U.PORTO
FEUP FACULDADE DE ENGENHARIA
UNIVERSIDADE DO PORTO

Department of Mechanical Engineering

Numerical Analysis of Forming of Anisotropic Sheet Metals

Dipak Wagre

June 2020
Porto, Portugal

Dipak Wagre

Numerical Analysis of Forming of Anisotropic Sheet Metals

A thesis submitted to the
Faculdade de Engenharia da Universidade do Porto
for the Programa Doutoral em Engenharia Mecânica

Supervisor:	Professor Abel Dias dos Santos
Co-supervisor:	Professor José César de Sá

Departamento de Engenharia Mecânica
Faculdade de Engenharia
Universidade do Porto

A PhD thesis

Numerical Analysis of Forming of Anisotropic Sheet Metals

Submitted by

Dipak Wagre

Supervisor: **Professor Abel Dias dos Santos**
Department of Mechanical Engineering
Faculty of Engineering, University of Porto

Co-supervisor: **Professor José César de Sá**
Department of Mechanical Engineering
Faculty of Engineering, University of Porto

President and the Jury Committee

Dr. Renato Manuel Natal Jorge (President)
Professor at Department of Mechanical Engineering, University Porto, Portugal

Dr. Marta Cristina Cardoso de Oliveira
Professor at Department of Mechanical Engineering, University of Coimbra, Portugal

Dr. Gabriela Tamara Vincze
Professor at Department of Mechanical Engg., University of Aveiro

Dr. Pedro Manuel Cardoso Teieira
Researcher at Frezite High Performance Ltd.

Dr. Abel Dias dos Santos (Supervisor)
Professor at Department of Mechanical Engg, University of Porto

Dr. Marco Paulo Lages Parente
Professor at Department of Mechanical Engg, University of Porto

ABSTRACT

An accurate modeling of the sheet metal deformations including the springback is one of the key factors in the efficient utilization of finite element (FE) process simulation in the industrial practice. The use of newer materials such as advanced high strength steels (AHSS) and aluminum alloys in automobile industry is increasing. For such newer materials, forming and springback prediction poses many challenges, because it is strongly influenced by numerical parameters such as the type, order and integration scheme of finite elements as well as the shape and size of the finite element mesh, but also of the constitutive model adopted.

A benchmark test of an automotive aluminum panel was analyzed under the proposal of Numisheet conference series. The numerical results were obtained using different FE codes and different approaches for material models and comparisons were performed between available obtained numerical results, as well as between numerical and experimental data. The analysis gives an insight into issues related to the comparison of results in complex geometries involving springback, leading to some recommendations for similar benchmarks.

An additional topic was the development and implementation of both associated and non-associated plastic flow rules and the models were implemented into the finite element code ABAQUS, using a dynamic-explicit analysis. The anisotropic parameters for the yield function were identified using the directional yield stresses, bulge yield stress and shear yield stress, while those for the plastic potential function were identified using the directional r-values. Capabilities of the developed model for predicting the anisotropic behavior of sheet metal were investigated by considering cup height evolution for different directions and through-thickness strain distributions obtained from the simulations. Also, springback analysis was performed for the cup test using the different numerical approaches. Four different anisotropic sheet materials were used to validate results with bibliography and experimental data. Sensitivity analysis of various parameters is performed using different numerical approaches. Numerical results were compared with the experimental data and results demonstrate that the developed material models can improve accuracy of predicting the anisotropic and springback behaviors. Furthermore, the simple formulations are efficient and user-friendly for computational analyses and to solving the common industrial sheet metal forming problems.

Keywords:

Sheet Metal Forming, Anisotropy, Springback, Numerical Simulation, Flow Rule.

RESUMO

A modelação numérica rigorosa das deformações plásticas, incluindo o retorno elástico é um dos fatores fundamentais para o uso eficiente do método dos elementos finitos na simulação de processos industriais. A utilização de novos materiais como aços avançados de alta resistência (AHSS) e ligas de alumínio na indústria automóvel tem sido crescente, no entanto, tais ligas estão ligadas a maiores valores de alteração da geometria final, em virtude do retorno elástico. De facto, a previsão do retorno elástico coloca um número de desafios por ser influenciada por diversos parâmetros numéricos como o tipo, ordem e esquema de integração dos elementos finitos, assim como a forma e tamanho da malha e ainda com o modelo constitutivo adotado. Adicionalmente, as medições nos componentes complexos requerem a definição de um dispositivo, que não infuencie as medições e tenha uma referência absoluta sobre as secções de medição e respetivas direções.

Um dos tópicos do presente trabalho analisa um benchmark dedicado à conformação plástica e previsão do retorno elástico de um componente automóvel e foi proposto no âmbito de conferência internacional Numisheet. Os resultados numéricos são obtidos por diferentes códigos de elementos finitos com diferentes abordagens para os modelos de material e são feitas comparações tanto entre os diferentes códigos, como entre os resultados numéricos e experimentais. O estudo mostra as questões relacionadas com a comparação de resultados em geometrias complexas envolvendo retorno elástico, permitindo uma série de recomendações sobre novos benchmarks.

Um tópico adicional de desenvolvimento é o relacionado com modelação anisotrópica de chapas metálicas. O desenvolvimento considerou a implementação de diversos modelos de leis de escoamento associativas e não-associativas e os modelos foram implementados no código de elementos finitos Abaqus, com análise explicita. São investigadas as capacidades dos modelos desenvolvidos na previsão do comportamento anisotrópico de chapas metálicas, considerando a conformação de copos cilíndricos e a medição de alturas das orelhas de embutidura, as variações de espessura do copo, bem como a análise do retorno elástico. A comparação dos resultados numéricos com os experimentais demonstram que os modelos desenvolvidos baseados em leis não-associadas melhoram o rigor, quer da previsão do comportamento anisotrópico do material, quer do retorno elástico. Adicionalmente, verifica-se que as formulações implementadas são simples, eficientes e amigáveis, bem como perfeitamente adequadas para análise computacional e para resolver os problemas industriais de conformação de chapas metálicas.

Palavras-chave

Embutidura, Anisotropia, Retorno Elástico, Simulação Numérica, Cedência Plástica.

Acknowledgments

I would like to acknowledge and express my deepest appreciation to a few people without whom this dissertation couldn't have been accomplished.

I am very grateful to my supervisors Prof. Abel Dias dos Santos for his constant support, availability, readiness, transmitted knowledge and specially for all their patience. Without him I would not have able to finish this work.

A great thanks to my guide Prof. César Sá and Prof. António Baptista who supported me in all the ways and for valuable guidance. Also, I am thankful to Prof. Marta Oliveira for her help and valuable guidance.

I would like to express my gratitude to Prof. Jorge H. O. Seabra, for the help and facilities and Dr. Ramiro C. Martins, Beatriz Graça, Jose Brandão, Carlos Fernandes, David Gonçalves, Pedro Marques not only for their constant help and support and help.

Special thanks for Rui Amaral, Sara Miranda, Daniel Cruz and colleagues from INEGI for their valuable time and helping me throughout this research.

I am thankful to Erasmus Mundus Action 2, LEADERS Project coordinated by City, University of London, United Kingdom, scholarship for Doctoral Program. I would like to thank INEGI, Institute of Science and Innovation in Mechanical and Industrial Engineering, providing me research fellowship and facilities.

Also, it is gratefully acknowledged the funding of Project NORTE-01-0145-FEDER-032419 msCORE - Multiscale methodology with model order reduction for advanced materials and processes and Project POCI-01-0145-FEDER-032466 NanosFLiD, POCI-01-0145-FEDER-030592 ifDamagElse and POCI-01-0145-FEDER-031243 RDFORMING cofinanced by Programa Operacional Regional do Norte (NORTE2020) and Programa Operacional Competitividade e Internacionalização (Compete2020), through Fundo Europeu de Desenvolvimento Regional (FEDER) and by Fundação para a Ciência e Tecnologia through its component of the state budget.

Finally, I would like to thank my family, my amazing brother Vishal, sisters Namrata and Dipali, and specially to dear Madhuri for all the encouragement and support given throughout my life and during this research. I am thankful to my friend Vanessa for helping me during the life in Porto. I am thankful to all friends and specially to some dear friends Gosia, Jana, Sebastian and Vishwas who are always source of inspiration.

Porto, June 2020
Dipak Gopinath Wagre











To My Parents

आई - पप्पा

Contents

Contents viii

List of Symbols xv

1 INTRODUCTION 1

1.1 Motivation 2

1.2 Scope and layout of the thesis 5

2 SHEET METAL FORMING 7

2.1 Introduction 7

2.2 Springback prediction using FEM 11

2.3 Constitutive Models of Plasticity 13

2.3.1 Hill'48 Anisotropic Function 14

2.3.2 Non-Associated Flow Rule 15

2.3.3 Yield Function based on stresses 16

2.3.4 Hill'48 Potential Function based on r-values 17

2.3.5 Stress Integration Procedure 19

3 SPRINGBACK IN ANISOTROPIC SHEET METALS 22

3.1 Introduction 22

3.2 Springback in bending 23

3.3 Benchmark study of an automotive panel 24

3.3.1 Forming process 25

3.3.2 Forming simulation 25
3.3.3 Element type 26
3.3.4 Material properties 27
3.3.5 Boundary conditions 28
3.4 Benchmark results of section profiles 29
3.4.1 Numisheet results after springback 30
3.4.2 Comparison of results after springback 33
3.4.3 Analysis of blank draw-in, AF-UP vs. DD3-UC 36
3.4.4 Discussion of results 38
3.5 Benchmark results of section profiles using global planes 40
3.5.1 Section profile before forming 40
3.5.2 Section profile after forming 41
3.5.3 Section profile after trimming and before springback . . . 41
3.5.4 After springback 42
3.5.5 Discussion 43

4 NON-ASSOCIATED PLASTIC FLOW MODEL EVALUATION 44

4.1 Introduction 44
4.2 Selected sheet materials 46
4.2.1 Mechanical properties 46
4.2.2 Yield stresses and r-values evolution 48
4.3 Single element case study 49
4.3.1 Single element numerical results 51
4.4 Cylindrical cup test 54
4.4.1 Finite element models 55

4.4.2 Mesh sensitivity analysis 57
4.4.2.1 Results 58
4.4.3 NAFR vs. AFR results using different methodologies . . . 64
4.4.4 Sensitivity analysis for process variables 69
4.4.4.1 Friction 69
4.4.4.2 Blank holder clearance 70
4.4.4.3 Anisotropic parameters 71

5 APPLICATION TO CUP DRAWING AND SPRINGBACK 75

5.1 Cylindrical cup drawing 75
5.1.1 Experimental setup 75
5.1.2 Material properties and numerical model 76
5.1.3 Cup height evolution, stress and strain contours 78
5.1.4 Thickness strain 86
5.1.5 Sensitivity analysis for anisotropic parameter τ_{xy}/σ_0 . . . 89
5.2 Cup split and springback 93
5.2.1 Experimental methodology and numerical modelling . . . 93
5.2.2 Stress contours and springback 95
5.2.3 Earing evolution and experimental validation 102

6 CONCLUSIONS AND FUTURE WORK 108

6.1 Concluding remarks 108
6.2 Future work 110

References 111

List of Figures

2.1 Deep drawing process schematics 8
2.2 Aluminum Panel used in a Jaguar Land Rover 10
2.3 Schematic of yield and potential surfaces [28] 16
2.4 Schematic view of Newton-Raphson Method [28] 20

3.1 Springback in Bending 22
3.2 Assembly setup 26
3.3 Schematic of Top, Middle and Bottom layer of the Element 26
3.4 Defined boundary condition for springback 29
3.5 Defined sections for analysis 30
3.6 Numisheet results - Local converted 2D frame - Section A 31
3.7 Numisheet results - Local converted 2D frame - Section B 31
3.8 Local converted 2D frame - Section A, after springback 32
3.9 Section A, after springback - numerical and experimental profiles 34
3.10 Section B, after springback - numerical and experimental profiles 35
3.11 Section C, after springback - numerical and experimental profiles 35
3.12 Blank position with pivots after blank holding. 36
3.13 Blank draw-in for AF-UP simulation. 37
3.14 Blank position before and after binder closure. 37
3.15 Blank position after blank holding and forming. 38
3.16 AF-UP and DD3-UC predicted geometries 40
3.17 YZ section profile after blank holding stage 41
3.18 YZ section profile after forming stage 41
3.19 YZ section profile before springback 42
3.20 YZ section profile after springback 42

4.1 Numerical r-value evolution with different models for AA2090 . 48
4.2 Numerical yield stress evolution with different models for AA2090 49
4.3 Boundary conditions for test model 50
4.4 Swift hardening behavior for AA2090-T3 50
4.5 Hill'48 3D yield surface for the AA2090 51
4.6 True stress-strain along rolling direction 52
4.7 True stress-strain along longitudinal direction 52
4.8 Schematic view of the cylindrical cup-drawing test 54
4.9 Typical parts in the FE model: Die, Punch, Blank Holder and Blank 55
4.10 Numerical tool assembly for the cylindrical cup drawing 56
4.11 Different stages of cylindrical cup drawing 56
4.12 Example of different meshes used for the cylindrical cup test . . 57

4.13 Two mesh models for the AA2090 material 59
4.14 Cup height comparison of AA2090 different mesh 59
4.15 Cup height comparison of AA6061 different mesh 60
4.16 Effect of Different Mesh along Perimeter 60
4.17 Effect of Different Mesh in Thickness 61
4.18 Effect of Different Mesh in Radial direction 62
4.19 Effect of Different Mesh in Radial direction for SPCE 63
4.20 Validation of VUMAT with Abaqus code results 64
4.21 In-plane vs 3D formulation of Hill48 function 65
4.22 In-plane vs 3D formulation of Hill'48 function for AA6061 65
4.23 Contours of the equivalent plastic strain 66
4.24 in-plane vs 3D formulation of Hill48 function for SPCE steel . . . 67
4.25 Contours of the equivalent plastic strain for different approaches 67
4.26 Cup height using 3D formulation SPCE 69
4.27 Effect of friction on cup height prediction: SPCE 70
4.28 Effect of blank holder clearance on cup height prediction: SPCE . 70
4.29 r-value evolution for different r-values: SPCE 71
4.30 Cup height prediction for different r-value: SPCE 72
4.31 Effect of different r-values for prediction of earing 72
4.32 Cup height prediction for different r-value: Case a2 and a4 . . . 73
4.33 Case a5 and a6: Cup height and earing prediction: SPCE 73
4.34 Cup height prediction using proposed r-values 74

5.1 Experimental universal testing machine and tool 76
5.2 Schematic view for cylindrical cup drawing test 76
5.3 DP780 hardening curves from tensile test and shear test 77
5.4 Mesh distribution for DP780 blank 78
5.5 Cup height evolution subroutine verification 79
5.6 Equivalent stress contours using Abaqus and VUMAT 80
5.7 Plastic equivalent strain contours using Abaqus and VUMAT . . 80
5.8 Cup height evolution along different angles 81
5.9 Equivalent stress contours for different approaches 81
5.10 Plastic equivalent contours for different approaches 81
5.11 Cup height evolution comparison of Numerical and experimental 82
5.12 Equivalent stress contours for different approaches 82
5.13 Equivalent stress contours for different approaches 82
5.14 Cup height evolution comparison of Numerical and experimental 83
5.15 Equivalent stress contours for different approaches 83
5.16 Equivalent stress contours for different approaches 84
5.17 Cup height evolution along different angles 85
5.18 Equivalent stress contours using NAFR 85
5.19 Plastic equivalent strain contours using NAFR 85
5.20 View of earing cup profile from experimental cup 86
5.21 Cylindrical cup: experiment and simulation 86
5.22 Comparison of predicted thickness strain: DP780 87
5.23 Predicted thickness strain for NAFR 88
5.24 Comparison of predicted thickness strain along TD 88

5.25 Predicted thickness strain along RD 89
5.26 Cup height evolution for parameter sensitivity 90
5.27 Equivalent stress contours for sensitivity 90
5.28 Plastic equivalent strain contours for sensitivity 90
5.29 Cup height evolution along different angles for AFR-S3D 91
5.30 Equivalent stress contours for AFR-S3D 91
5.31 Plastic equivalent strain contours for AFR-S3D 91
5.32 Cup height evolution of NAFR sensitivity 92
5.33 Equivalent stress contours of NAFR sensitivity 92
5.34 PEEQ contours of NAFR sensitivity 92
5.35 Experimental cylindrical cup 94
5.36 Boundary conditions for springback simulation 95
5.37 Contours for springback 96
5.38 Contours for springback 96
5.39 Contours for springback for S-inPlane 97
5.40 Contours for springback for S3D 97
5.41 Contours for springback for NAFR in-plane 98
5.42 Contours for springback for NAFR S3D 98
5.43 Contours for springback for NAFR S3D 99
5.44 Lateral profile section after springback 100
5.45 Lateral section springback profile for different methods 100
5.46 Displacement contours after springback 101
5.47 Displacement contours after springback 102
5.48 Cup height evolution befor and after springback for AFR 103
5.49 Cup height evolution befor and after springback for NAFR . . . 103
5.50 View of experimental cup after vertical split (STL data 104
5.51 Experimental STL raw data with corresponding coordinate system 104
5.52 Comparison of experimental cup profile 106
5.53 Comparison of experimental geometry with simulation 106
5.54 Comparison of experimental geometry with NAFR simulation . 107

List of Tables

2.1 Hill'48 anisotropic parameters 18

3.1 Elastic mechanical properties 27
3.2 Uniaxial tension test data 27
3.3 Equal biaxial tension test data 27
3.4 Hardening curve 27
3.5 Material constants for yield function Yld2000-2d (a = 8.0) 28
3.6 Material constants for yield function Yld89 (m = 8.0) 28
3.7 Boundary conditions for forming and trimming operations . . . 28
3.8 Boundary Conditions 28
3.9 Defined normal vectors for the section planes 29

4.1 Material properties of AA2090-T3 46
4.2 Values of Hill'48 parameters for AA2090-T3 47
4.3 Material properties of AA6061-T6 47
4.4 Values of Hill'48 parameters for AA6061-T6 47
4.5 Material properties of SPCE 48
4.6 Hill'48 parameters for SPCE 48
4.7 Numerical results: r-value comparison 53
4.8 Dimensions of tools for cup drawing (mm): AA2090 54
4.9 Dimensions of tools for cup drawing (mm): AA6061 and SPCE . 55
4.10 Simulation boundary conditions (BC) 56
4.11 Different mesh models 58
4.12 Parameters for anisotropy sensitivity for SPCE 71

5.1 Mechanical properties for DP780 material 77
5.2 Values of Hill'48 parameters for DP780 77

List of Symbols

$\boldsymbol{d\sigma}$	Stress tensor increment
$\boldsymbol{d\varepsilon}$	Strain tensor increment
$\boldsymbol{d\varepsilon}^e$	Elastic strain increment
$\boldsymbol{d\varepsilon}^p$	Plastic strain increment
$d\bar{\varepsilon}^P$	Equivalent plastic strain increment
$d\lambda$	Plastic multiplier increment
dW	Plastic work increment
$\boldsymbol{D}^e$	Elastic stiffness tensor
$\boldsymbol{D}^{ep}$	Elastic-plastic tangent modulus
$\bar{\varepsilon}^p$	Equivalent plastic strain
ϕ	Yield criterion
f	Yield stress function
g	Plastic potential function
h	Isotropic hardening function
F,G,H,L,M,N	Parameters of the yield function
F^*, G^*, H^*, L^*, M^*, N^*	Parameters of the potential function
$\boldsymbol{m}$	First order gradient of yield function
$\boldsymbol{n}$	First order gradient of potential function
P	Ratio of the potential function to the yield function
$\bar{\sigma}_f$	Equivalent stress of the yield function
$\bar{\sigma}_g$	Equivalent stress of the potential function
$\bar{\sigma}_Y$	Equivalent stress at uniaxial tension
$\boldsymbol{\sigma}$	Cauchy stress tensor
$\boldsymbol{\sigma}^{tri}$	Trial stress tensor

1 INTRODUCTION

Sheet metal forming is one of the most common metal processing manufacturing technologies and automotive parts are an important application due to corresponding production volume and competitiveness. Sheet metals are stamped between die and punch so as to give the desired part geometry. Also, light metal alloy beverage cans are produced using forming operations such as deep drawing, ironing and coining. In all of these examples, great precision is required relative to both the geometry and mechanical properties for the final product. It has therefore become apparent that the traditional trial-and-error method of optimizing such metal forming operations is rather inefficient. The mathematical modeling of material behavior is a very effective way of reducing the time and costs involved in optimizing manufacturing processes. Indeed, numerous complex forming operations have been simulated numerically in order to predict and optimize critical parameters.

During the tryout of a forming process various types of defects are usually appearing in the formed part. Examples of such defects are:

- Fracture in the material, usually preceded by a marked strain localization;
- Excessive thinning in some areas of the blank;
- Wrinkling, which implies the formation of bulges with relatively short wavelength due to high compression stresses;
- Buckling, a term used for bulges with long wavelength, preferably appearing in unsupported areas of the blank with small compression stresses;
- Springback is a term for those deformations that take place when a workpiece is removed from the tools after completed forming;
- Various surface defects, which usually are due to insufficient stretching of the material.

It is the purpose of the die design and process layout work, and the subsequent

tool tryout, to optimize the forming process in such a way that these defects can be avoided.

The simulation of sheet metal forming receives continuously increasing attention from the material science society as well as the computational community. It has been recognized that the plastic behavior of textured polycrystalline sheets is mainly anisotropic due to the processing of the material. The anisotropic mechanical behavior of this material has a great influence on the final shape and residual stress of the parts [1].

1.1 Motivation

Concerns about energy consumption have increased in the manufacturing industry due to a rise in energy cost and ecological adverse outcomes of production [2]. Industrial sector accounts for approximately 50% of the total energy consumption in which the manufacturing sector accounts major share of the energy consumption [3]. Hence, the increase in global concern for the environment, and consequently, energy saving has become a focal subject of the modern manufacturing industry. To reduce the environmental impact of the manufacturing processes, uses of lightweight materials and parameter optimization of the manufacturing processes can be seen as important aspect of the energy impacts in manufacturing industry. Due to high demand for weight reduction in the automobile industry the use of stronger or lighter sheet metals, e.g., ultrahigh strength steel or low-density metals such as aluminum alloys, has increased exponentially. This necessity for lightweight design, multi-material concepts, advanced high strength (AHS) steels, aluminum alloys due, to the tough fuel economy and to meet the emission standards the automotive industry continuously urge to use newer materials. Aluminum alloy sheets are widely used in the car, ship building and aerospace industries as substitutes for steel sheets and fiber reinforced plastic panels, due to their excellent properties such as high strength, corrosion resistance, and weld abilities [4].

Several parameters such as material, geometric or test parameters can influence the forming process. Accordingly, one has to get a deep insight into parameters influencing the process. Due to its high efficiency and relative low-cost, numerical simulation has become an important tool for the optimizing the process

parameters and solving the problems in the design of the products and in the manufacturing processes. Therefore, for the accurate numerical modeling of sheet metal forming processes, the use of suitable material models that correctly describe material behavior is currently a fundamental need.

Rolled sheet metals exhibits anisotropic behavior which affects the formability of the final part. The anisotropic behavior is crucial while considering constitutive modeling of sheet metals. Hence, an accurate and appropriate anisotropic constitutive model is essential in order to improve the accuracy and efficiency of manufacturing processes of sheet metals. In sheet metals, the anisotropic behavior is commonly described by Lankford coefficient (r-value) and yield stresses in defined orientations relative to the rolling direction. In the past, various anisotropic models have been proposed to analyze and reproduce the anisotropic behavior in the sheet metal forming processes. The classical Hill [5] quadratic function (Hill'48), which applies the r-value to describe the deformation anisotropy, is the original yield function for anisotropic sheet metals. Although the Hill'48 function has a simple quadratic form and the ability to describe the orthotropic anisotropy for some metals with accuracy, it shows some limitations in accurately predicting material behaviors under complex loading conditions, particularly for some aluminum alloys (r-value < 1). Woodthorpe (1970) [6] performed uniaxial tension and hydraulic bulge tests on cold-rolled purity aluminum sheets. Their results demonstrate that Hills theory underestimates the ratio of biaxial to uniaxial yield stress by more than 20% [7].

Many proposed models which studied anisotropic sheet metals, generally have been developed based on the associated flow rule (AFR) [8–10], which follows the classical normality rule and stating that the yield function and plastic potential function are identical. However, some studies [11,12] show that some anisotropic materials such as aluminum alloys and ferrous materials do not satisfy the AFR constrains. To overcome such difficulties some recent efforts [1, 12–17] have been made to develop methods of numerical analysis based on non-associated flow rule (NAFR) in which different functions are utilized to describe the plastic yield function and potential (flow) function. Although, the concept of NAFR to improve elasto-plastic behavior was discussed by Melan back in 1938 [18], it seems that the engineering applications are relatively recent. The NAFR constitutive model could be implemented to improve the accuracy of solutions but work conjugate rule should be followed to keep the theoretical

continuity [19,20].

While the classical Hill'48 function has a clear 3D expression, many previous studies [13,21–23] in which only in-plane condition was assumed, which provides the simplified form of the Hill'48 function. Although, this may be economical to implement from the development and computational point of view, it limits the numerical simulation to shell elements only. Ogawa et al. [24] and Yoshida et al. and others [25,26] pointed out that in some cases of forming consideration, 3D stress condition is important e.g., sheet forming, forging, bottoming, ironing, etc. However, the 3D stress models implementation comes with a cost of higher computational efforts as well as it requires higher parameter identification and material testing, which is challenging. Some studies such as [14,27,28] shows improvement in prediction of the anisotropic sheet forming.

In this work formulations of NAFR model with the isotropic hardening law were derived and the work conjugate rule was strictly followed. Furthermore, a cutting-plane return-mapping method was utilized to integrate the stress and state variables over each time increment. The developed model was implemented in the commercial FE code ABAQUS via a user-defined material subroutine (VUMAT). Furthermore, the evaluation of the stability issue of using NAFR formulations when combined with complex yield functions indicates that the stability conditions are not violated.

The experimental data and anisotropic parameters for different materials were given and the validity of the developed model was discussed. The Hill'48 based model is simple and allows for a convenient approach for parameter identification. To evaluate its performance in FE simulations, cylindrical cup drawing processes were conducted and simulated with 3D solid elements for industrial sheet metal alloys, like AA2090-T3, AA6061-T6, SPCE and DP780 steels. To further assess the effects and accuracy on results, cup height evolution along different sheet directions and through thickness strain were extracted and compared with available experimentally values. The developed model was shown to be an efficient choice for these selected sheet materials.

The challenges on material behavior such as springback, wrinkling, fracture are more complex in the new materials such as aluminum alloys and high strength steels. Springback not only causes difficulties in joining the parts

and assembling, but need to compensate before finalizing the die design. Due to tight design tolerances is it very much important to accurately predict the springback behavior and this has to be done in the design stage of dies. It is more challenging due the fact that the springback can be seen only after formed stage and to overcome that some changes in tool design are needed or in the design of the part itself. To overcome the problem of change of geometry due to springback, tooling compensation is needed. In order to achieve this goal, numerical simulations must be provided with the material and process data as accurate as possible. Hence, each aspect of the FE modelling and prediction of material behavior needs to be studied thoroughly.

1.2 Scope and layout of the thesis

In this study several aspects of FEM simulations have been studied. The main focus has been in springback and forming predictions for anisotropic materials. Different materials have been used and tested using implemented associated and non-associated flow rules. Chapter one gives a bibliographic overview about some of the topics which are presented in this work and the motivations for carrying out these studies.

In chapter two, a more detailed review is performed, which includes some fundaments of sheet metal forming, the main aspects of springback simulation and the background of mathematical constitutive equations and methodologies used in this study.

Chapter three is dedicated to springback analysis with a main focus on industrial application and state-of-the-art benchmark simulation, in addition to challenges of numerical validation with experimental results.

Chapter four presents the implementation of non-associated flow rule. A single element case and a cylindrical cup drawing study are selected to validate and test the implemented associated (AFR) and non-associated flow rule (NAFR) approaches.

Chapter five is the application of implemented and developed anisotropic constitutive models to an experimental cylindrical cup, with the objective of

validation, not only to forming prediction capabilities but also the springback analysis.

Finally, in chapter six, a short summary and the conclusions of this work are presented along with suggestions for future research.

2 SHEET METAL FORMING

2.1 Introduction

In today's automobile industries, the primary materials used are high and ultrahigh strength steels as well as aluminum alloys. These materials enable car manufacturers to design lighter cars taking also into account the increasing safety requirements. However, the application of these materials poses additional challenges. Forming parts made from high and ultrahigh strength steels and aluminum alloys are more affected to forming challenges and springback than parts made from conventional deep-drawn steel [4, 29]. In order to remain competitive, engineers must find ways to reduce the engineering time required for part and tool production and modern engineering addresses these challenges by applying stamping simulation.

Within the wide range of metal forming processes, a distinction is made between bulk metal forming and sheet metal forming. The first group contains elements such as forging and extrusion, while the second group consists mainly of bending and deep drawing. This latter process forms the basis of the present study.

By far the most common sheet forming process is stamping, which especially is used in the huge automotive industry. In the stamping process the metal sheet is formed by rigid tools, which, on its fundamental parts; consist of a punch (male part), a die (female part), and, a blank-holder. The role of the blank-holder is to press the blank against the die and prevent it from wrinkling, and also through friction forces control the material flow into the die cavity during the stroke. The main advantage of the stamping process is its high productivity, which is a very important quality in the highly efficient and automated car manufacturing industry [30].

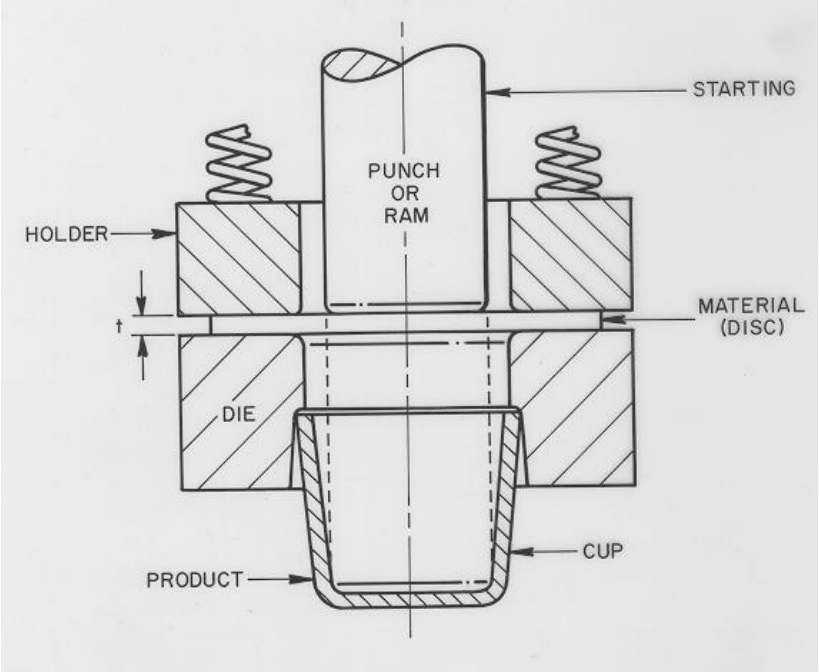


Fig. 2.1: Deep drawing process schematics

Figure 2.1 shows a typical stamping setup i.e. deep drawing of a cylindrical cup, in which a planar disk is transformed into a cup with a flat bottom, cylindrical walls, and an open top. The disk is placed over the opening in the die and forced to deform by moving the punch. As the punch moves downward, it pulls the flange toward the center. The flange is held between the die and the blank-holder, with the purpose of preventing the flange from folding upward. The blank-holder is also called as binder. The flange moves inward radially while its inner side bends over the rounded corner of the die and transforms from a flat disk to a circular tube. The bottom is not deformed, while the cylinder is already deformed but is not undergoing further deformation also, the toroidal section between the cylinder and the flange is bending, and the flange is undergoing plastic deformation.

The use of numerical modeling is now vital stage in the pre-production phase of the tooling for metal forming operations. With the use of these models (mostly finite element simulations), the time consuming and costly trial and error process can be reduced to great extent. To obtain a valid model, the required input should be as accurate as possible. The input basically consists of geometrical quantities of the tools and material behavior for both the elastic-plastic work piece and the rigid tools, contact conditions at the interface between tool and work piece and, finally, some process conditions such as punch force, velocity,

boundary conditions.

Springback describes the change in shape of a formed sheet upon removal from the tooling. Springback has been a severe problem in the design of automotive sheet metal stamping processes, especially with the increasing use of lightweight materials with higher strength-to-modulus ratio such as aluminum and high strength steels (HSS) [31]. The use of these materials involves a particular challenge because of their severe, and sometimes peculiar, springback behavior. The springback phenomenon has been deeply and extensively studied numerically with the increase of computational capacities, since it is more sensitive to numerical parameters and tolerances than the forming process. However, numerical simulation of the springback phase is still difficult to predict accurately [32], since it is influenced by a great number of parameters of two different kinds: physical and numerical. The finite element analysis (FEA) of springback is shown to be very sensitive to many numerical parameters, including the number of through-thickness integration points, type of element, mesh size, angle of contact per element on die shoulder, possible inertia effects and contact algorithm. Moreover, springback is also sensitive to many physical parameters including material properties, hardening laws, coefficient of friction, blank-holder force (BHF) and possible unloading procedure. All that makes springback simulation very cumbersome [33].

Stamping simulation is used to verify formability issues, such as splits and wrinkles. In the past, the main focus when analyzing splits and wrinkles was on the drawing stage. In recent years, higher quality requirements have to be verified, and one of the most important of them is a geometrical accuracy. In particular, verification of springback and its countermeasure, springback compensation, are carried out regularly in car body engineering. Gained experience has shown that compensation is not an easy task. In order to carry out the compensation effectively, a set of requirements has to be fulfilled.

This set of requirements includes springback feasibility. The analysis of springback feasibility ensures that the defined process setup allows for efficient compensation in which there is no backdraft in the drawing tool and formability is not compromised.

Figure 2.2 shows a typical automotive aluminum panel which was the topic of a

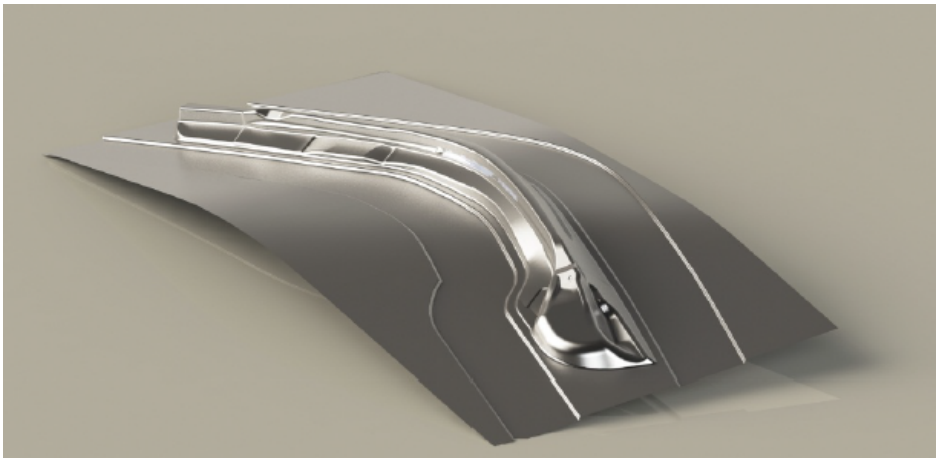


Fig. 2.2: Aluminum Panel used in a Jaguar Land Rover

benchmark test for a NUMISHEET conference [34] and it was used for forming analysis, as well as springback.

Springback is one of the most important problems for the sheet metal forming industry due to the strong geometrical deviations which occurs through elastic recovery after forming. These deviations can lead to many manufacturing difficulties such as joining parts together into a more complex assembly. Springback is influenced by the forming operations and the degree of constraints imposed by the geometry of the part but it is also strongly dependent on the material properties of the blank sheet. For aluminum, springback behavior is more complex because of its strong plastic anisotropy and low Young's modulus. Consequently, inaccurate material models can lead to major or unexpected deviations in the prediction of springback.

The kinematic hardening effect of bending and unbending deformation through the different die radius and curvatures of the tools can significantly influence the nature and prediction of panel's springback. The springback prediction of different loading/unloading forming operations requires the use of appropriate kinematic and/or combined kinematic/isotropic hardening models, together with sophisticated flow rules and yield functions.

2.2 Springback prediction using FEM

During the development stage of tools, springback is analysed and predicted by FEA (finite element analysis) codes so that compensation can be performed and the part can be removed from tools with the required geometry order to remove the part from the tool straight away in the required dimensions. Therefore, any tryout loops, which occur at a very late stage in the development of the tool, are reduced to a minimum.

Commercial codes based on finite element method can detect not only springback early on, they can also compensate for it. In this way, tooling processes are improved and manufacturing costs are significantly decreased. Springback compensation thus minimizes the risk of costly modifications on tools or processes later on.

Springback is one of the main factors that influence the geometry of the final product, which if not properly controlled, can affect the precision resulting in product quality. This is a phenomenon that occurs after the plastic deformation and after the removal of the forces applied to the tools, which depends on the conjugation and / or interaction of a large number of factors:

- mechanical properties of materials;
- tool geometry;
- levels and distribution of stresses and strains;
- process parameters (clamp pressure, lubrication, etc.).

The simulation of springback depends not only on the forming conditions (contact, friction and geometry of the tools) but also on the choice of the constitutive model applied to the material and the numerical implementation in the finite element program, element size, element type and points of integration along the thickness and in the plane [35,36]. With shorter delivery times, coupled with the increasing use of high strength materials, the simulation of the springback in the plastic deformation of sheet metal has become a fundamental aspect for better tool design and process optimization (Wagoner 2007). Therefore, the change in the geometry of the final product caused by the springback brings with it numerous problems.

Traditional methods of trial and error are expensive and time-consuming,

whereas an empirical approach based on slight adjustments for springback does not usually apply to complex geometries and / or materials whose mechanical behavior is not fully known [37]. However, it is necessary to take into account the economic impact in terms of delay in the production, revision and rejection of parts due to this geometric deviation. The prediction of springback is a very relevant issue in the industry, regarding the processes of sheet metal forming. It can be obtained in two different ways, one making use of the removal of tools, another one using equivalent forces for elastic recovery.

The non-tool springback initially considers forces as a boundary condition for nodes that are in contact with the tools at the last stage of the forming process. The springback ceases after these forces cancel out. The tool type simulation springback, which occurs according to the unloading operation of the industrial process, is based on the reversal of tools, after the plastic forming process, and the punch is unloaded by reversing its movement, until there are no nodes in contact with the tools.

To successfully implement springback compensation based on simulation results, the following conditions have to be fulfilled:

- It must be possible to set up and simulate the entire forming process, including all secondary operations such as trimming or flanging, in a single system.
- The exact springback simulation requires a finite element analysis (FEA) formulation that predicts not only strain states for failure prediction, but also stress states. In addition, appropriate algorithms that can efficiently solve the corresponding sets of equations are needed.
- The entire forming process must be designed robustly with respect to noise (interference). Therefore, a stochastic (pertaining to random variables) simulation is necessary, whereby certain parameters are varied automatically, leading to multiple evaluations of the process. The results should be presented in an intuitive and easy-to-interpret manner.

Some recent studies [38,39] analyzed the effect of the advanced plastic anisotropic constitutive models to understand the springback and Bauschinger effect, and elastic modulus degradation. Such studies with sensitivity analysis on the constitutive model shows that mainly plastic anisotropy and elastic behavior of a

material influence the panel stiffness. One of the classical anisotropic constitutive model Hill'48 function with the NAFR could better predict the springback because the anisotropy in both the r-values and yield stress could be applied for the identification of model coefficients [33].

2.3 Constitutive Models of Plasticity

With the assumption of isotropic linear elasticity and additive decomposition of the strain tensor increment, Hooke's law can be given as:

$$\boldsymbol{d\sigma} = \boldsymbol{D}^e : \boldsymbol{d\epsilon}^e = \boldsymbol{D}^e : (\boldsymbol{d\epsilon} - \boldsymbol{d\epsilon}^p) \tag{2.3.1}$$

where $\boldsymbol{d\epsilon}$ is the total strain increment, $\boldsymbol{d\epsilon}^e$ and $\boldsymbol{d\epsilon}^p$ are the elastic and plastic strain increments respectively, assuming the isotropic hardening law. The yield criterion to define anisotropic yield stresses is defined as:

$$\phi(\boldsymbol{\sigma}, \bar{\varepsilon}^p) = f(\boldsymbol{\sigma}) - \sigma_Y(\bar{\varepsilon}^p) = 0 \tag{2.3.2}$$

Following previous work [20,40,41], the flow rule is used to define the plastic strain increment, as

$$\boldsymbol{d\epsilon}^p = d\lambda \frac{\partial g(\boldsymbol{\sigma})}{\partial \boldsymbol{\sigma}} = d\lambda \cdot \boldsymbol{n} \tag{2.3.3}$$

and if the potential function $g(\sigma)$ is identical to the yield function $f(\sigma)$, the plastic strain increment is defined as,

$$\boldsymbol{d\epsilon}^p = d\lambda \frac{\partial f(\boldsymbol{\sigma})}{\partial \boldsymbol{\sigma}} = d\lambda \cdot \boldsymbol{m} \tag{2.3.4}$$

where, **n** = first order gradient of the potential function and **m** = first order gradient of the yield function.

By Euler's work conjugate equivalence of plastic work, the strain increment, is given as

$$dW = \overline{\boldsymbol{\sigma}}_f(\boldsymbol{\sigma}) d\bar{\varepsilon}^p = \boldsymbol{\sigma} : \boldsymbol{d\epsilon}^p \tag{2.3.5}$$

$$d\bar{\varepsilon}^p = \frac{\boldsymbol{\sigma} : \boldsymbol{d\epsilon}^p}{\overline{\sigma}_f(\boldsymbol{\sigma})} = d\lambda \cdot \left(\frac{\boldsymbol{\sigma} : \frac{\partial g(\boldsymbol{\sigma})}{\partial \boldsymbol{\sigma}}}{\overline{\sigma}_f(\boldsymbol{\sigma})} \right)_{f(\boldsymbol{\sigma}) - \overline{\sigma}_f(\boldsymbol{\sigma}) = 0} \tag{2.3.6}$$

$$= d\lambda \left(\frac{\boldsymbol{\sigma} : \frac{\partial g(\boldsymbol{\sigma})}{\partial \boldsymbol{\sigma}}}{f(\boldsymbol{\sigma})} \right) = d\lambda \cdot \frac{g(\boldsymbol{\sigma})}{f(\boldsymbol{\sigma})} = d\lambda \cdot P(\boldsymbol{\sigma}). \tag{2.3.7}$$

In case of associated plastic flow rule, the P becomes 1 and equation 2.3.6 can be simply reduced to

$$d\bar{\epsilon}^p = d\lambda \tag{2.3.8}$$

2.3.1 Hill'48 Anisotropic Function

The classical constitutive model of von-Mises employs the AFR to maintain consistency while the Hill'48 constitutive model takes into account of anisotropic material concerns. The Hill'48 function is one of the most popular and comprehensive yield functions in the sheet forming simulation process, particularly for the orthotropic, anisotropic metals [40]. Considering its simplicity, clear 3D expression and its physical meaning, this Hill'48 quadratic function was applied in this study. Hill'48 equivalent stress yield criterion is:

$$\bar{\sigma}_f = \sqrt{F(\sigma_{22} - \sigma_{33})^2 + G(\sigma_{33} - \sigma_{11})^2 + H(\sigma_{11} - \sigma_{22})^2 + 2L\sigma_{23}^2 + 2M\sigma_{31}^2 + 2N\sigma_{12}^2} \tag{2.3.9}$$

where 11, 22, and 33 represent the orthogonal principal anisotropic axes along the longitudinal, transverse and normal directions to rolling of metallic sheets, respectively.

The equation 2.3.9 is Hill'48 equivalent stress for yield surface, and the parameters F,G,H,L,M,N are defined using yield stresses in subsection 2.3.3.

$$\bar{\sigma}_g = \sqrt{F^*(\sigma_{22} - \sigma_{33})^2 + G^*(\sigma_{33} - \sigma_{11})^2 + H^*(\sigma_{11} - \sigma_{22})^2 + 2L^*\sigma_{23}^2 + 2M^*\sigma_{31}^2 + 2N^*\sigma_{12}^2} \tag{2.3.10}$$

The equation 2.3.10 is Hill'48 equivalent stress for potential surface, and the parameters F^*,G^*,H^*,L^*,M^*,N^* are defined using r-values in subsection 2.3.4.

In case of AFR the Hill's parameters F, G, H, L, M, and N are generally calculated based on r-values. As the associated flow rules is neither necessary nor sufficient conditions for some metals, hence it is very much interesting to use the full potential of the Hill's equation to model the material completely. The Hill'48 quadratic yield function, which is generalized from the von-Mises isotropic

function, is a reliable constitutive model with accuracy as well as being able to give the ability to model the complex anisotropic behavior. Different anisotropic materials with their corresponding parameters are used to obtained the yield function and potential function.

In this work we will follow the flow rule based on the eq. 2.3.8 to update the equivalent plastic strain.

2.3.2 Non-Associated Flow Rule

The constant need to utilize newer materials which are lightweight and stronger (e.g., automotive industry), creates challenges when components are manufactured using such newer materials for which the predicted behavior of traditional materials may not be applicable. Newer materials such as HSS steels and aluminum alloys are included in such materials for which there are stronger needs to predict accurately the mechanical behavior. Corresponding studies have a challenge to evaluate, analyze material behavior in sheet metal forming. Many factors including material properties, mechanical testing, numerical modeling and the methodologies affect accuracy to predict the sheet metal behavior.

When the Yield function and the Potential function are defined separately it is known as the Non-Associated Flow Rule (NAFR). For this study based on Hill 48, the parameters for yield function were identified with the planar yield stresses and the plastic potential function is defined on the basis of r-values. The schematic of the yield surface and potential surface when NAFR is used is shown in figure 2.3.

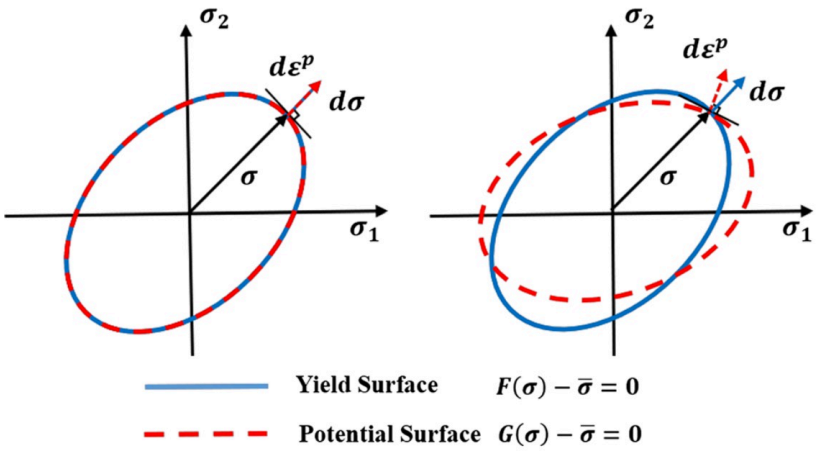


Fig. 2.3: Schematic of yield and potential surfaces [28]

For this study the yield function and potential function's parameters are defined in the next subsections.

2.3.3 Yield Function based on stresses

The Hill'48 yield function has its parameters based on the yield stress components. Equation 2.3.9 is used for the yield surface, where the Hill'48 parameters are defined as:

$$2F = \frac{\sigma_0^2}{\sigma_{90}^2} + \frac{\sigma_0^2}{\sigma_b^2} - 1 \tag{2.3.11}$$

$$2G = \frac{\sigma_0^2}{\sigma_b^2} + 1 - \frac{\sigma_0^2}{\sigma_{90}^2} \tag{2.3.12}$$

$$2H = 1 + \frac{\sigma_0^2}{\sigma_{90}^2} - \frac{\sigma_0^2}{\sigma_b^2} \tag{2.3.13}$$

$$2N_p = \left(\frac{2\sigma_0}{\sigma_{45}}\right)^2 - \left(\frac{\sigma_0}{\sigma_b}\right)^2 \tag{2.3.14}$$

$$2N_{3D} = \frac{\sigma_0^2}{\tau_{xy}^2} \tag{2.3.15}$$

and $L = M = 1.5$, which are the which are the commonly used used values for sheet metals.

2.3.4 Hill'48 Potential Function based on r-values

The Hill'48 potential function having its parameters based on anisotropic r-values i.e. r0, r45 and r90, which are the r-values measured along the rolling, diagonal and transverse directions, respectively. For the potential surface the equation 2.3.10 is used, where the Hill'48 parameters are defined using r-values as:

$$F^* = \frac{r_0}{r_{90}(1+r_0)} \tag{2.3.16}$$

$$G^* = \frac{1}{1+r_0} \tag{2.3.17}$$

$$H^* = \frac{r_0}{1+r_0} \tag{2.3.18}$$

$$N_p^* = N_{3D}^* = \frac{(r_0+r_{90})(2*r_{45}+1)}{2(1+r_0)r_{90}} \tag{2.3.19}$$

and $L^* = M^* = 1.5$, commonly used values for sheet metals.

For the equivalent plastic strain, the equation 2.3.8 is assumed for this study ($d\epsilon^p = d\lambda$).

To calculate the flow direction, the normal directions are calculated based on the potential functions of the Hill'48. The equation 2.3.20 shows the tensor for such normal directions. The amount of the flow is defined by the $d\lambda$ which is to be calculated by stress integration procedure. In matrix form the flow equations are:

$$\frac{\partial \phi}{\partial \sigma} = \begin{bmatrix} \frac{\partial \phi}{\partial \sigma_{11}} & \frac{\partial \phi}{\partial \sigma_{12}} & \frac{\partial \phi}{\partial \sigma_{13}} \\ \frac{\partial \phi}{\partial \sigma_{21}} & \frac{\partial \phi}{\partial \sigma_{22}} & \frac{\partial \phi}{\partial \sigma_{23}} \\ \frac{\partial \phi}{\partial \sigma_{31}} & \frac{\partial \phi}{\partial \sigma_{32}} & \frac{\partial \phi}{\partial \sigma_{33}} \end{bmatrix} \tag{2.3.20}$$

where the components of partial derivatives of potential function are:

$$\begin{aligned} \frac{\partial \phi}{\partial \sigma_{11}} &= \frac{1}{\sigma_{eq}}\left(G^*(\sigma_{11} - \sigma_{33}) + H^*(\sigma_{11} - \sigma_{22})\right) \\ &= \frac{1}{\sigma_{eq}}\left(\sigma_{11}(G^* + H^*) - \sigma_{22}H^* - \sigma_{33}G^*\right) \end{aligned}$$

$$\frac{\partial \phi}{\partial \sigma_{22}} = \frac{1}{\sigma_{eq}} \left(F^* \left(\sigma_{22} - \sigma_{33} \right) + H^* \left(\sigma_{22} - \sigma_{11} \right) \right)$$
$$= \frac{1}{\sigma_{eq}} \left(- \sigma_{11} H^* + \sigma_{22} \left(F^* + H^* \right) - \sigma_{33} F^* \right)$$

$$\frac{\partial \phi}{\partial \sigma_{33}} = \frac{1}{\sigma_{eq}} \left(F^* \left(\sigma_{33} - \sigma_{22} \right) + G^* \left(\sigma_{33} - \sigma_{11} \right) \right)$$
$$= \frac{1}{\sigma_{eq}} \left(- \sigma_{11} G^* - \sigma_{22} F^* + \sigma_{33} \left(F^* + G^* \right) \right)$$

$$\frac{\partial \phi}{\partial \sigma_{23}} = \frac{2 L^* \sigma_{23}}{\sigma_{eq}}$$

$$\frac{\partial \phi}{\partial \sigma_{31}} = \frac{2 M^* \sigma_{31}}{\sigma_{eq}}$$

$$\frac{\partial \phi}{\partial \sigma_{12}} = \frac{2 N^* \sigma_{12}}{\sigma_{eq}}$$

Hill'48 anisotropic coefficients are calculated based on the Lankford coefficient i.e. r-values and based on the yield stresses to obtain potential surface and yield surface respectively.

Table 2.1: Hill'48 anisotropic parameters

based on R-values	based on yield stresses
$F^* = \frac{r_0}{r_{90}(1+r_0)}$	$F = \frac{1}{2}\left[\left(\frac{\sigma_0}{\sigma_{90}}\right)^2 - 1 + \left(\frac{\sigma_0}{\sigma_b}\right)^2\right]$
$G^* = \frac{1}{1+r_0}$	$G = \frac{1}{2}\left[1 - \left(\frac{\sigma_0}{\sigma_{90}}\right)^2 + \left(\frac{\sigma_0}{\sigma_b}\right)^2\right]$
$H^* = \frac{r_0}{1+r_0}$	$H = \frac{1}{2}\left[1 + \left(\frac{\sigma_0}{\sigma_{90}}\right)^2 - \left(\frac{\sigma_0}{\sigma_b}\right)^2\right]$
$N_p^* = \frac{1}{2}\frac{(r_0+r_{90})(1+2r_{45})}{r_{90}(1+r_0)}$	$Np = \frac{1}{2}\left[\left(\frac{2\sigma_0}{\sigma_{45}}\right)^2 - \left(\frac{\sigma_0}{\sigma_b}\right)^2\right]$
$N_{3D}^* = \frac{1}{2}\frac{(r_0+r_{90})(1+2r_{45})}{r_{90}(1+r_0)}$	$N3D = \frac{\sigma_0^2}{2{\tau_{xy}}^2}$

2.3.5 Stress Integration Procedure

To implement the NAFR model into an FE code, the integration of the governing elasto-plastic rate constitutive equations over the time increment is required. The return- mapping algorithm [28] is commonly applied because of its high accuracy and unconditional stability. The general return-mapping method involves elastic prediction and plastic correction. First, an elastic predictor is obtained on the basis of the elastic equations with the total strain increment.

In this section, an algorithm based on fully implicit backward Euler integration is presented. This numerical integration procedure of elasto-plastic problems gained extensive popularity due to its unconditional stability [42]. With this integration procedure, it is essential to use the algorithmic tangent modulus in order to preserve the quadratic rate of asymptotic convergence of Newton method [43]. The used integration algorithm is a strain-driven algorithm where the stress history is obtained from the strain history.

For the purpose of finding the plastic corrector multiplier $d\lambda$ it is required to implement the time integration algorithm to obtain the solution of the constitutive equations described in the previous section. In this work, the convex cutting plane algorithm proposed by Ortiz and Simo [44] and [45] is implemented. It facilitates the implementation of complex anisotropic yield functions over fully implicit Euler backward formulations [20].

- *Evaluate the elastic trial state: Given the incremental strain* $\Delta\bar{\varepsilon}$ and the state variables at t_n.

  $\bar{\varepsilon}^{e\ trial}_{n+1} = \bar{\varepsilon}^{e}_{n} + \Delta\bar{\varepsilon}$
- *Check plastic consistency: Is yielding?*

  If

  $$\Phi = \sigma^{trial}_{n+1} - \sigma_y(\bar{\varepsilon}^{trial}_{n+1}) \leq 0 \tag{2.3.21}$$

  then, **Elastic step:**
  Set $(.)_{n+1} = (.)^{trial}_{n+1}$
- *Return mapping: Plastic step*

  By differentiating eq.2.3.21, the consistency condition is obtained:

$$\frac{\partial f(\sigma)}{\partial \sigma} : d\sigma - \frac{\partial \sigma_y(\bar{\varepsilon}^p)}{\partial \bar{\varepsilon}_p} : d\bar{\varepsilon}^p = 0 \tag{2.3.22}$$

$$d\lambda = \frac{\frac{\partial f(\sigma)}{\partial \sigma} : \boldsymbol{D}^e : d\varepsilon}{\frac{\partial f(\sigma)}{\partial \sigma} : \boldsymbol{D}^e : \frac{\partial g(\sigma)}{\partial \sigma} + h \cdot P(\sigma)} \tag{2.3.23}$$

where, h is the slope of yield curve.

- *Update the state variables*
  After the plastic corrector multiplier $d\lambda$ is obtained, then the trial tress tensor is corrected using,

$$\sigma_{n+1} = \sigma_n - d\lambda \boldsymbol{D}^e \cdot n \tag{2.3.24}$$

- *Exit*

The NewtonRaphson iteration method is often employed to calculate the above non-linear equation. However, it is usually difficult to obtain the numerical solution at a large strain increment and complex deforming processes because of the rate convergence [46], which is more likely to occur for metals with low r-values.

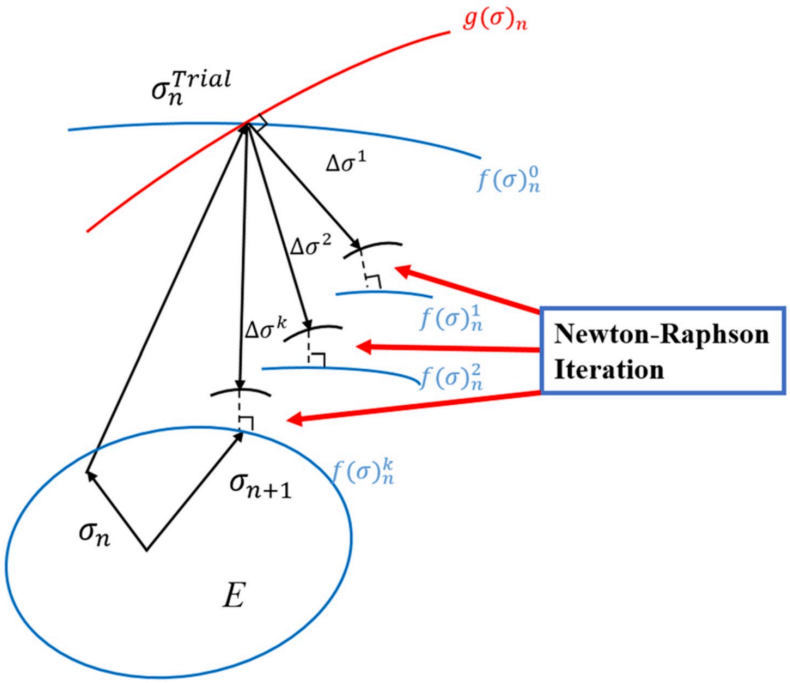


Fig. 2.4: Schematic view of Newton-Raphson Method [28]

For this NAFR model, different mechanical tests are required to identify the parameters to describe both aspects of anisotropy. As mentioned previously, the parameters of the function denoted as Hill'48- f(σ) are determined by using directional yield stresses. Uniaxial tensile tests in longitudinal (0^0, RD), diagonal (45^0, DD) and transverse (90^0, TD) directions to the rolling direction are required to define the directional planar yield stresses σ_0, σ_{45}, and σ_{90}.

3 SPRINGBACK IN ANISOTROPIC SHEET METALS

3.1 Introduction

The use of high-strength steels (HSS) and aluminum alloys in industry such as the automotive is creating forming challenges for tool and die engineers. Meeting the dimensional specifications to produce parts made of these materials is difficult and can require expensive tryout loops. The higher strain hardening of HSS compared to mild steel and the aluminum alloy low stiffness property result in a significant increase in elastic springback. Springback, the elastically-driven change in shape of a part upon unloading after forming, is a concern as manufacturers increasingly rely on materials with higher strength-to- modulus [47].

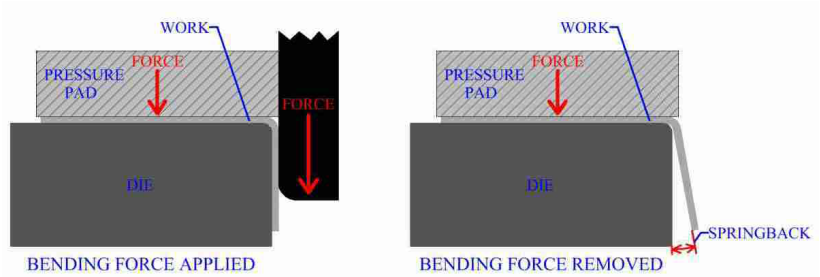


Fig. 3.1: Springback in Bending

The Figure 3.1 illustrate the phenomenon of springback in bending process. Springback is the geometric change in the part at the end of the forming process when the part has been released from the forces of the forming tool. Upon completion of sheet metal forming, deep-drawn and stretch-drawn parts spring back and thereby affect the dimensional accuracy of a finished part. The final form of a part is changed by springback, which makes it difficult to produce

the part with the intended accurate geometry. As a result, the manufacturing industry is faced with some practical problems: firstly, prediction of the final part geometry after springback and secondly, appropriate tools must be designed to compensate for these effects.

Through the application of new materials, the number of problems increases. Forming parts made of these materials are more affected by springback than parts made from conventional deep-drawn steel. Concerning classic sheet metal defects such as splits and wrinkles, strain in the sheet metal is decisive. If springback occurs, such models are not enough to predict elastic recovery. In this case, the stresses are decisive and a considerably higher accuracy is crucial.

3.2 Springback in bending

Springback is a sheet metal behavior, which must be addressed when bending sheet metal. It occurs because there is always an elastic region (albeit, sometimes very small) within the sheet which wants to return to its original state after the bending operation. The springback of the bent sheet can be approximated using the expression shown in equation 3.2.1. This equation was deduced by analyzing the bending process as a pure flexion problem, assuming that for Ri > 2.t the neutral axis is located at the center of the sheet thickness and that the applied bending moments generate a plane strain [48].

$$\frac{R_i}{R_f} = 4(\frac{R_i Y}{Et})^3 - 3(\frac{R_f Y}{Et}) + 1 \tag{3.2.1}$$

where:
R_i Initial bending radius,
R_f Final bending radius,
Y Yield stress of the material,
E Young Module of the material,
t Sheet thickness.

A bi-dimensional analysis of sheet bending and corresponding springback can be easily approximated by expressions like 3.2.1. However, when 3D complex

geometries are analysed, simple expressions cannot be used and finite element analysis can give the answers to better understand and predict the final geometry of a stamped component after being released from tools. In the next section an automobile component will be presented, which was object of a benchmark challenge to finite element codes in order to predict the final geometry of an aluminum part and the comparison of selected sections to experimental measurements.

On the objectives of this study it was included not only the possibility of performing simulation at the level of current challenges for numerical modelling of sheet metal forming processes and predicting the stamping of an industrial component by using practical stages of binder closure, forming, trimming and springback, but also giving a contribution on the understanding of dispersion of results, variability of comparisons and discussing the associated uncertainties of results, a topic which is not recent but shall be continuously further developed, so that accuracy and validation of numerical results goes in parallel with experimental developments and standardization. Nowadays, with current higher level of finite element modeling this is a fundamental topic and there is a need on the highest level of confidence on experimental data, so that different methodologies and numerical approaches shall be confronted and new developments be validated with the greatest level of accuracy.

3.3 Benchmark study of an automotive panel

The forming analysis and springback for the selected component in this section corresponds to a proposed benchmark by NUMISHEET 2016 [34]. NUMISHEET is a bi-annual conference series on Sheet Metal Forming. This conference, besides featuring the usual sessions, is also including a benchmark session, during which numerical simulations of sheet formed parts are proposed and codes are challenged on its prediction and accuracy by comparison with state-of-the-art experimental results from the industry and academia.

3.3.1 Forming process

This is the most important stage of the FEM simulation to define the process. In this stage it was defined the total press stroke, which corresponds to 500 mm. Then defining the tool offset equals to the thickness of blank i.e. 3 mm. Here the punch and die are already containing the offset distance. The lubricating condition is to be defined in this section. The coefficient of friction used is 0.14.

To hold the blank at the right position during the drawing operation the pilots were defined on the binder surface. While defining binders there is a need to care if they are not intersecting and locking the blank.

The CAD models, material description, deep drawing process variables and boundary conditions are provided for the aluminum panel. The simulation conditions are the part of the benchmark provided by NUMISHEET [34] for the Springback of a Jaguar Land Rover Aluminum Panel which is shown along with the tool assembly in the figure 3.2.

The springback stage of this study includes a previous stage of one single forming operation and a trimming step. Cross-sectional profiles need to be analysed at specific (provided) sections in the part before and after springback. The tool geometries, material properties, and the simulation parameters are provided.

3.3.2 Forming simulation

The forming of a Jaguar Land Rover Aluminum Panel is done using a commercial FE code AutoForm. The geometries of punch, die, blank, blank holder (binder) and trimming curve are carefully positioned as per the requirement of the NUMISHEET benchmark. The total assembly is as shown in the figure 3.2.

The simulations consist of different stages:

- Binder Closure: Closing of the die and binder;
- Forming: One step forming;
- Trimming: Profile trimming with the trim curve tool;
- Springback: Measurement of the springback;
- Springback Analysis: Exporting defined section curves profile for the

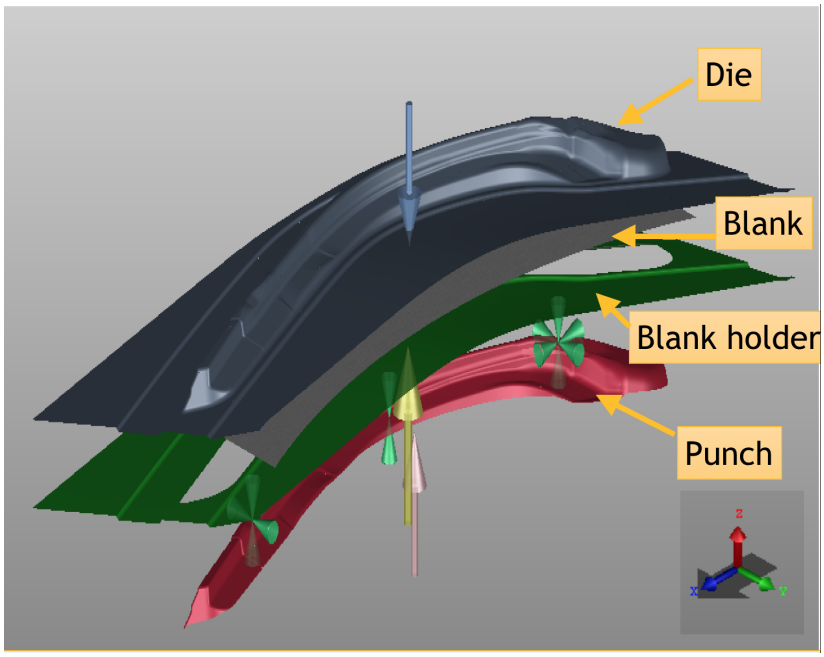


Fig. 3.2: Assembly setup

springback analysis;

- Punch force Analysis: Exporting Punch force vs. Die stroke data;
- Thickness Analysis: Exporting Blank thickness after forming at defined sections.

3.3.3 Element type

The shell element with the maximum number of 11 layers has to be used, if springback is to be analyzed after the forming simulation. This is necessary because springback results have proven to be extremely sensitive with respect to the smallest inaccuracies in the calculation of internal stress state. Hence, Element type EPS-11 is used. The schematic of EPS-11 element is shown in the figure 3.3 (EPS-11: Elastic plastic shell element with 11 layers.)

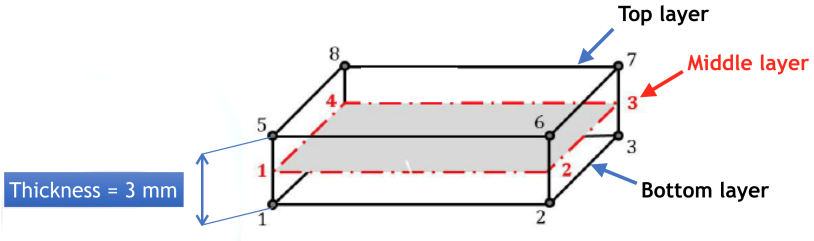


Fig. 3.3: Schematic of Top, Middle and Bottom layer of the Element

3.3.4 Material properties

The blank material to be used in this study is the aluminum alloy (AA6451-T4) with thickness t = 3.0 mm. The elastic mechanical properties are given in table 3.1. The uniaxial tensile yield stress and r-values are given in table 3.2.

Table 3.1: Elastic mechanical properties

Sample	**Density,** $\rho(g.cm^{-3})$	**Young's modulus, E (GPa)**	**Poisson ratio,** ν
AA6451-T4	2.7	68.9 GPa	0.33

Table 3.2: Uniaxial tension test data

test direction	**YS,** σ_{yld} **(MPa)**	**r-value**
0^0	151.28	0.62
45^0	171.2	0.33
90^0	163.6	0.8

Table 3.3: Equal biaxial tension test data

σ_b **(MPa)**	**r-value,** r_b
153.6	0.55

The equal biaxial tensile yield stress and biaxial r-value are given in table 3.3.

The material constants for the hardening curve at 0 degrees from the rolling direction (RD) are described in Table 3.4 for the Voce hardening law.

Table 3.4: Hardening curve

Voce		
A, (MPa)	**B, (MPa)**	**C**
359.093260	196.310139	9.374256

The Voce hardening curve gives a better fitting to the experimental results at 0 degrees from RD. The material constants for Barlat's Yld2000-2d yield function are provided in table 3.5. The eight anisotropy coefficients and the material constants for Barlat's Yld89 yield function are provided in table 3.6.

Table 3.5: Material constants for yield function Yld2000-2d (a = 8.0)

Sample	α_1	α_2	α_3	α_4	α_5	α_6	α_7	α_8
AA6451-T4	1.06517	0.84189	0.96006	0.95865	1.03404	1.02711	0.83899	0.87703

Table 3.6: Material constants for yield function Yld89 (m = 8.0)

Sample	a	c	h	p
AA6451-T4	1.3033	0.9556	0.9247	0.8465

3.3.5 Boundary conditions

Table 3.7: Boundary conditions for forming and trimming operations

Part	**Operation**			
	Binder Closure	**Forming**	**Trimming**	**Springback**
Die	Z-Disp:-300 mm	Z-Disp:-200 mm	Clamped	
Binder	Clamped	BHF:1900 kN	Clamped	
Blank	Free	Free	Free	Boundary condition
Punch	Clamped	Clamped	Clamped	

When performing springback analysis, there are three boundary conditions at which the movement of the blank is restricted. The three boundary conditions are at the defined sections at points, A,B and C as shown in the figure 3.4 and they are presented in table 3.8.

Table 3.8: Boundary Conditions

Point	Boundary Condition	Coordinate
Point A	Pin	$\delta x = \delta y = \delta z = 0$
Point B	Simply supported	$\delta x = 0$
Point C	Slot	$\delta y = \delta z = 0$

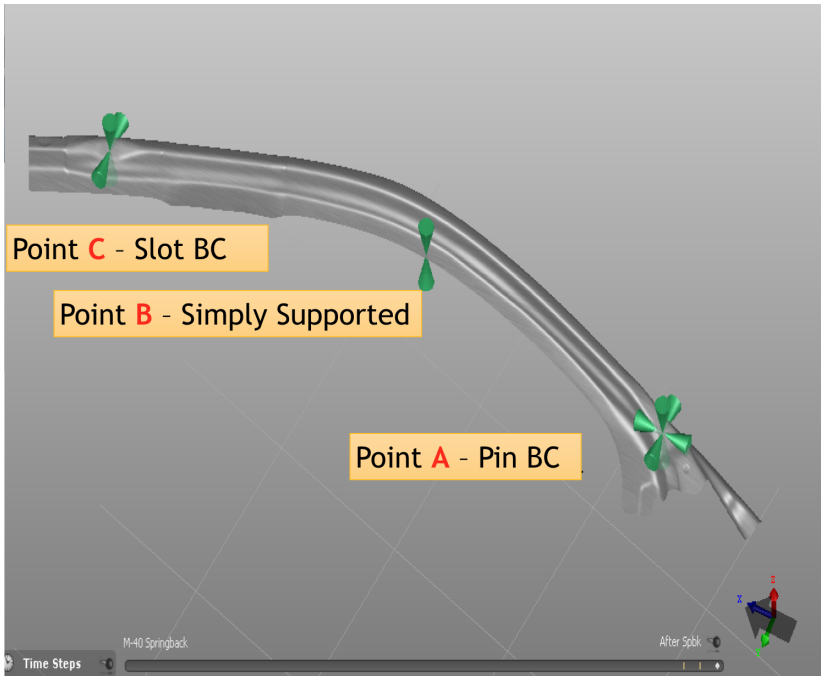


Fig. 3.4: Defined boundary condition for springback [34]

3.4 Benchmark results of section profiles for planes as defined by Numisheet

According to the General Description for report on Benchmark 2 Springback of a Jaguar Land Rover Aluminum [49] three planes (figure 3.5), as defined in table 3.9, in addition to a provided local coordinate system, are used to obtain the sections for analysis of results.

Table 3.9: Defined normal vectors for the section planes

Normal Vectors	X	Y	Z
Sec-A (sect I)	-0.985572	0.100936	-0.135870
Sec-B (sect III)	-0.997984	-0.062806	0.009108

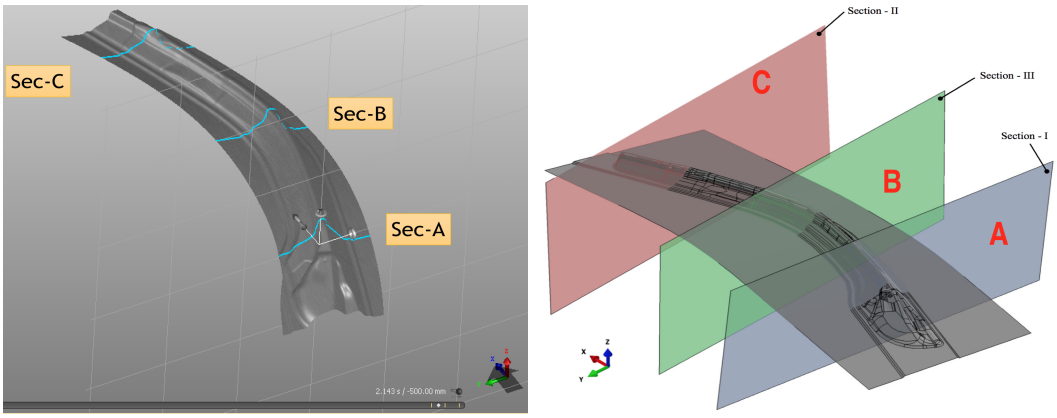


Fig. 3.5: Defined sections for analysis [49]

Each numerical participant on this benchmark had to provide his own data of results of the resulting section profile from the predicted final geometry of the component, after springback. The collection of results from each numerical participant gave the possibility to obtain the comparison of numerical results and the difference to the provided experimental section profile.

3.4.1 Numisheet results after springback

It is presented in figures 3.6 and 3.7 the published FE results of profiles for sections A and B, respectively, obtained from the participants in this benchmark and the comparison with experimental measured data, which is available for after springback stage and also for after forming stage. In these figures, one of the numerical participants (DD3-UC) is highlighted, because their results will be used in the next sections, on the analysis of this benchmark.

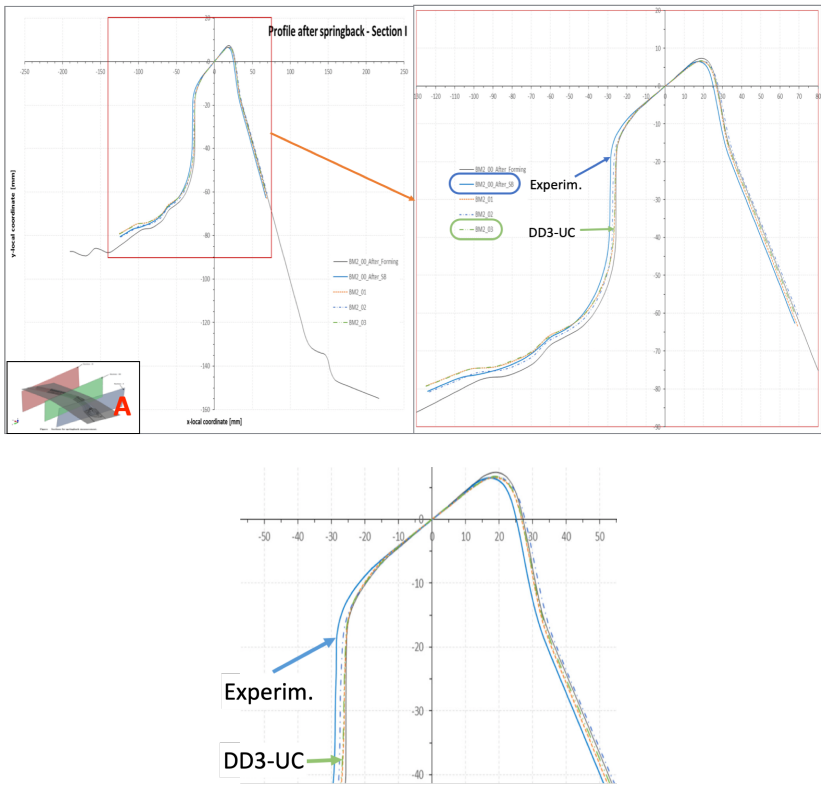


Fig. 3.6: Numisheet results - Local converted 2D frame - Section A, after springback [49]

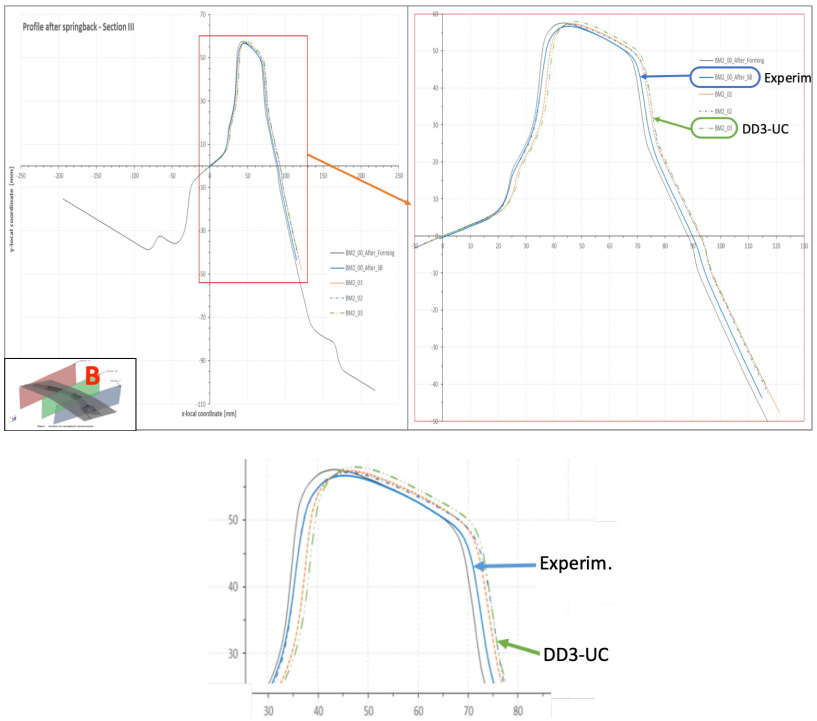


Fig. 3.7: Numisheet results - Local converted 2D frame - Section B, after springback [49]

To obtain the presented section profiles in 2D local coordinates, the 3D coordinates of the sections need to be transformed from global coordinate system to the local defined coordinate system. The relationship between these two coordinate systems can be seen in figure 3.8. This visualization and the related transformation correspond to a script developed in MatLab, with the special objective of assuring and performing this fundamental task.

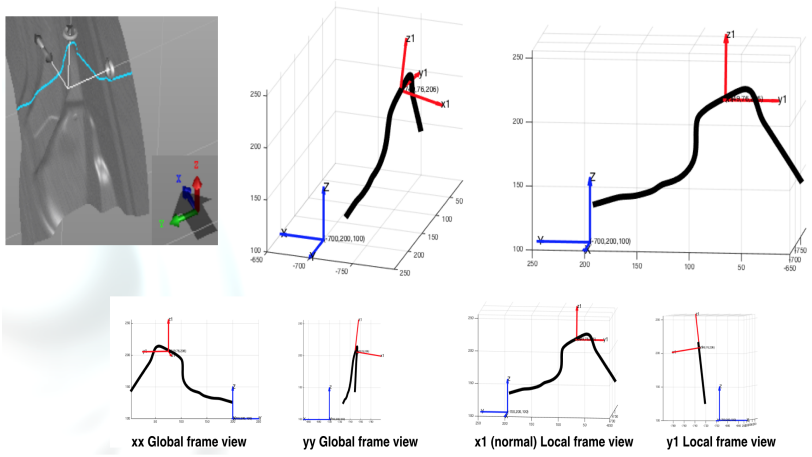


Fig. 3.8: Local converted 2D frame - Section A, after springback

When analyzing the results from both figures 3.6 and 3.7 for sections A and B it is difficult to find repeatability of profiles from numerical results and specially it is seen that none of them is following the reference results. In case of section A (figure 3.6) it is observed that numerical profiles are much closer to the reference profile after forming than the profile after springback, which is opposite to what would be expected. In case of section B (figure 3.7), the results show that the numerical profiles define a group which is closer and the reference profile is somewhat far away. Although not presented here, the same tendency, observed in sections A and B, was found in section C for results.

These observations were a starting point to investigate and be able to get directions for explanations on these diverging results between experiments and numerical simulation for this BM2 Numisheet2016 benchmark. With this kind of output, the main objective of benchmarks, which is the validation of numerical results was not possible to go forward.

The methodology to be followed, for an understanding of such results, was to perform numerical simulation by using AutoForm FE code and in parallel

to interact with one of the BM2 Numisheet2016 participants, the group from University of Coimbra, M.Oliveira at el. with DD3IMP code [50].

As main characteristics, the finite element code DD3IMP (Deep-Drawing 3D Implicit code) has been specifically developed to simulate sheet metal forming processes. The evolution of the deformation process is described by an updated Lagrangian scheme. An explicit approach is used to calculate an approximate first solution for the nodal displacements, the stress states and frictional contact forces. A r-min strategy is implemented to impose several restrictions on the size of the time increment in order to improve the convergence. The first trial solution is iteratively corrected, using a NewtonRaphson algorithm, finishing when a satisfactory equilibrium state in the deformable body is achieved. It is then possible to update the blank sheet configuration, as well as all the state variables, passing on to the calculation of the next time increment and this is repeated until the end of the process [51–53].

3.4.2 Comparison of results after springback, AF-UP vs. DD3-UC

In this section the BM2 simulation results from AutoForm code will be compared with results from DD3IMP code. The results from AutoForm will be referred as AF-UP, while DD3IMP will be referred as DD3-UC. The section profiles will be compared for Numisheet BM2 proposed sections A, B, C, and the profiles were plotted in the defined local 2D coordinate system. Additionally, each section was treated independently and some translation for an individual profile was performed with a best close fitting, optimizing their matching. Also, the available 2D experimental data was included in this comparison with the two numerical profiles. The profile from AF-UP is offset by half of sheet thickness (1.5 mm) so that a more efficient comparison is possible, thus being both visible and not coincident, in case of perfect matching.

Figures 3.9, 3.10 and 3.11 show the corresponding results for sections A,B, C, respectively. As seen from figure 3.9, for section A, the numerical profiles agree closely on the right part of the profile (there is an intended offset of 1.5 mm), both of them following also the experimental profile. On the left part of profile numerical results differ and DD3-UC shows a higher springback, while

experiment is somewhat in the middle of numerical results. An interesting observation can be seen on top part of profile (center), which shows that the experimental profile doesn't match with the numerical profiles. While the numerical profiles follow a tendency of matching each other (by offset) along most of the profile, even at the top part, this is not the case for experiment at the top region. The only explanation for such behavior is that experiment does not belong to the same section or local frame of reference as the numerical profiles.

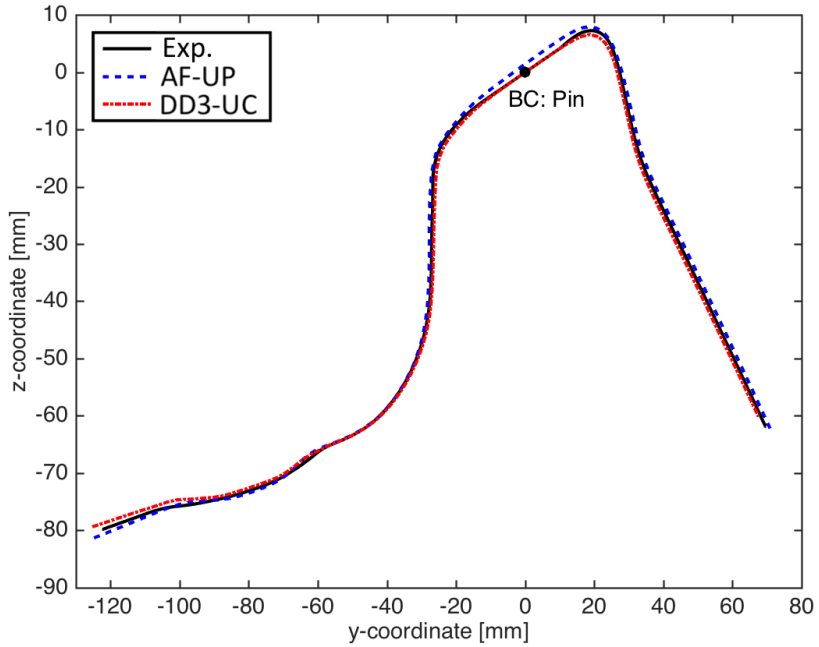


Fig. 3.9: Section A, After Springback - numerical and experimental profiles, using local 2D coordinate system; AF-UP=AutoForm code, DD3-UC =DD3IMP code; AF-UP is offset by 1.5 mm.

Now, analyzing figure 3.10 it is seen that every profile is matching closely, even the experimental profile is coincident with DD3-UC results. AF-UP follows closely (with offset) previous results, but a slightly higher springback differentiates its geometry on the right side (opposite side of BC restriction). To be noted that length of right side profiles is different: AF-UP vs DD3-UC vs experiment. The different length cannot be easily understood, due to the fact that the previous stage to springback (tools released) is the trimming operation, in which the sheet dimensions get standardized. A possible explanation is some material flow during stages and also to the fact that pivots were defined differently for each FEM simulation, as it may be explained in next text section.

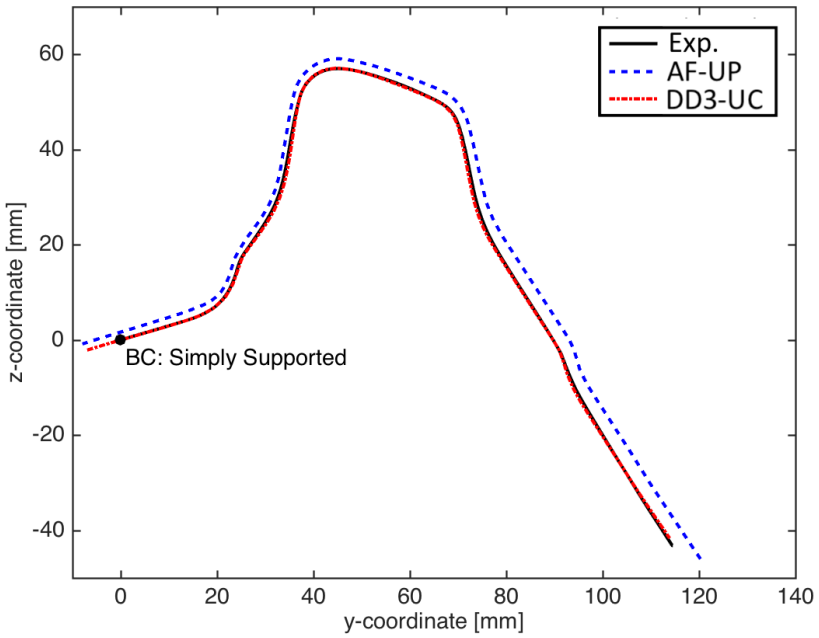


Fig. 3.10: Section B, After Springback - numerical and experimental profiles, using local 2D coordinate system; AF-UP=AutoForm code, DD3-UC =DD3IMP code; AF-UP is offset by 1.5 mm.

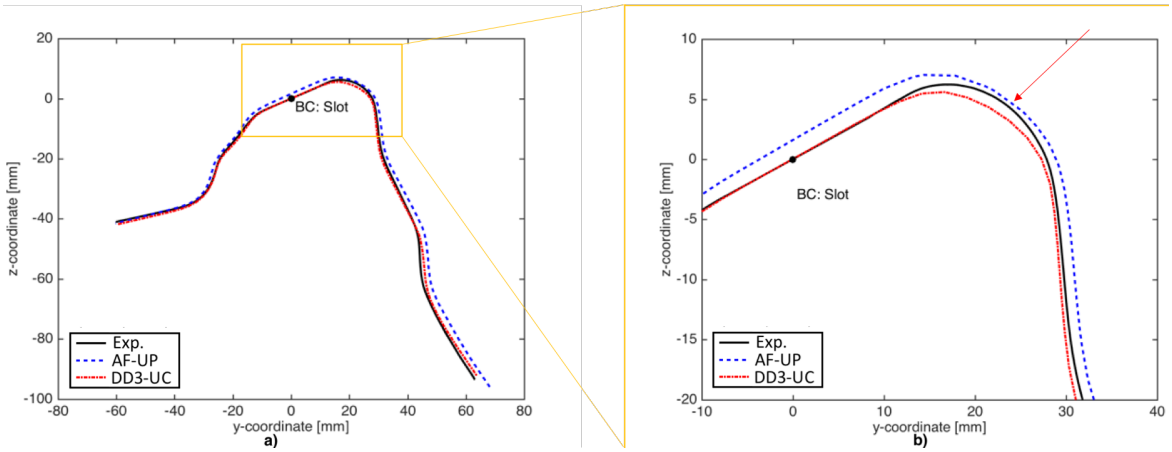


Fig. 3.11: Section C, After Springback - numerical and experimental profiles, using local 2D coordinate system AF-UP=AutoForm code, DD3-UC =DD3IMP code; AF-UP is offset by 1.5 mm.

Seeing section C, figure 3.11, it shows that AF-UP and DD3-UC numerical profiles follow each other very closely on the top surface, where BC restriction is defined. It is also understood the existence of a similar comparison to what seen in section A: the right side of profile shows a good matching between numerical profiles, while the left side shows a different springback behavior; however, again the experimental profile is not following the tendency of numerical profiles, now not only on the top surface, but also in the right part of profile. Again,

this reinforces the previous understanding that the cutting plane (and local coordinate system) for experimental profile is not the same as the one used for numerical profiles. This is perfectly highlighted when seeing in more detail the top view of profile, figure 3.11 b), which shows a different radius of curvature for the experimental profile, when compared to numerical results.

3.4.3 Analysis of blank draw-in, AF-UP vs. DD3-UC

When analyzing final results for a sheet stamped par, such as the geometry after springback and trying to understand why differences exist, one should be aware about all the loading history the material has undergone and that any difference on final results and final distribution of strains and stresses can be due to different flow of material and plastic loading paths. Therefore, it was decided to perform a comparison of results for the initial stage of forming: the draw-in operation.

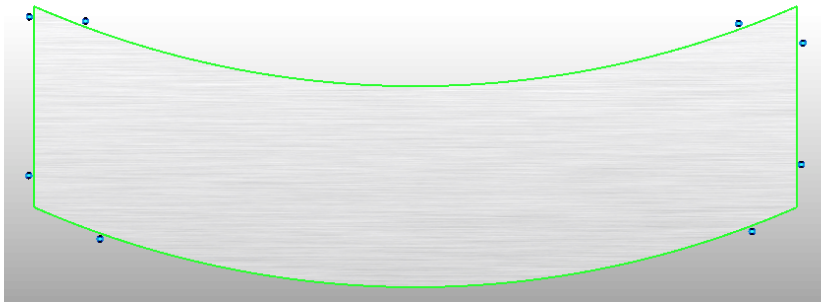


Fig. 3.12: Blank position with pivots after blank holding.

According to the proposed recommendation for BM2 the blank is to be placed in over the blank holder. To keep the blank in the right position eight pivots were defined as shown in fig. 3.12. As the NUMISHEET benchmark didn't provide information regarding the pivots, this is already a reason for a possible difference in the positioning of the blank and a possibility for results having differences. Figure 3.13 shows the total draw-in, before the trimming operation for numerical results of AF-UP. An efficient method to compare the draw-in between different codes id to use the free edges of blank and, in this case, to use the xy plane to plot the contours.

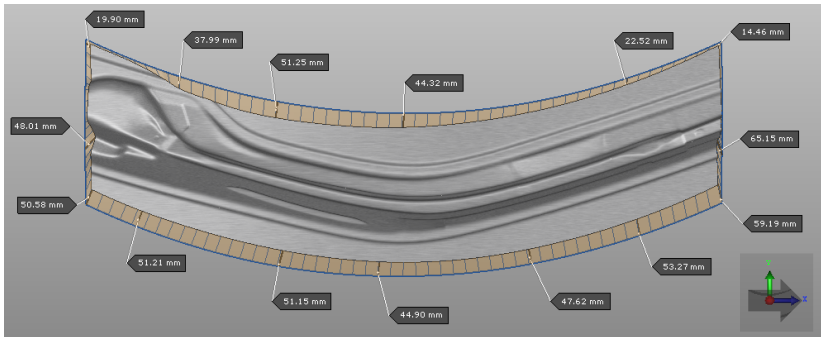


Fig. 3.13: Blank draw-in for AF-UP simulation.

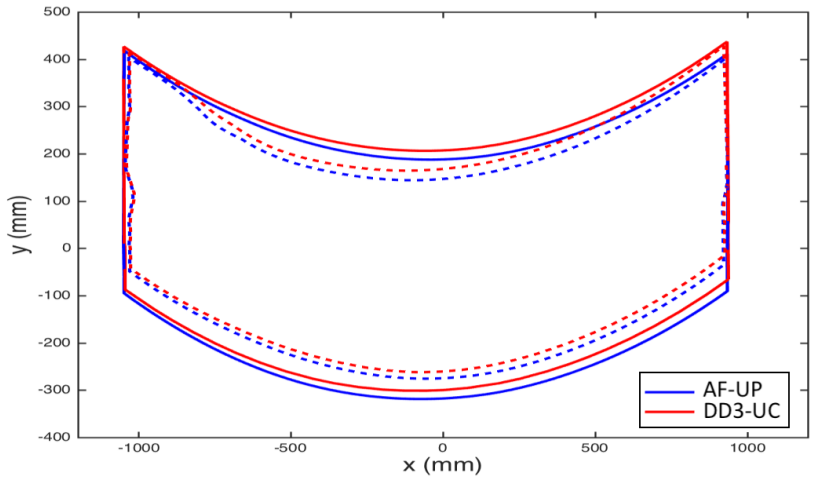


Fig. 3.14: Blank position before and after binder closure.

Figure 3.14 shows the free edges of blanks during the first stages of forming operations (blank holding and forming) with AF-UP and DD3-UC simulations. The outer boundary of the blank is not matching between different codes. This is explained by the different position of the pivots to hold the blank and therefore to a different positioning of the blank. As a consequence, this will give different blank positions after forming with numerical simulations of different codes. This can be clearly seen from the figure 3.15, which shows the two numerical simulations starting with the same initial blank position as shown in the figure 3.15 i) (on the left) and then, when the blank is held against the binder then the two blanks flow (deform) differently, which can be seen by a different position in figure 3.15 ii). Also, after forming, figure 15 iii) (on the right) the blank position keeps a similar difference in draw-in. This different positioning between AF-UP and DD3-UC simulations have possible influence on final results. A study on different results for experimental benchmark [54, 55] has shown that even for simple geometries the different flow of material with bending and unbending

loading causes a different loading history in a part of the blank, which will cause visible differences in final geometry after springback.

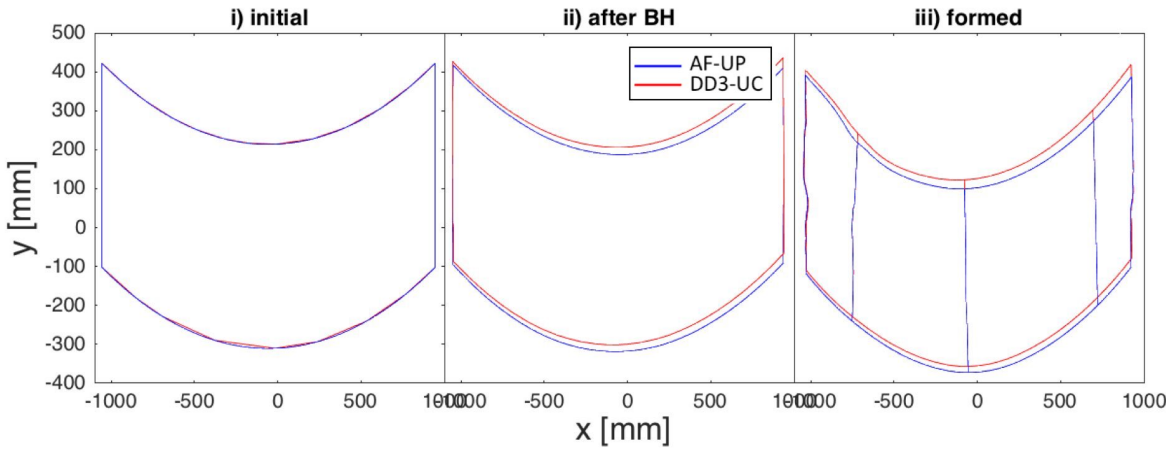


Fig. 3.15: Blank position after blank holding and forming.

3.4.4 Discussion of results

The comparison of 3D complex geometries, after springback, obtained by sheet metal forming is not a straightforward task. Even simpler to perform, the 2D geometries may sometimes give some challenges on such comparison and on the repeatability of results [54,56,57].

As seen from figures 3.6 and 3.7, BM2 from Numisheet, and the comparisons between numerical and experiment results don't give possibilities for definite conclusions on the capabilities of numerical predictions and for validation of the numerical approaches, since the experimental results dont match with numerical defined profiles. On the other hand it must be highlighted that FE simulation results are in a high level of competence, since they all offer a predicted similar tendency, not only among them but also to the experiment, for a challenging practical industrial problem with several different stages of production.

With this level of competence for simulation, a step forward it is to look for additional accuracy and increasing the scale level of requirements. For such objective and for purpose of validation, the experiments must also increase the level at which dispersions and inaccuracies exist. From the research study of previous sections, it was seen that some explanations exist for results having differences and dispersion. The conditions for which BM2 of Numisheet were

required didn't prevent two type of possible incorrections. The first one is the definition of sections and local planes or coordinate systems, which required conversions and transformations, thus being possible a non-objective output of measurement data and adding uncertainties to results. A second possibility for dispersions or incorrections is due to the positioning of blank or different restrictions to the flow of material, with consequences on different loading paths for some parts of the sheet and possible strain and stress distribution.

Being aware of previous analysis, although understanding that other directions could or should be done for a wider justification of dispersions, just using common sense it would be suggested:

- to find the simplest procedure for positioning the complex part in the right points to support the part is of primordial importance, taking into account the need for reproducibility of experimental parts to be measured and having a selected experimental fixture to do it; accordingly, numerical parts will just follow the same standardized procedures as experiments;
- to use measurement data and get point coordinates from a unique global coordinate system, thus guarantying that a standard method for measurement exists and minimizing any need of conversions of transformations;
- when several stages to process the part exists, besides having results from final geometry, it would be important having the results from each of the processing stages; even if experimental data would be difficult to obtain after each stage; just the comparison of numerical results for such stages would give a much wider understanding on the obtained final results; for example for presented BM2 results, figures 3.6 and 3.7, it is seen that experimental profiles after forming are available, which would give the possibility to compare with numerical results, e.g., draw-in after forming;
- although other directions could be considered, another point is highlighted for experiments, which is the associated uncertainty of such results that should be included: how many specimens have been used for measurement? What is the level of dispersion for results? what is the uncertainty for validation?

In the next section, a comparison of results will be performed between the two codes of current investigation, in which two of the previous points will be followed: the use of global planes (and global coordinates), as well as the use of

comparison of results from each stage of part processing.

3.5 Benchmark results of section profiles using global planes

Figure 3.16 shows the comparison of predicted BM2 numerical geometries, after springback, of the results obtained by AutoForm (AF-UP) and DD3IMP (DD3-UC). This is performed by a post-processing software, NXT Defect Evaluator 5 [58], and the distances between geometries are defined by contours of positive and negative values.

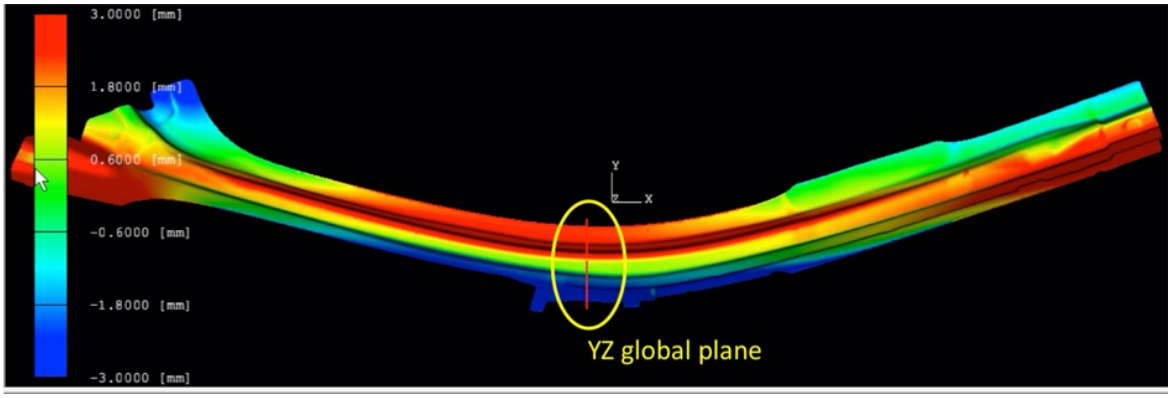


Fig. 3.16: AF-UP and DD3-UC predicted geometries and corresponding distance evaluation after springback [58]

As seen, this comparison of complex geometries, as an overall analysis, by itself permits already a better understanding on the differences on numerical predictions, being visible that the main differences on springback prediction is in the center region of the part as well on the left region. In the same figure it is presented at the center region a global plane (YZ plane), which will be used for comparison of results in the next figures. This global YZ plane permits a direct plot of 3D coordinates of the sections thus avoiding any transformation and/or rounding off errors that may occur and an efficient comparison.

3.5.1 Section profile before forming

In figure 3.17 it is shown the comparison of numerical results between AF-UP and DD3-UC, after the initial stage of blank holding. As seen, it is visible the

different draw-in obtained from each code, due to different positioning or blank restrictions during this first processing stage, which goes according to what has been already seen in figure 3.15 ii).

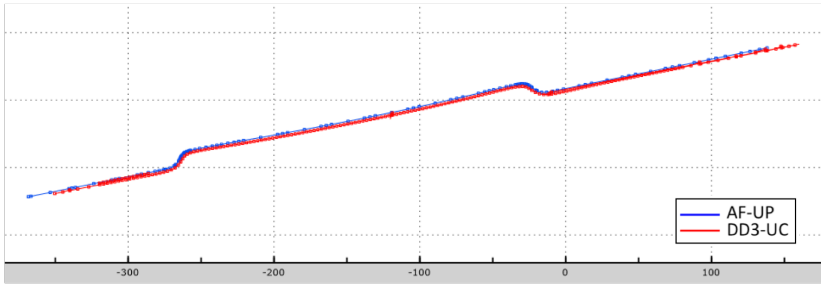


Fig. 3.17: YZ section profile after blank holding stage; section in YZ global plane defined in figure 3.16.

3.5.2 Section profile after forming

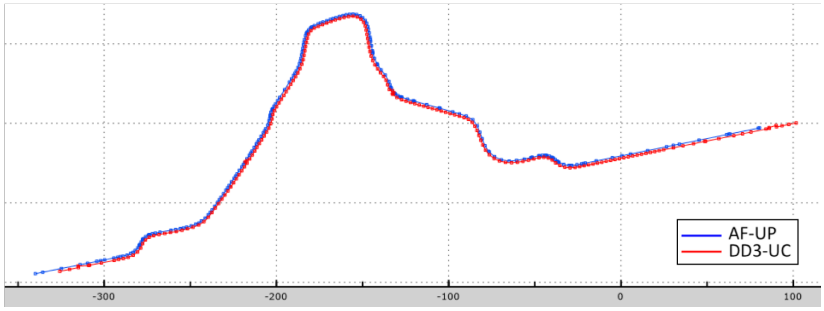


Fig. 3.18: YZ section profile after forming stage; section in YZ global plane defined in figure 3.16.

Figure 3.18 shows the two section profiles from AF-UP and DD3 after forming and they show a perfect matching, since their geometry is being defined by the geometry of tools, which, as expected, shall be the same. As in previous stage of blank holding the material draw-in is different from each code, as already seen in figure 3.15 iii).

3.5.3 Section profile after trimming and before springback

The predicted profiles from each of the two simulations are presented in figure 3.19, after the trimming stage. As in case of the geometries after forming, the matching between the results is complete (geometry being defined by geometry

of tools), except on the length of profile, which is higher for AF-UP. This observation goes according to what was already seen in figure 3.10.

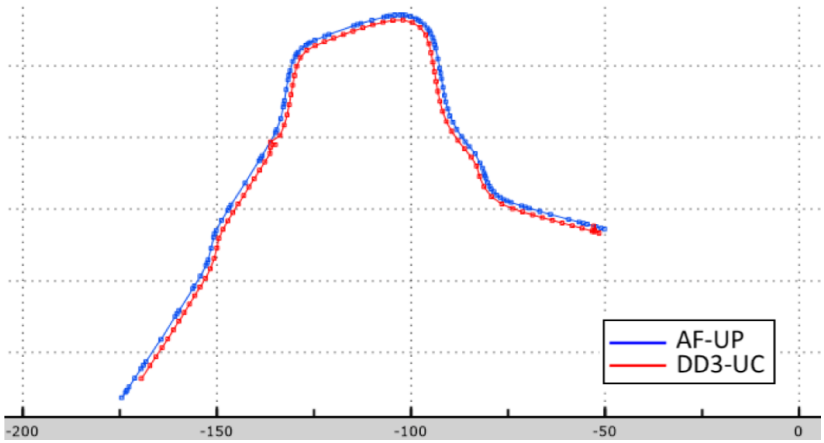


Fig. 3.19: YZ section profile before springback; section in YZ global plane defined in figure 3.16

3.5.4 After springback

The final geometries after springback are shown in figure 3.20. From this figure it is seen that the two profiles dont show so much difference on the their opening, due to springback, which is also according to what was presented in figure 3.10. However, there is an evident translation between the two profiles, which means that the springback acted (or can be seen) more differently in XY plane view. This observation also redirects to the difficulty of analyzing differences

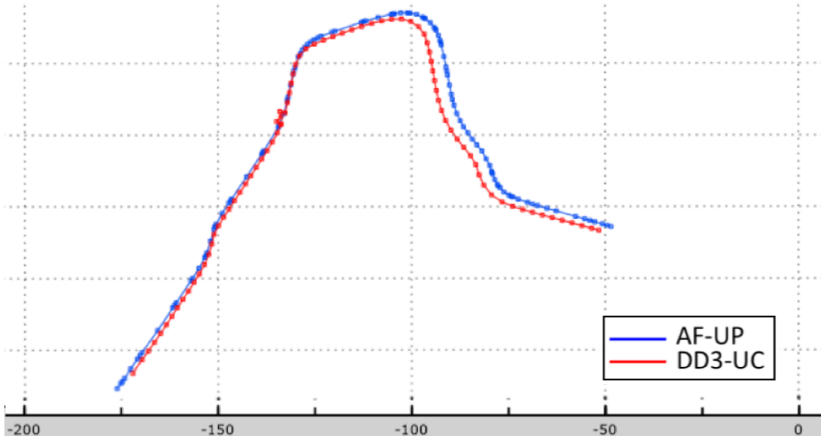


Fig. 3.20: YZ section profile after springback; section in YZ global plane defined in figure 3.16.

of complex 3D geometries and the limitations of 2D comparisons, in addition to the challenge of finding the best sections for geometry comparison after

springback. This observed translation could be already understood in figure 3.16, in which the complete part and contours of geometric distance show that there a positive (red) displacement between simulations, while on the other side there is a negative (blue) displacement between predicted geometries.

3.5.5 Discussion

Published results from Numisheet2016 BM2 with comparisons of final profiles, after springback, of numerical participants and experiments show that analysis and comparisons of complex 3D geometries is a challenging task, which shall be overcome using simple but efficient methodologies, in parallel with the best technologies for measurement and digital data comparison. Advances in this topic corresponds, also, to an important direction towards reference experimental results for validation of advanced numerical approaches, so that the needed level of accuracy is compatible with current level of results from numerical FE modelling.
In current investigation it was possible to understand some of the reasons why Numisheet BM2 results didnt give the complete intended numerical validation answers that were expected. The performed analysis gave the possibility to redirect the use of some guidelines, which may support some directions to follow, when comparison of complex geometries needs to be performed.

This chapter was dedicated to springback analysis, but the main focus was directed to state-of-the-art benchmark simulation, in addition to challenges of numerical validation with experimental results.

This same topic of springback analysis will be referred again in chapter 5, but with a different perspective of developments in numerical approaches for improvements on accuracy and better prediction of the final geometry of a sheet stamped part, namely by using different anisotropic constitutive models.

4 NON-ASSOCIATED PLASTIC FLOW MODEL EVALUATION

4.1 Introduction

Several anisotropic yield functions have been proposed for sheet metal forming based on the Associated Flow Rule (AFR) hypothesis, in which the yield function determines both the flow direction and yielding, simultaneously. The Hill quadratic function (Hill'48) is the most frequently used yield criterion because of its simple form and identification of parameters. It has been proposed as a generalization of the von Mises yield function (J2) for anisotropic materials [15,59]. In fact, this Hill'48 quadratic yield function has some limitations and in some cases its results cannot describe the observed simultaneous behavior for both the anisotropic yield and the anisotropic strain of sheet metals [60]. The use of advanced constitutive equations has been a research direction to overcome these limitations and numerous yield criteria have been developed [60–63].

The use of these advanced constitutive equations, comes also with incorporating more coefficients to the yield criterion, which turns the parameter identification process more complex, with the need of more experimental data, time and computational cost. Generally, the proposed models have been developed and are based on the associated flow rule (AFR), following the classical normality rule, in which yield function and plastic potential function are identical.

As an alternative to more advanced models and complex parameter identification some effort has been made on the use and development of methods based on the non-associated flow rule (NAFR), in which plastic yielding and plastic flow is described by two independent functions. The use of NAFR suggests a simple and flexible means of simulating the complex relationship between

yield behavior and plastic flow and this is the motivation to be incorporated in current research.

Despite these proofs, the direct justification of non-associated flow application still remains an open issue due to the difficulty in experiment based direct measurement of the plastic flow [33, 47]. However, as initiated by [11], the non-associated quadratic anisotropic models received increasing attention in recent years, which is mainly driven by its efficiency and simplicity. Compared to the associated quadratic models, it improves the anisotropic characteristic predictive capability to a similar level as the advanced non-quadratic associated anisotropic models.

Sheet metals generally exhibit a considerable anisotropy due to their crystallographic texture. The mechanical anisotropic characteristics of the sheet metal have a great influence on the shape of the specimen after the deformation. Therefore many successful phenomenological models have been proposed for use in Finite Element (FE) codes to simulate the anisotropic behavior of a material. The anisotropy is mainly described on the basis of initial Lankford coefficients and/or yield stresses along the orthotropic axes of the sheet metals. The different yield functions make use of different combinations of these parameters to represent a three-dimensional surface determining the transition between elastic and plastic deformation [64].

This study mainly focuses on the following goals:

- Implementation of an Anisotropic Material Model based on non-associated flow rule.
- Implementation into a user material VUMAT subroutine for the commercial finite element code ABAQUS.

Having in mind these objectives, the following steps will be considered:

- Yield function and plastic flow are to be defined i.e. Hill'48 anisotropic yield function in parallel with Swift or Voce hardening laws;
- Coefficients for Yield functions to be determined from yield stresses;
- Coefficients for the plastic potential to be determined from the r-values;
- Computational plasticity equations to be formulated using return mapping algorithm to integrate the stress over each time increment;

- To implement the material model to simulate sheet metal forming process;
- Comparison of the results between associated and non-associated models;
- Experimental validation of the model;
- Sensitivity analysis to numerical variables of model (e.g. mesh size) and to parameters from yield functions.

To implement and verify the constitutive equations and the Non Associated Flow Rule methodology, the material user subroutine (VUMAT) was developed in FORTRAN language to implement it with Abaqus solver. In the next sections the validation of the implementation is done at first for a single element case and next to a cylindrical cup case.

4.2 Selected sheet materials

Three materials have been selected, i.e. AA2090, AA6061 and SPCE steel. The selection has been performed in order to compare results with the bibliography.

4.2.1 Mechanical properties

Concerning selected alloys, the respective mechanical properties and the Hill48 parameters are presented in tables 4.1 to 4.6.

In this study aluminum alloy AA2090-T3 is used. The mechanical properties of AA2090-T3 sheets given in table 4.1.

Table 4.1: Material properties of AA2090-T3

Sheet thickness	1.60 (mm)				
Young's modulus	69 000 (MPa)				
Poisson's ratio	0.33				
Stress-strain curve	$\sigma_y(\bar{\varepsilon}^p) = 646(0.025 + \bar{\varepsilon}^p)^{0.227}$				
R-values	r_0	r_{45}	r_{90}		
	0.2115	1.5769	0.6923		
Yield stresses (MPa)					
σ_0	σ_{45}	σ_{90}	σ_b	τ	
279.6	226.9	254.5	289.4	131.4	

*Material properties from Yoon at el. [65].

The values of Hill'48 anisotropic coefficients are calculated using the expressions

shown in table 2.1 to obtain potential surface and yield surface respectively. The two set of such Hill's parameters values are shown in table 4.2.

Table 4.2: Values of Hill'48 parameters for AA2090-T3

Based on	F	G	H	L	M	N_p	N_{3D}
r-values	0.252	0.825	0.175	1.5	1.5	2.24	2.24
stress	0.570	0.363	0.637	1.5	1.5	2.57	2.26

The main reason for using this particularly Aluminum AA2090-T3 alloy is because of it's strong anisotropic values, which has value of $r_0 = 0.22$ while $r_{90} = 1.57$.

Concerning A6061P-T6 and SPCE steel, the corresponding properties are listed in table 4.3 and table 4.5, respectively. Hills parameter values are shown in table 4.4 and table 4.6.

Table 4.3: Material properties of AA6061-T6

AA6061-T6*				
Sheet thickness	1.0 (mm)			
Young's modulus	61 000 (MPa)			
Poisson's ratio	0.33			
Stress-strain curve	$\sigma_y(\bar{\varepsilon}^p) = 298 + 26.76(1 - e^{-20.28\bar{\varepsilon}^p})$			
R-values	r_0	r_{45}	r_{90}	
	0.524	0.599	0.710	
Yield stresses (MPa)				
σ_0	σ_{45}	σ_{90}	σ_b	τ
298	277.9	280	278.9	174.9

*Material properties from Wu et al. [28].

Table 4.4: Values of Hill'48 parameters for AA6061-T6

Based on	F	G	H	L	M	N_p	N_{3D}
r-values	0.484	0.656	0.344	1.5	1.5	1.25	1.25
stress	0.64	0.50	0.50	1.5	1.5	1.73	1.45

Table 4.5: Material properties of SPCE

SPCE*	
Sheet thickness	1.2 (mm)
Young's modulus	113 600 (MPa)
Poisson's ratio	0.30
Stress-strain curve	$\sigma_y(\bar{\varepsilon}^p) = 159.01 + 138.25(1 - e^{-17\bar{\varepsilon}^p})$
R-values	r_0 r_{45} r_{90}
	1.53 1.64 2.05
Yield stresses (MPa)	
σ_0 σ_{45} σ_{90} σ_b τ	
161.2 159.6 170.8 159.9 84.7	

*Material properties from Wu et al. [28].

Table 4.6: Hill'48 parameters for SPCE

Based on	F	G	H	L	M	N_p	N_{3D}
r-values	0.295	0.395	0.605	1.5	1.5	1.48	-
stress	0.45	0.56	0.44	1.5	1.5	1.53	1.32

4.2.2 Yield stresses and r-values evolution

Firstly, it is important to analyze how the anisotropy affects yield stress of a material with the angle relative to the rolling direction. In figure 4.1 it is shown the evolution of r-values along the rolling direction for the AA2090-T3 material used in this study.

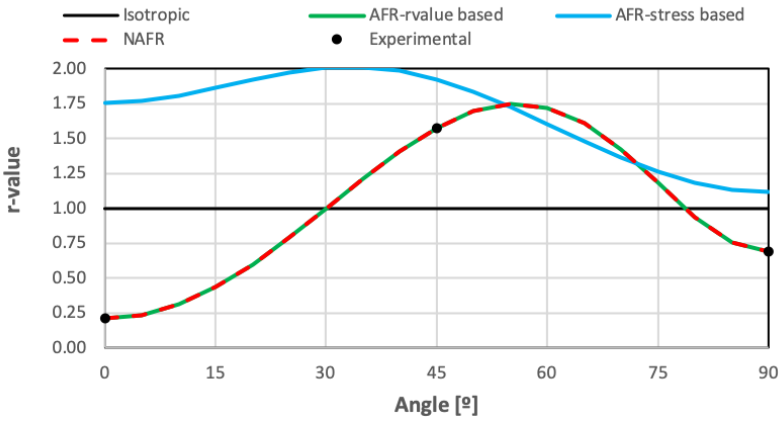


Fig. 4.1: Numerical r-value evolution with different models for AA2090

From figure 4.1 it is seen that isotropic behavior modeling is far from adequate to model the change, since isotropic behavior does not consider the changes in material properties at different directions in the material. With implemented Associated Flow Rule (AFR) based on r-values then it was possible to reproduce the same behavior from FEM output as of the experimental result. On defined constitutive equations based on yield stress components instead of the r-values then AFR (yield based) shows the different r-value trend from the experimental one.

Figure 4.2 shows evolution of yield stress with respect to angle with rolling direction of the sheet metal. At the beginning of curve at 0^0, the different models based on different parameters show the same behavior. This is due to the fact that reference stress is along the 0^0, i.e., σ_0.

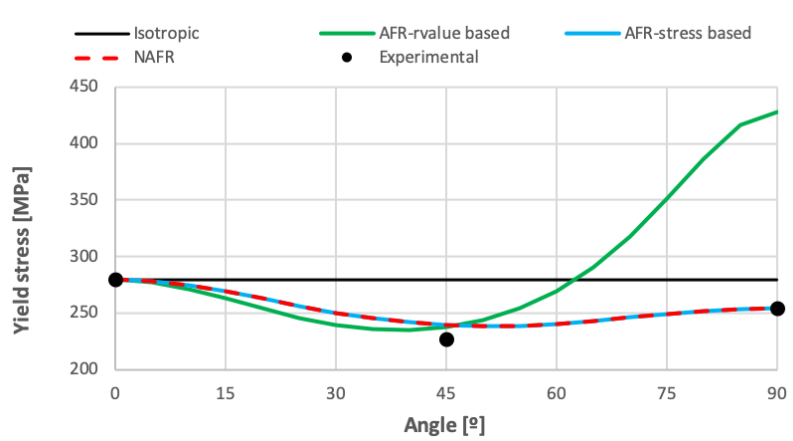


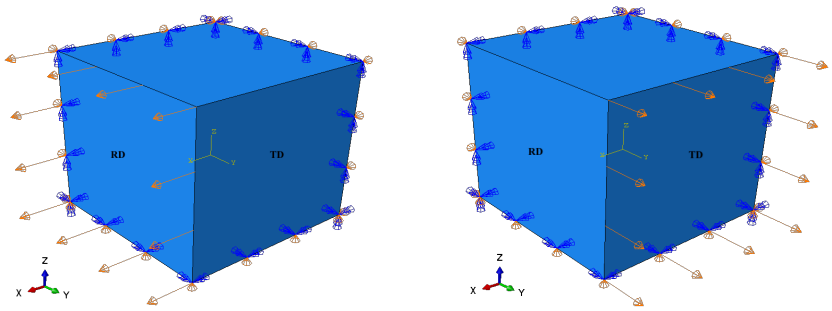
Fig. 4.2: Numerical yield stress evolution with different models for AA2090

Along the 90^0 direction yield stress predicted by the AFR based on r-values is higher than the experimental values. To implement r-value and yield stress material behavior in the FEM code it is important to consider such NAFR approach which the yield stress behavior having the flow direction considered independently.

4.3 Single element case study

To keep in mind the complexity while implementing the newly developed scrip and testing the model can be difficult. From the point of view to test the model

efficiently it is the best practice to implement the developed model firstly on single element in FEM code.



(a) Rolling Direction (RD) (b) Transverse Direction (TD)

Fig. 4.3: Boundary conditions for test model

For this study we used 3D Stress element from ABAQUS library, C3D8R: An 8-node linear brick with reduced integration.

The selected material for single element case study the hardening behavior for Aluminum alloy AA2090-T3 is defined using Swift hardening law as shown in figure 4.4.

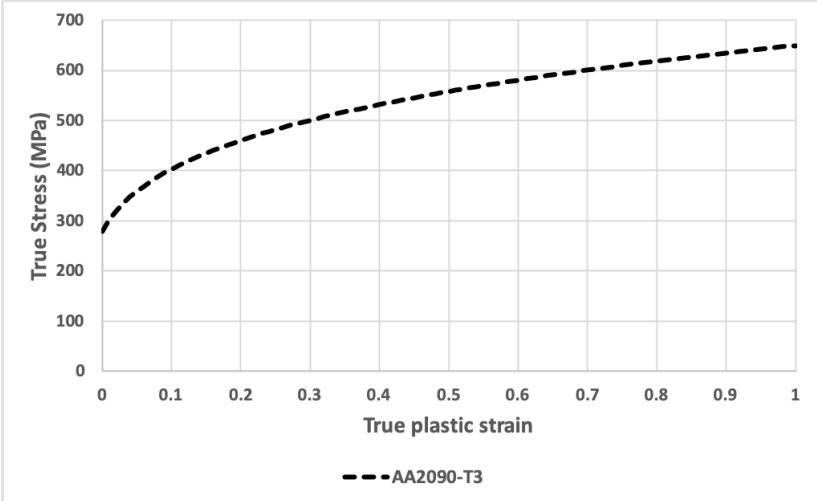


Fig. 4.4: Swift hardening behavior for AA2090-T3

Using the properties as shown in the table 4.2 the Hill'48 3D yield surface is plotted in the figure 4.5. Two simple tensile tests were carried out in rolling and transverse directions. Figure 4.3 shows, the boundary conditions used during the test of single element of 1 mm cube. For the rolling direction test along X-axis, figure 4.3 a), the boundary conditions have symmetry defined

about the three faces of the cube. The two tensile tests were carried along the rolling direction (RD) and transverse direction (TD) aligned along X and Y-axis respectively.

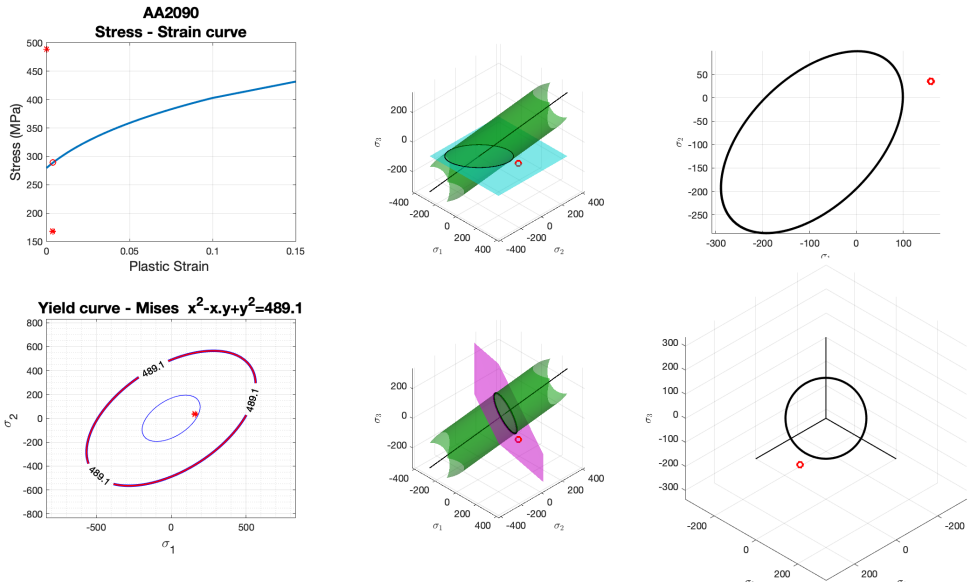


Fig. 4.5: Hill'48 3D yield surface for the AA2090

4.3.1 Single element numerical results

In this section the assessment of VUMAT is performed and results from stress-strain curves and r-values are compared between different approaches.

Figure 4.6 shows the simple tensile test along the rolling direction, which is coincident with x-axis. The Swift hardening behavior is plotted for the reference.

In figure 4.6 results obtained from implementation of Hill'48 models are presented along with the hardening behavior using Swift law. As seen, the results for different approaches are coincident, which means that input values for the hardening Swift law follow the obtained results for AFR(r-based), AFR(yield-based) and NAFR.

The two approaches of the Hill'48 based on r-value and Hill'48 based on yield surface, since they are both AFR, give the same result for the rolling direction. That is explained by σ_{11} being used as the reference stress.

The figure 4.7 shows similar results to figure 4.6, but now along the 90 degrees

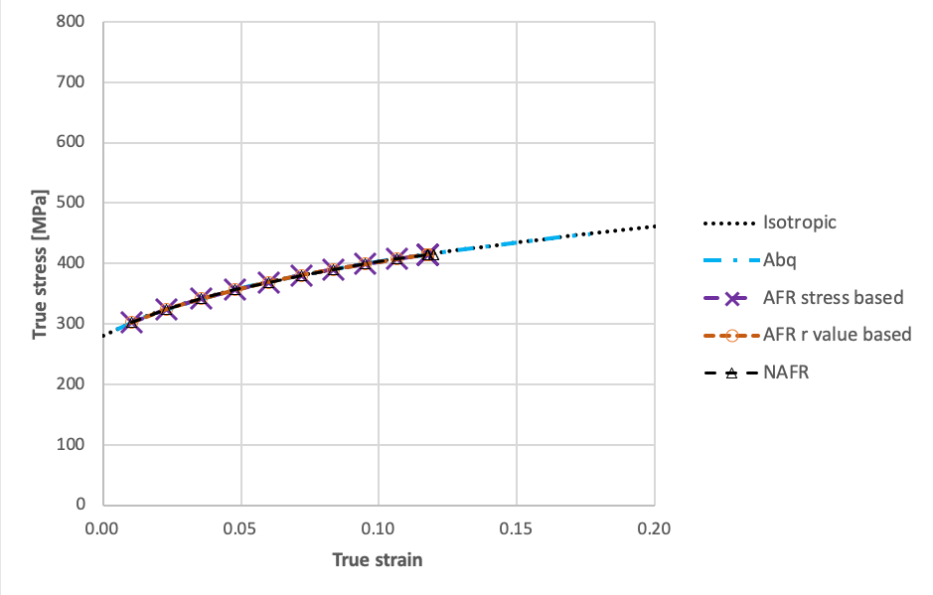


Fig. 4.6: True stress-strain along rolling direction

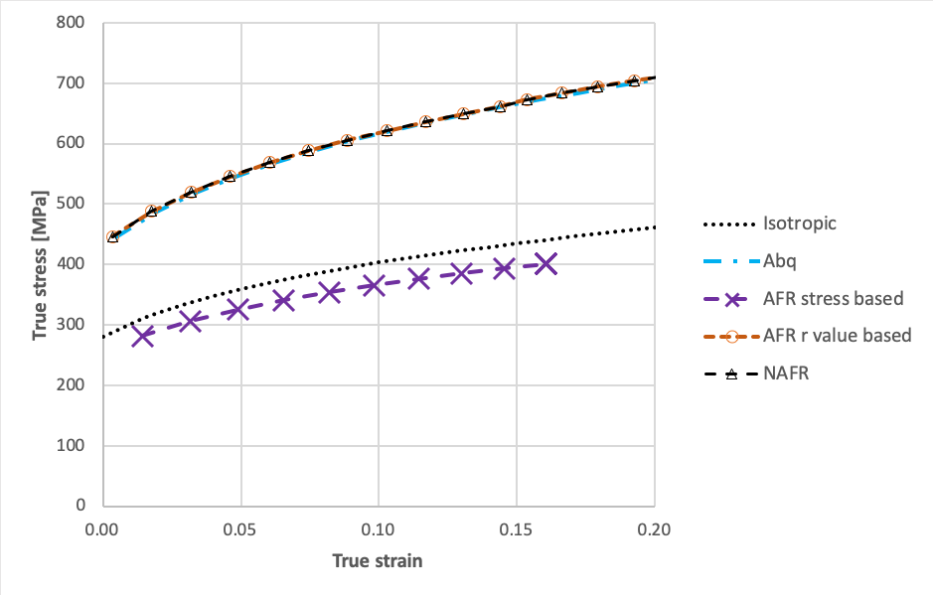


Fig. 4.7: True stress-strain along longitudinal direction

to rolling direction. In figure 4.7 it can be seen that the isotropic behavior is coincident with the Swift hardening behavior as expected. The two AFR approaches (r-based and stress-based) predict different stress behavior. The results for AFR r-based and NAFR are predicting similar results, which is the same behavior as seen previously in figure 4.2.

Table 4.7: Numerical results: r-value comparison

Angle	**0^0**	**90^0**
Exp.	0.21	0.69
Isotropic	1.0	1.0
AFR r-based	0.22	0.69
AFR stress-based	1.73	1.11
NAFR	0.22	0.69

Table 4.7 shows the experimental and numerical measured r-values. The numerical simulation were performed for the rolling (along the x-axis) and longitudinal (along the y-axis).

From figure 4.1 it can seen that when the potential (flow function) is based on the r-values, therefore numerical simulation predicts the same r-values as the experimental measured values. The Hill'48 numerical model based on yield stresses predicts different r-values. The NAFR predicts similar r-values as the experimental results.

From the analysis of figure 4.1, 4.2 and table 4.1 it can be seen that, since AFR is based on either r-values or yield stress components, corresponding results only guarantee a correct material behavior for either results of strain or results of stress, not both, simultaneously. On the other hand, NAFR can follow material behavior for strains and stresses simultaneously.

That is why implementation of yield and potential (flow) behavior simultaneously is important. This can be achieved by using NAFR and from the previous case study it is seen that NAFR based constitutive models consider both the yield stresses and r-values anisotropy.

4.4 Cylindrical cup test

The earing prediction of a cylindrical cup-drawing test is a widely used indicator to represent the accuracy of a yield criterion. For this study, a cup drawing test was carried out using a cylindrical punch of 97.46 mm diameter for AA2090 and 75 mm for AA6061 and SPCE material. An AA2090-T3 aluminum alloy sheet of 1.6 mm thickness was used in this work. While for the AA6061 was 1 mm and for SPCE was 1.2 mm. The tools setup for the simulation is shown in the figure 4.10. A schematic view of the cup drawing process is shown in figure 4.8 with its dimensions in the table 4.8 and table 4.9. The cylindrical cup drawing test is one that can best characterize a typical forming operation, since it embodies the combined effects of friction, blank-holder force, bending and unbending of a sheet.

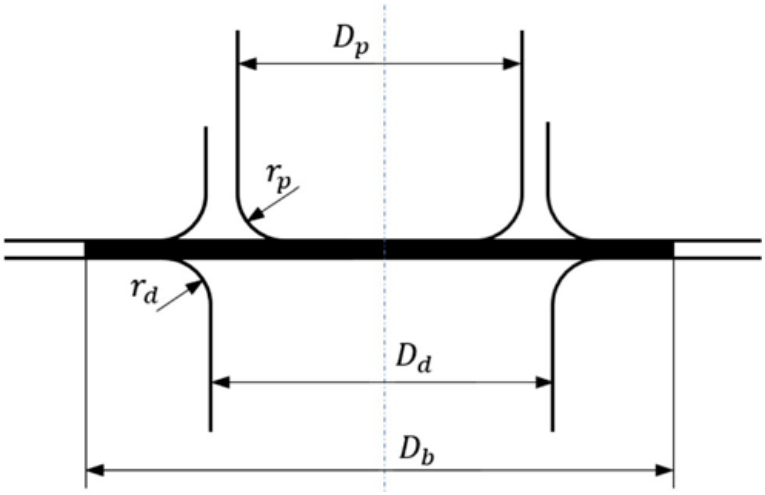


Fig. 4.8: Schematic view of the cylindrical cup-drawing test

The geometry and the specimen dimensions in the table 4.8 of the cylindrical cup-drawing test have been taken from Yoon at el. [65] and Park and Chung [66].

Table 4.8: Dimensions of tools for cup drawing (mm): AA2090

Material	D_b	D_d	D_p	r_d	r_p
AA2090-T3	158.76	102.48	97.46	12.70	12.70

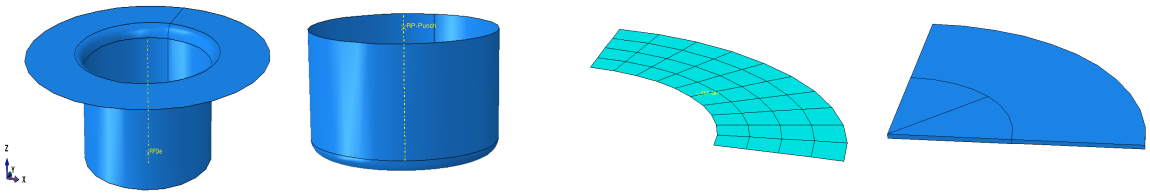
Table 4.9: Dimensions of tools for cup drawing (mm): AA6061 and SPCE

Material	D_b	D_d	D_p	r_d	r_p
AA6061 and SPCE	135	79	75	5	5

In case of material AA2090, the cup was formed with a minimum blank-holder force of 22.2 kN (approximately 1% of the yield force) to prevent wrinkling (divided by 4 for a quarter model) as suggested in the [28,39]. In case of material AA6061 and SPCE the blank holder was fixed at a distance of 1.15mm and 1.4 mm respectively. Coulomb friction coefficient of 0.05 has been used between the blank and the tools throughout the different numerical simulations.

4.4.1 Finite element models

The punch and die were modeled as rigid bodies and analytical surfaces, while blank holder was discretized with rigid planar shell element. A solid element formulation with reduced integration mode was used to model the blank. To reduce the computational time and to take the advantage of symmetrical cup geometry only one quarter model was simulated and symmetry boundary conditions (BC) have been imposed. Typical parts defined and assembled for the FE simulations are shown in figure 4.9 and 4.10.



Die Punch Blank Holder Blank

Fig. 4.9: Typical parts in the FE model: Die, Punch, Blank Holder and Blank

All cup drawing processes were simulated in the explicit time integration scheme, so that a VUMAT (user-defined material for Abaqus/Explicit) was needed for the material models.

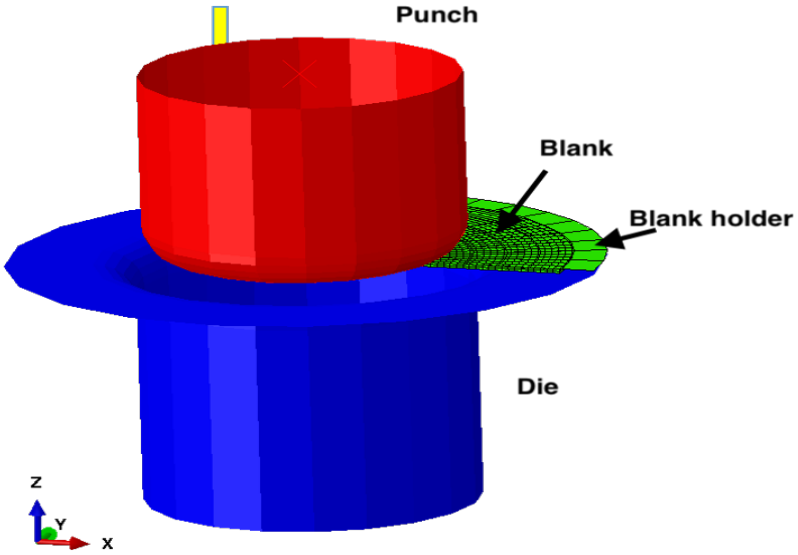
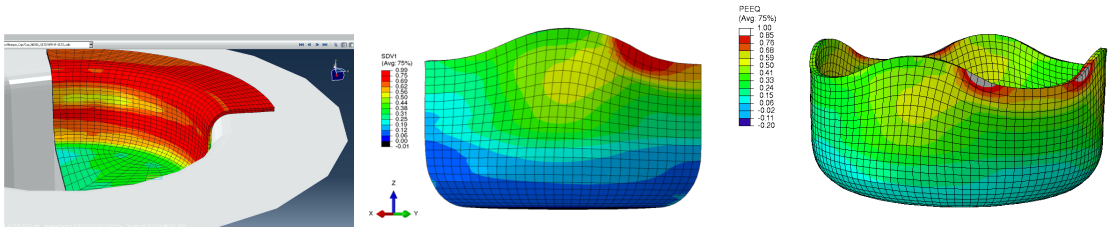


Fig. 4.10: Numerical tool assembly for the cylindrical cup drawing

Table 4.10: Simulation boundary conditions (BC)

Tool	**AA2090**	**AA6061 and SPCE**
Die	Fixed	Fixed
Punch	Disp. Z-axis	Disp. Z-axis
Blank Holder	F=5.55 kN	1.15 mm and 1.4 mm
Friction	0.05	0.05



(a) (b) (c)

Fig. 4.11: Different stages of cylindrical cup drawing

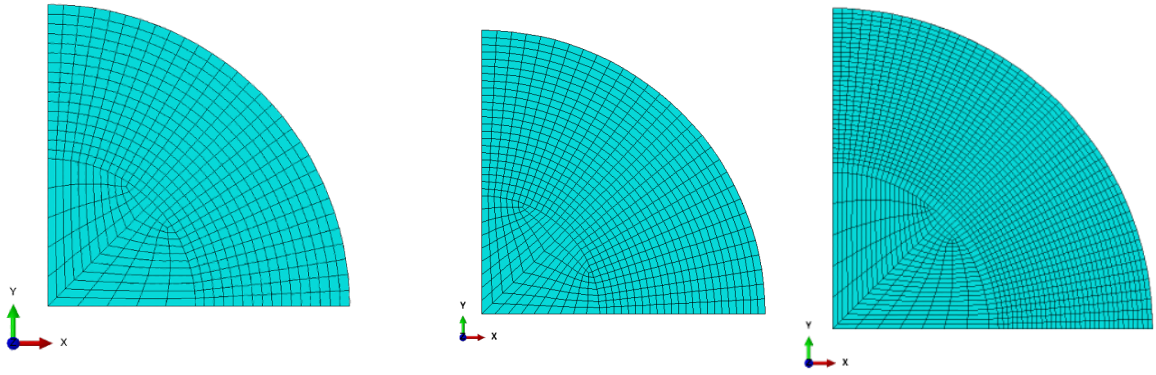
Typical deep drawing and earing formation of a cylindrical cup at different stages of the simulation with equivalent plastic strain is shown in the figure 4.11. This example is for the case of AA2090 alloy simulated with AFR r-based model. In total, 24 simulations were performed to get the earing profiles (cup height after drawing) of three different cases using three different material models and various different mesh models. Results obtained by pure isotropic hardening

are also presented during the cup height comparisons.

The earing predictions using two different anisotropic models based on Hill'48 are implemented for the three materials i.e. AA2090, AA6061 and SPCE. One important aspect of the advanced material models developed for more effective simulations of sheet metal forming is computation time. For this study all the numerical simulations were performed under the same conditions with the same machine with 4 CPUs (Quad-Core Intel Core i7) and 8 GB of RAM memory working on a Linux platform.

4.4.2 Mesh sensitivity analysis

To evaluate the mesh sensitivity of the earing simulations various different mesh systems were considered to model the blank. In figure 4.12 several blank discretizations are presented. Mesh1 is a coarser mesh consisting of 30 elements along the perimeter and 16 elements along the radial direction at cup wall, also with two elements in thickness direction. Mesh2, which is a finer mesh than mesh1 consists of 30 elements along the perimeter and 12 elements along the radial direction at cup wall and 3 elements along the thickness. Whereas, Mesh3 is the finest mesh consisting of 50 elements along the perimeter and 32 elements along the radial direction at cup wall and having three elements along the thickness direction.



Mesh1 Mesh2 Mesh3

Fig. 4.12: Example of different meshes used for the cylindrical cup test

So, to analyze mesh sensitivity for cylindrical cup results, there were several proposed mesh combinations, which were used to perform simulations. Mainly

focusing on analyzing after the mesh is:

- refined along Perimeter of blank
- refined along Radius of blank
- refined along Thickness of blank

Table 4.11: Different mesh models

AA2090	**AA6061**	**SPCE**
P30R16T2	P30R16T2	P30R16T2
P30R16T3	P30R16T3	P30R16T3
	P30R16T4	P50R16T2
	P30R32T2	P50R16T3
	P30R32T3	P30R32T2
	P30R32T4	P30R32T3
	P50R16T2	
	P50R16T3	
	P50R32T2	
	P50R32T3	
	P30R48T2	
	P30R48T3	

P-Perimeter, R-Radius, T-Thickness

For current analysis and study, the 3D element with eight-node type C3D8R is used.

4.4.2.1 Results

For this study the earing result predicted by AFR r-based model and AFR stress-based models are shown in the figure 4.14. Using the two different mesh as shown in the figure 4.13, the cup height prediction shows no visible differences. This means that both meshes sufficiently discretize the blank on critical area such as at the die radius. Hence the two types of results are showing no effect of such mesh models.

However there is significant improvement is computational time from 164 minutes to 57 minutes due to reduced number of elements in the mesh with 2 elements in thickness direction (T: 2 Elements).

A similar procedure to test mesh sensitivity is performed to AA6061 material, since it has smaller punch radius and blank diameter which makes it more sensitive to the mesh/element size of the blank.

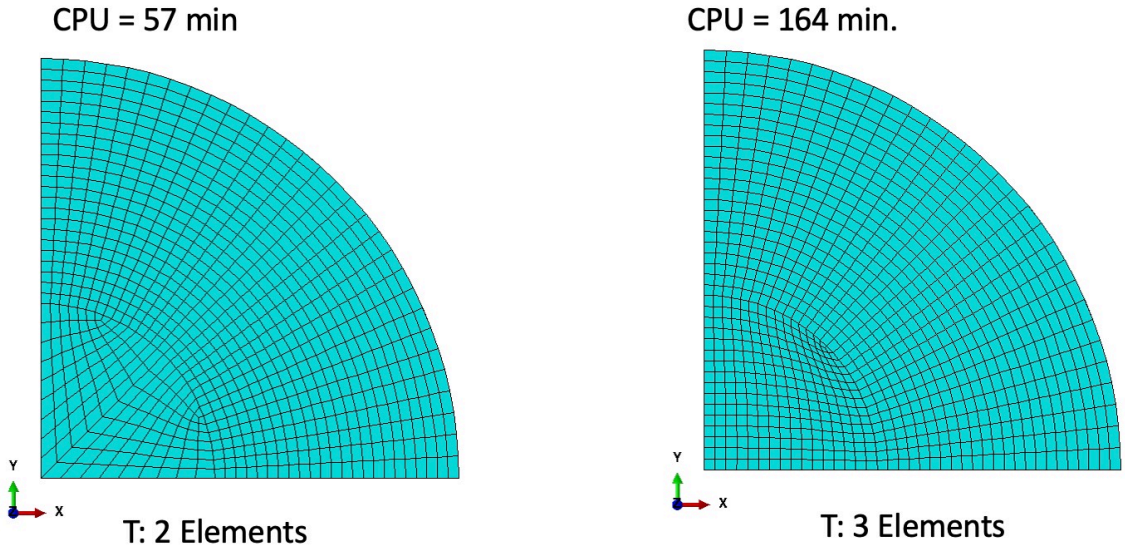


Fig. 4.13: Two mesh models for the AA2090 material

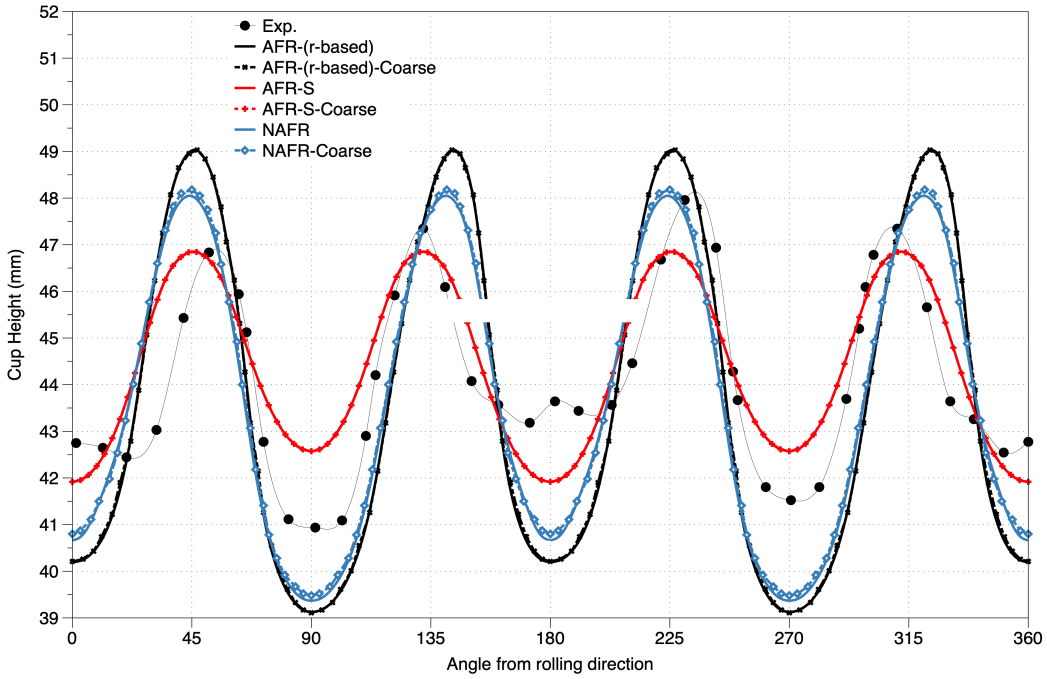


Fig. 4.14: Cup height comparison of AA2090 different mesh

In figure 4.15 shows the similar comparison of the predicted cup heights using two different mesh. Unlike, AA2090, the cup height prediction gets difference for

the two mesh models. To understand and quantify how the mesh discretization is affecting the results we will analyze different mesh models to predict the cup height.

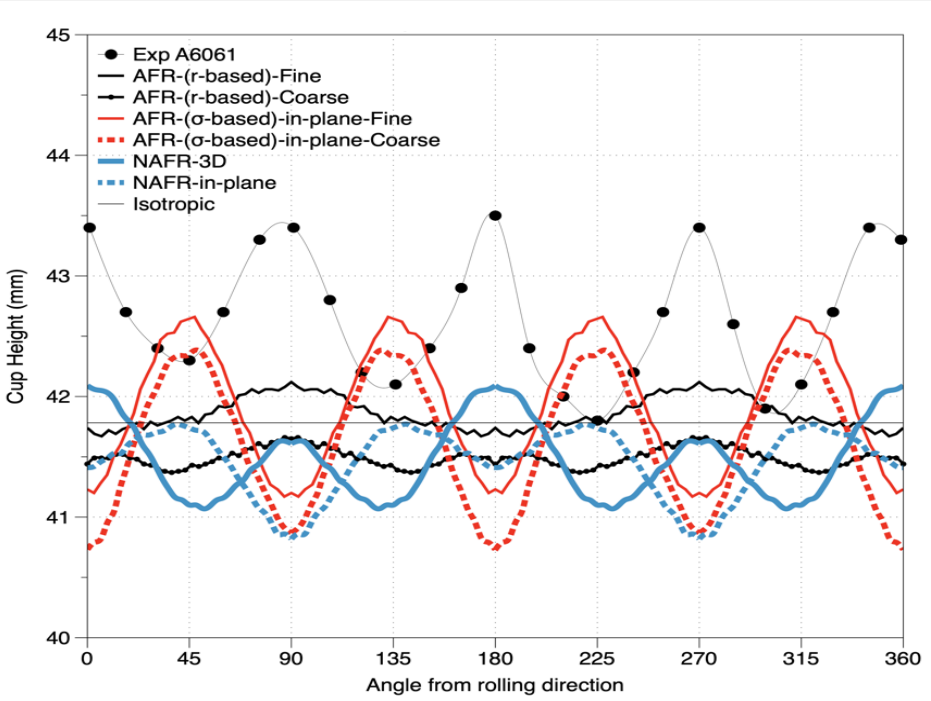
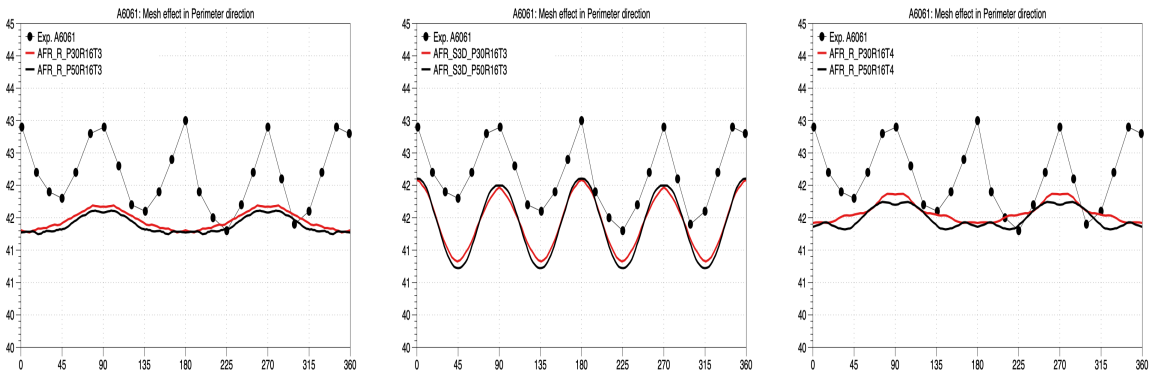


Fig. 4.15: Cup height comparison of AA6061 different mesh

Figure 4.15 shows the comparison of the predicted cup heights using two different methods.

Effect of Different Mesh in Perimeter

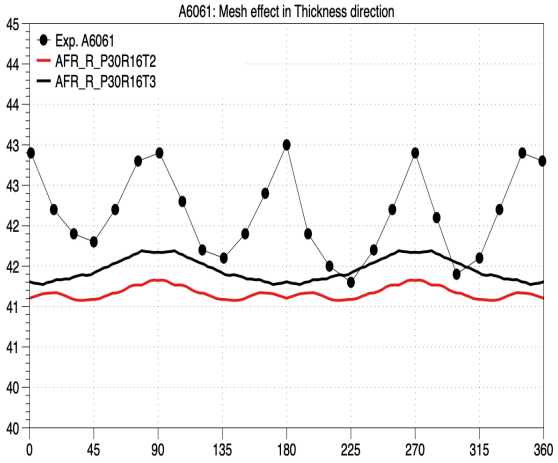
From the figure 4.16 the results of different models shows that the mesh refinement along the perimeter shows no difference in cup height prediction.



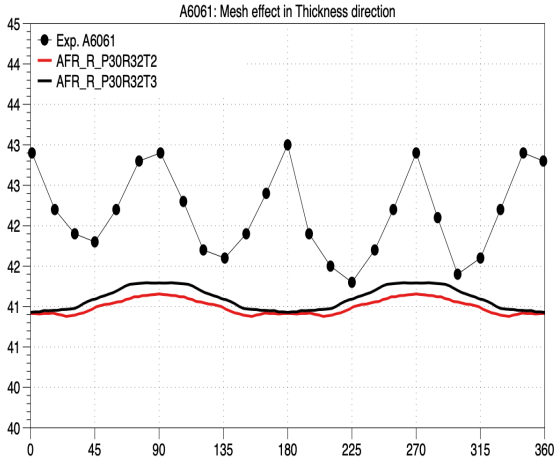
Mesh1: r-based Mesh1: σ-based Mesh2: r-based

Fig. 4.16: Effect of Different Mesh along Perimeter

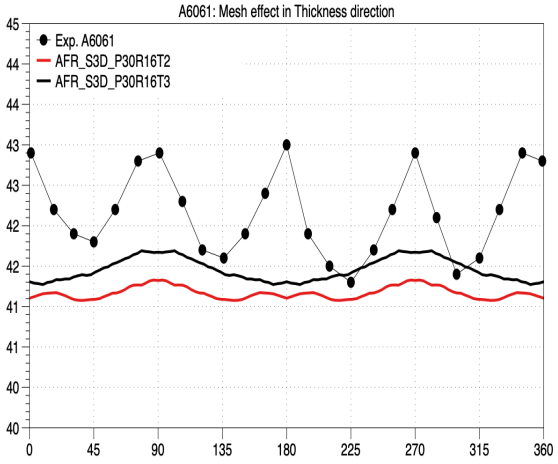
Effect of Different Mesh in Thickness



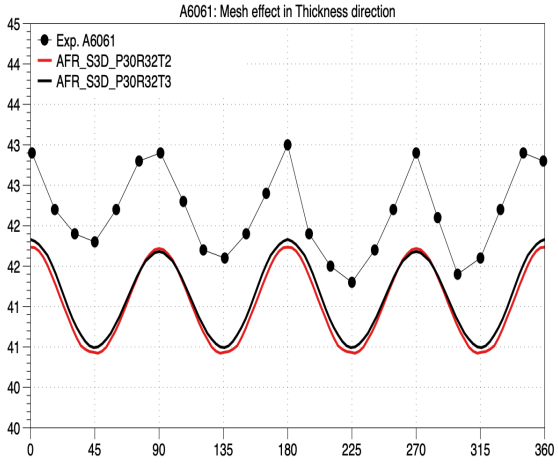
(a) AFR-r: Mesh1



(b) AFR-r: Mesh 2



(c) AFR-σ : Mesh 1

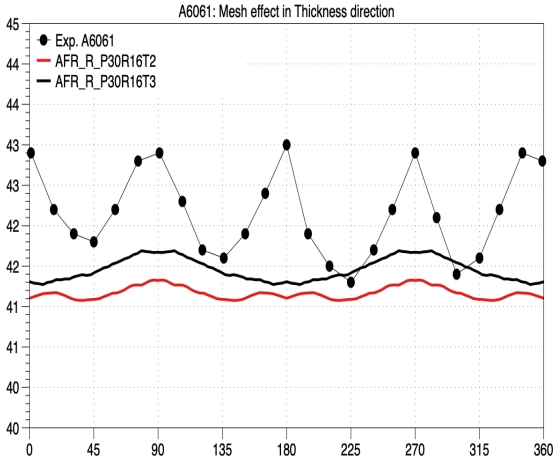


(d) AFR-σ : Mesh 2

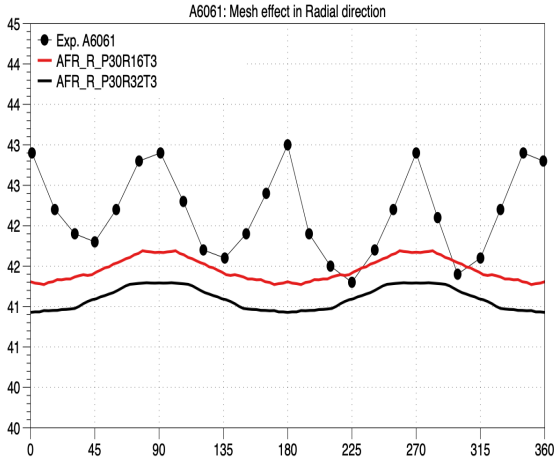
Fig. 4.17: Effect of Different Mesh in Thickness

From figure 4.16, results of different models shows that mesh refinement along the thickness direction shows some differences in cup height prediction. Hence, it is important to have sufficient number of elements along the blank thickness.

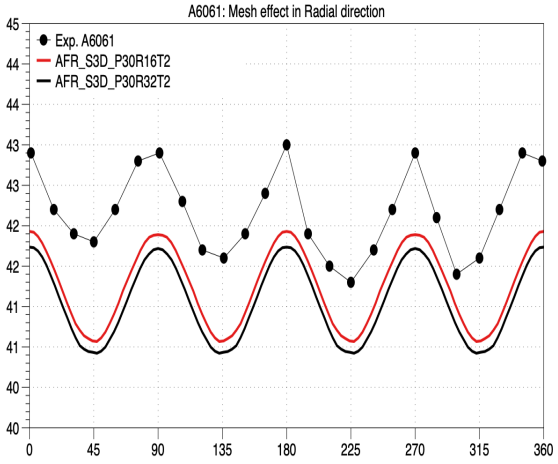
Effect of Different Mesh in Radial direction



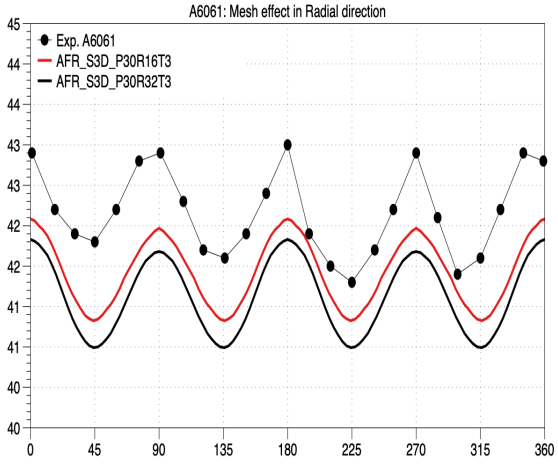
(a) AFR-r: Mesh1



(b) AFR-r: Mesh 2



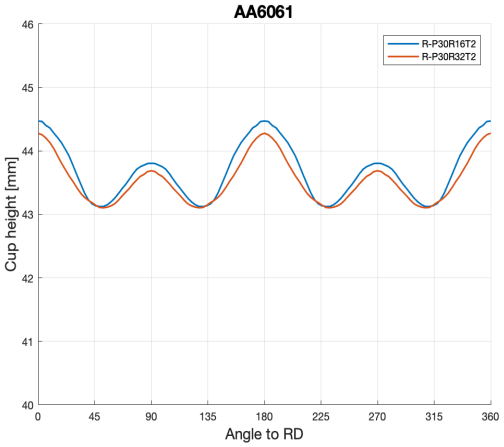
(c) AFR-σ : Mesh 1



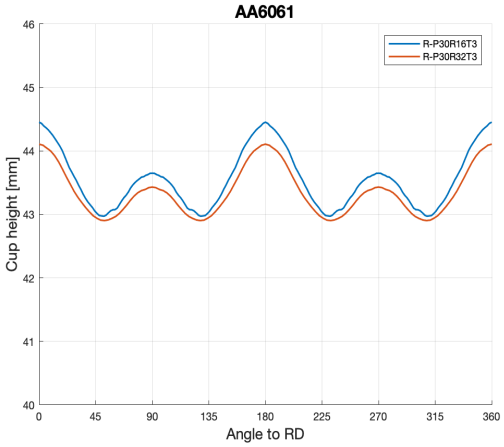
(d) AFR-σ : Mesh 2

Fig. 4.18: Effect of Different Mesh in Radial direction

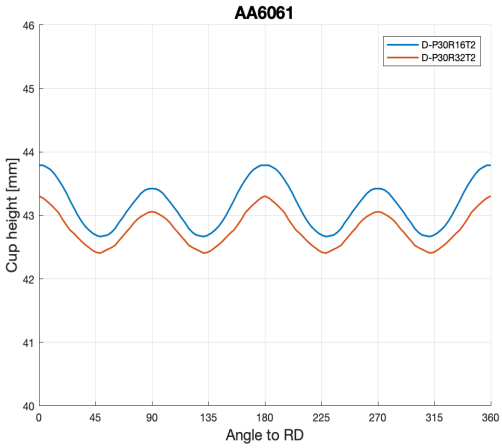
From the figure 4.18 the results of different models show that the mesh refinement along the radial shows also that this refinement has influence and there is a decrease in cup height prediction.



(a) AFR-r: Mesh1



(b) AFR-r: Mesh 2



(c) AFR-σ : Mesh 1

Fig. 4.19: Effect of Different Mesh in Radial direction for SPCE

In case of SPCE steel material, from the figure 4.19 the results of different models show that the mesh refinement along the radial direction have the effect of decreasing in cup height prediction.

The anisotropic plastic flow in the material creates the drawing ears in the final component. Therefore the cup drawing test was analyzed taking into account two main factors, as follows:

- Accuracy of the predicted ear profile
- Equivalent plastic strain distribution

The simulations were based on three models, two AFR models (r-based and stress-based) and a non-AFR model.

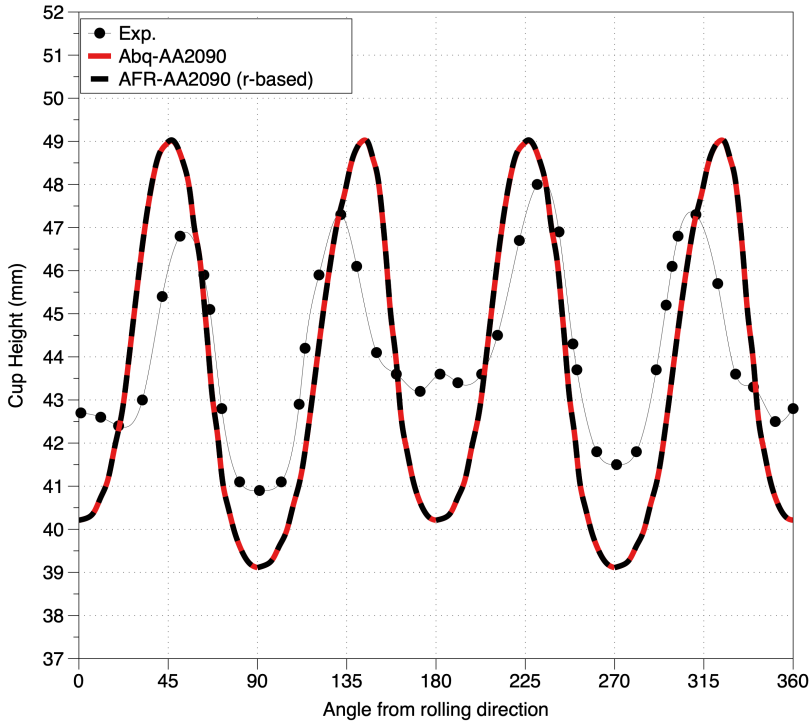


Fig. 4.20: Validation of VUMAT with Abaqus code results (without user subroutine)

From the figure 4.20 it can be seen that the developed VUMAT user subroutine presents the same results as the closed box Abaqus code, which validates the current implementation. further validation of the developed AFR, NAFR models, the results published in bibliography by Wu at el. [28] will be followed.

4.4.3 NAFR vs. AFR results using different methodologies

As shown in the 2.1 the stress based parameter N can be calculated by two ways. First is in-plane and second is 3D formulation. As this one parameter can also influence the AFR stress based results hence similarly NAFR might also gets influenced. To quantify the effect of such Hill'48 parameter N, the comparison between cup height, ear prediction is made using three methods of the VUMAT models developed.

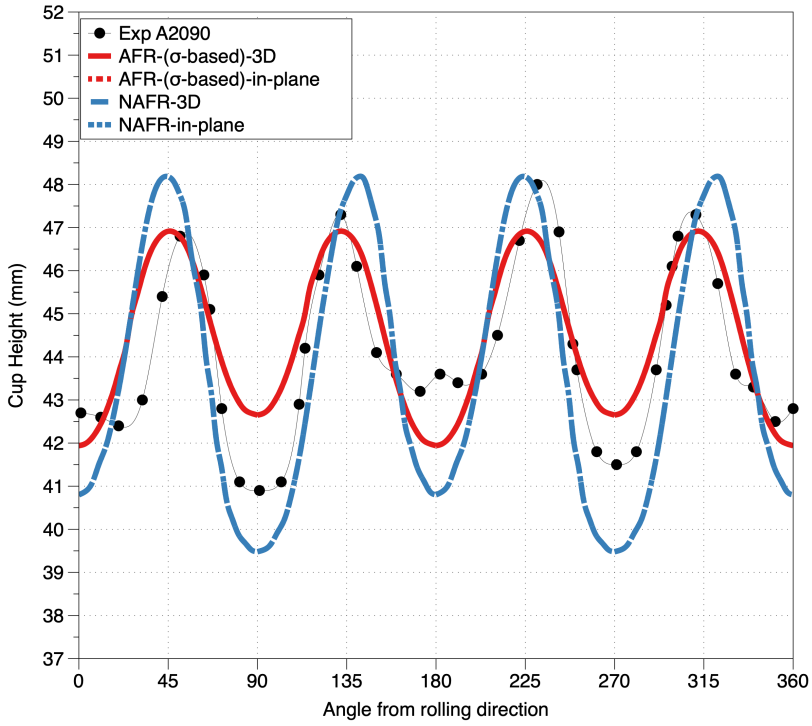


Fig. 4.21: In-plane vs 3D formulation of Hill48 function

From the figure 4.21 it can be seen that the in-plane and 3D formulation is giving the same cup height and ear prediction.

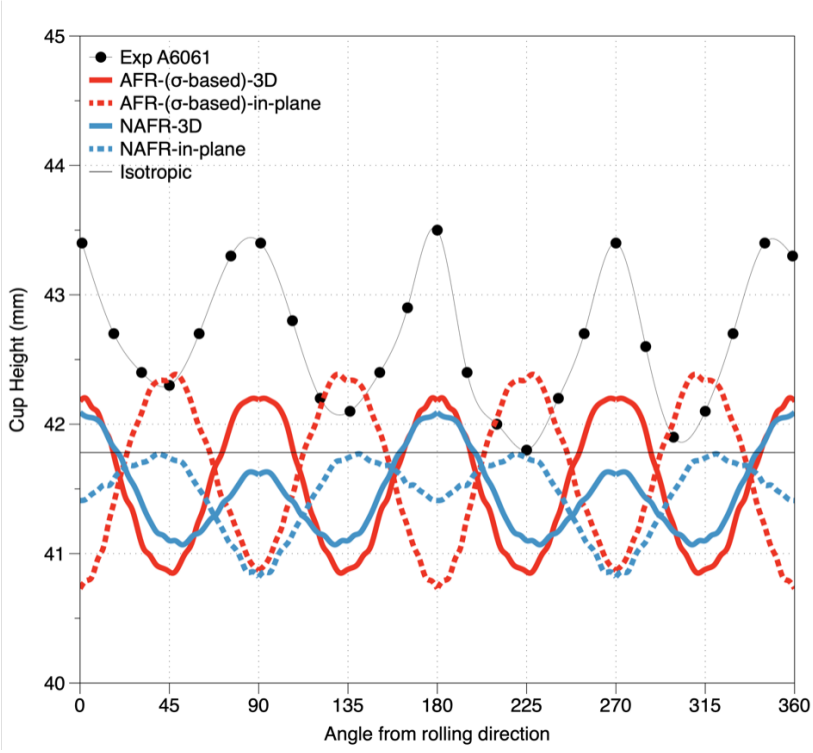


Fig. 4.22: In-plane vs 3D formulation of Hill'48 function for AA6061

From the figure 4.22 it can be seen that the in-plane and 3D formulation does not give similar results. Hence, the AFR stress based and NAFR methods can be seen influenced by the N parameter of Hill'48. It can also be seen that the in-plane formulation predicts the opposite evolution of peaks and valleys for the cup height earing. The 3D formulation for the same model gives similar profile of cup earing as the one of experimental data.

For the material AA6061 the equivalent plastic strain distribution contours can be seen in figure 4.23 for the various approaches that are discussed.

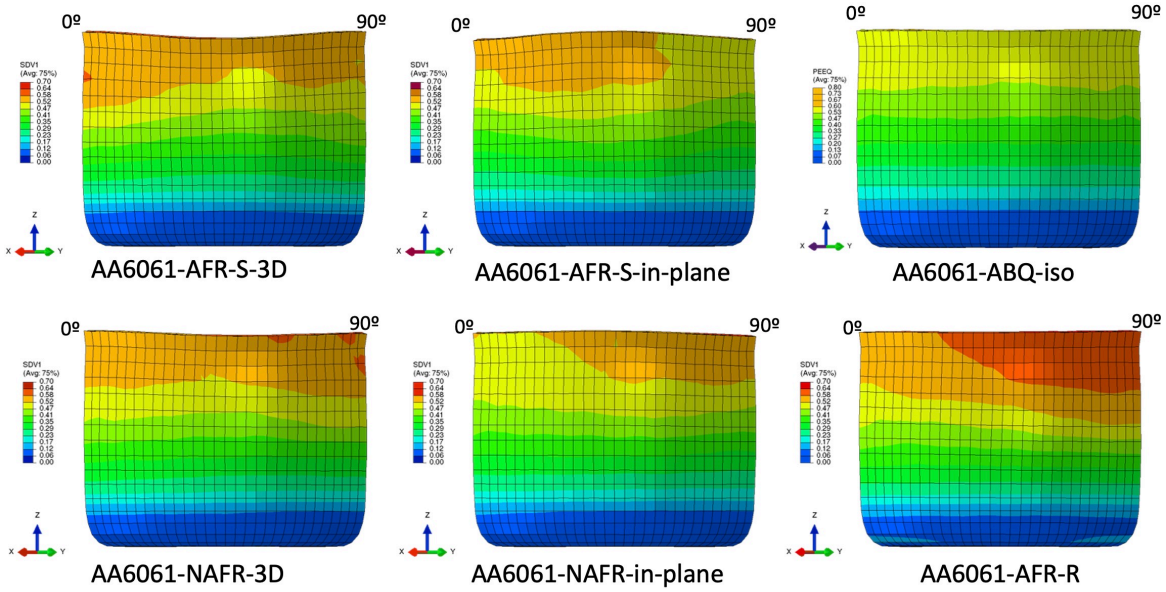


Fig. 4.23: Contours of the equivalent plastic strain for different approaches and AA6061

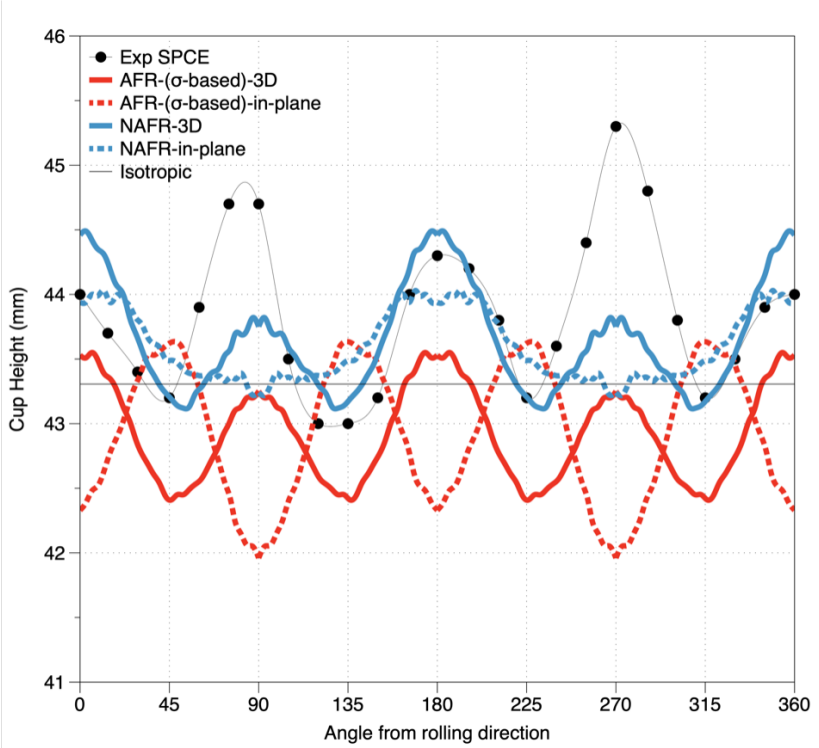


Fig. 4.24: in-plane vs 3D formulation of Hill48 function for SPCE steel

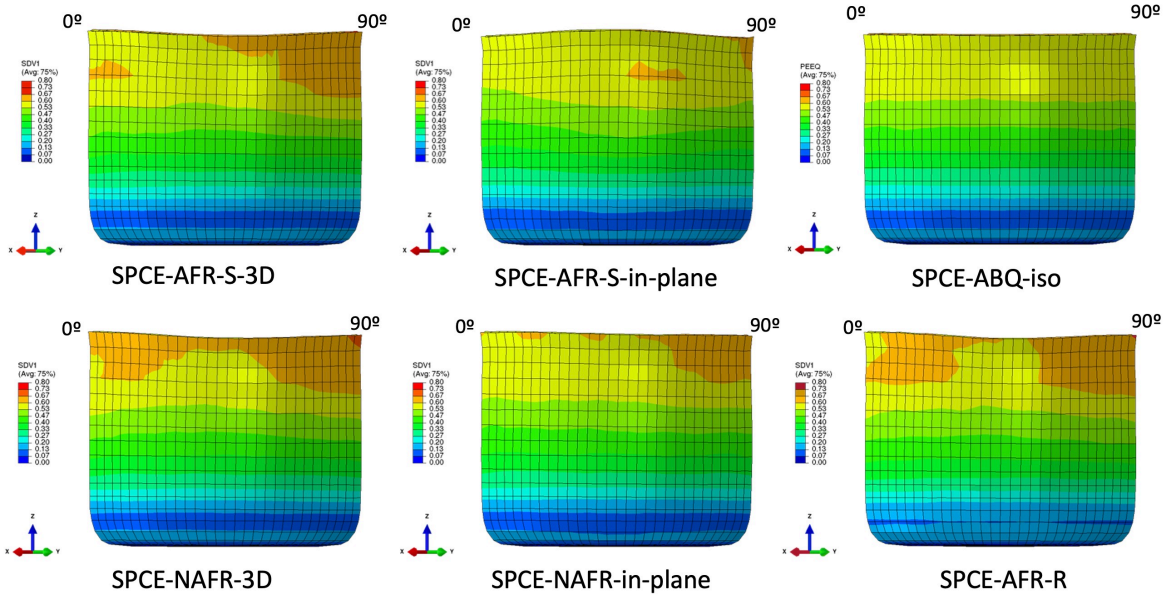


Fig. 4.25: Contours of the equivalent plastic strain for different approaches and SPCE steel

As it can be observed throughout the results that the NAFR predicts cup height and earing more closely to the experimental measurements in trend and accuracy. The earing profile predicted by NAFR model is in good agreement with the

experimental values. Regarding the mesh sensitivity, the results obtained by using Mesh2 and Mesh3 are very similar for both material models while the results obtained with Mesh1 are slightly different from the others. In fact the simulations performed with the finer mesh (Mesh2 and Mesh3) predict the earing slightly better than those performed with the coarser mesh system (Mesh1).

For comparison, the earing profiles (cup height) were simulated using different material models: Isotropic, Hill'48- $f(\sigma)$, Hill'48-$g(\sigma)$ and with the NAFR. The experimental and simulated earing profiles are compared. The Hill'48-$f(\sigma)$ model underestimates the experimentally determined amplitude of the earing profile, while the Hill'48-$g(\sigma)$ model overestimates the cup heights. The two models based on the AFR have different outcomes, but both gives somewhat deviation in predicting the earing profiles accurately. The simulation by using the developed NAFR model shows more close prediction of the earing profiles with the experimental cup height amplitude. This is because the NAFR model considers both aspects of anisotropy, while only one aspect can be considered in the AFR model. The developed model can also describe the behavior in an isotropic condition successfully. From the comparison between the Hill'48-f(σ) and Hill'48-g(σ) models, it can be found that for AA2090-T3 sheet, the anisotropy in deformation is much more pronounced than the anisotropy in yield stress.

In figure 4.26 it can be seen that the 3D formulation consideration gives better profile matching to the experimental measurement of the earing. Among the three different approaches of yield formulation i.e. AFR-r, AFR- or NAFR, the NAFR gives the closest results to the experimental measurement.

As we can conclude from the figure 4.26 NAFR gives the better results compared to other two AFR methods. Even though the earing prediction doesn't seem to be exactly as the experimental results. There can be many different variables affecting this, such as, accuracy of the experimental measurement, numerical forming conditions, etc. To understand this difference, it is needed to investigate the sensitivity of such variables which affects the numerical prediction. Hence, in the next subsection the sensitivity analysis for the anisotropic parameters, forming parameters is done.

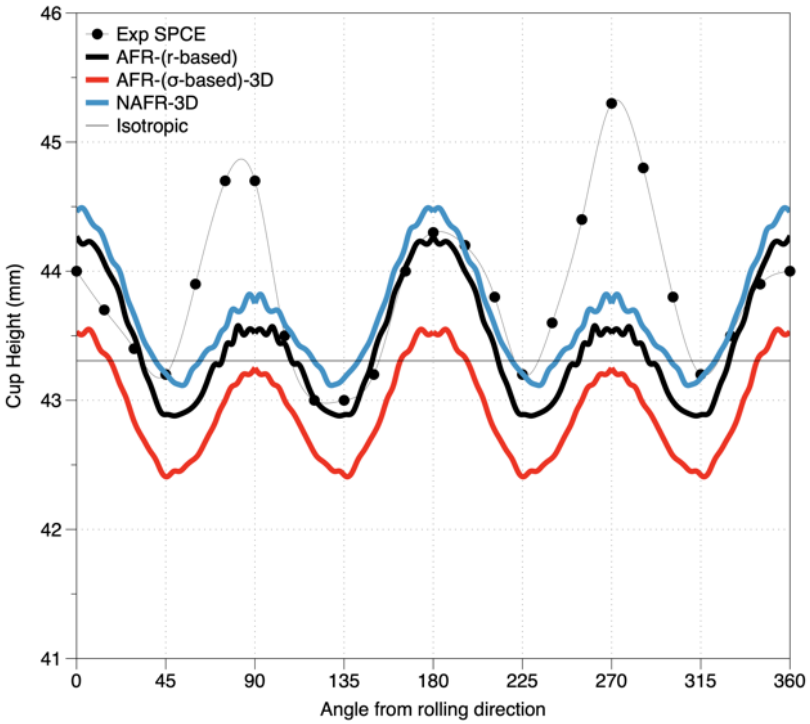


Fig. 4.26: Cup height using 3D formulation SPCE

4.4.4 Sensitivity analysis for process variables and anisotropic parameters

4.4.4.1 Friction

To evaluate the effect of friction between tools and blank it on the prediction of cup height, the different results obtained using friction with values of 0.05, 0.08, 0.13 and 0.16. The predicted cup height using these values are shown in the figure 4.27.

It can be seen that the increase in the value of coefficient of friction also increases the cup height. It is important to note that the effect is uniform i.e. translation of cup height equally for different angles to the rolling direction. Hence, friction has a linear effect in the prediction of cup height.

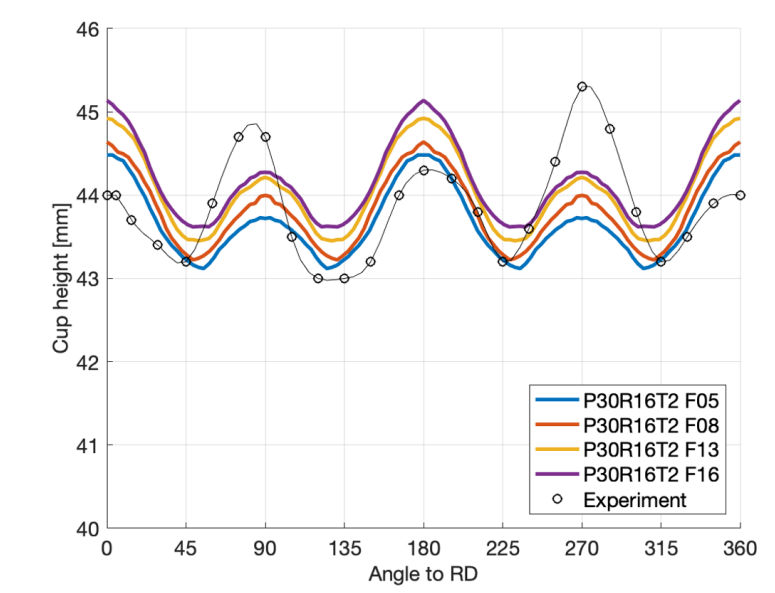


Fig. 4.27: Effect of friction on cup height prediction: SPCE

4.4.4.2 Blank holder clearance

In figure 4.28, the effect of the clearance between blank holder and blank is studied. The different clearance values of 1.3, 1.4 and 1.5 mm were used. These values are slightly greater than the blank thickness of 1.2 mm. As it can be seen, the lower is the blank clearance then the cup height prediction is higher. This is

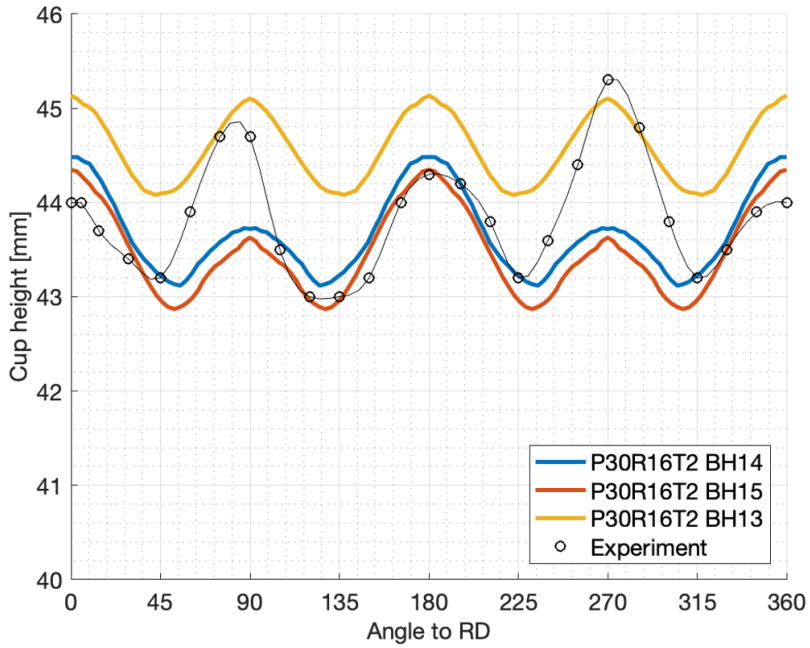


Fig. 4.28: Effect of blank holder clearance on cup height prediction: SPCE

due to material stretching between blank holder and die as the gap is closing between the two parts of the tool. Accordingly, it is important to keep the optimal clearance between the blank holder and the die. When using higher clearance, besides leading to predicting lower cup height it may also create the undesirable effect of wrinkling.

4.4.4.3 Anisotropic parameters

The table 4.12 shows the different proposed values of anisotropic values for the sensitivity analysis. Six different cases from a1 to a6 using different combination of r-values were considered. The case a1 corresponds the actual experimental values from the bibliography. Hence, the effect of anisotropic parameters r_0,r_{45} and r_{90} are compared on the cup height and earing prediction.

Table 4.12: Parameters for anisotropy sensitivity for SPCE

Case	r_0	r_{45}	r_{90}	F	G	H	N
a1	1.53	1.64	2.05	0.295	0.395	0.605	1.477
a2	2.05	1.64	1.53	0.439	0.328	0.672	1.642
a3	1.53	1.9	2.05	0.295	0.395	0.605	1.657
a4	2.3	1.8	1.6	0.436	0.303	0.697	1.699
a5	2.05	1.42	1.53	0.439	0.328	0.672	1.473
a6	2.25	1.64	1.73	0.400	0.308	0.692	1.515

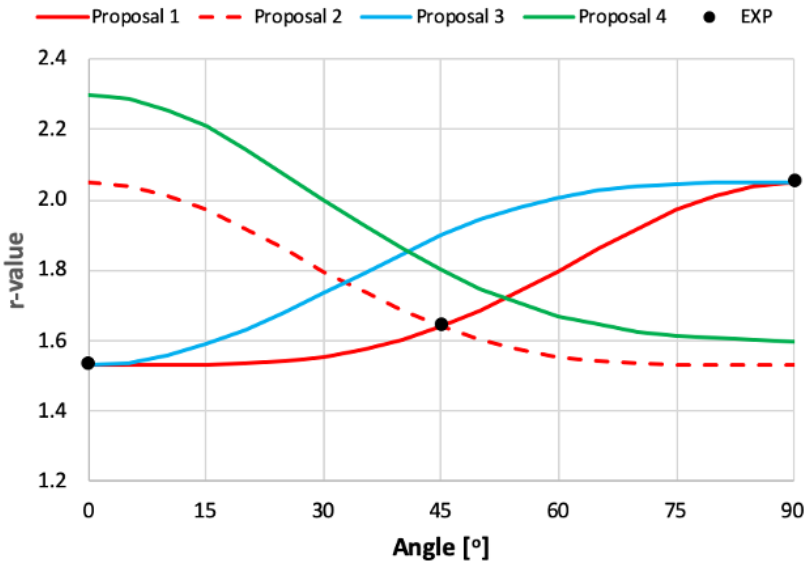
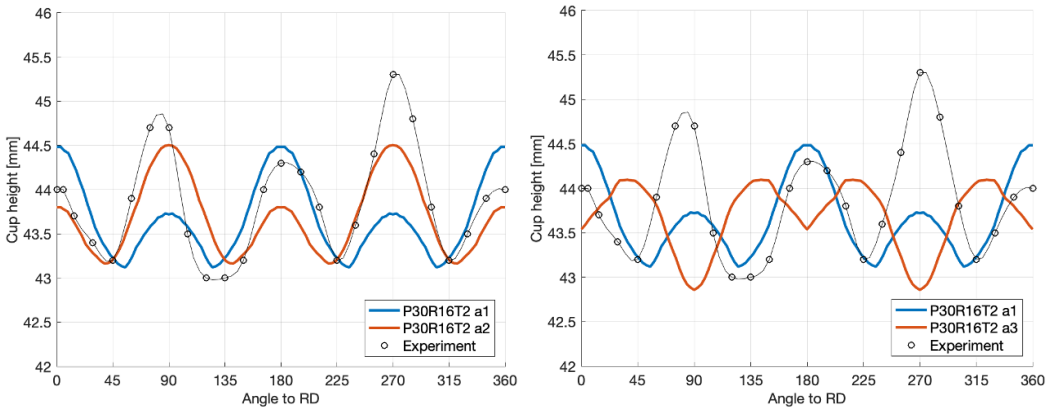


Fig. 4.29: r-value evolution for different r-values: SPCE

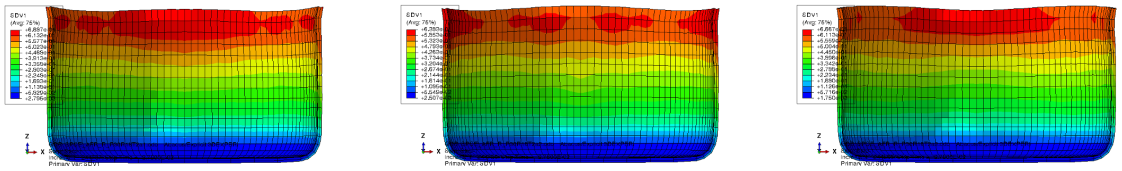
The figure 4.29 shows the evolution of the different cases of r-values using numerical formulation. It can be seen that the different case (set) of r-values gives different strains along the rolling direction. Hence, to understand the overall effect of such parameter variation different simulations are performed using these six cases.



(a) Case a1 and a2 (b) Case a1 and a3

Fig. 4.30: Cup height prediction for different r-value: SPCE

The figure 4.30 shows the cup height and ear prediction using three different sets of r-values. The case a2 is simply the reverse case of a1. That is r_0 and r_{90} values are interchanged. It is very clear from the graph a) that the a2 case gives better results close to the experimental earing. This raises a question about the accuracy the bibliographic experimental data for the anisotropic r-values. In figure 4.30 b) it is seen that the effect of r_{45} in case a3 is causing to give opposite earing than the experimental values. Such effect also seen while considering in-plane formulation.



a) Case1 b) Case2 σ-based c) Case3

Fig. 4.31: Effect of different r-values for prediction of earing

The figure 4.31 shows the contours of equivalent plastic strain obtained using different cases of r-values. Here it can be seen that even the small change in r-

values can change the earing prediction considerably. Hence, it is very important to model the numerical simulation correctly and considering the accuracy of the experimental measurement for anisotropic values. As seen r_{45} can cause opposite earing prediction.

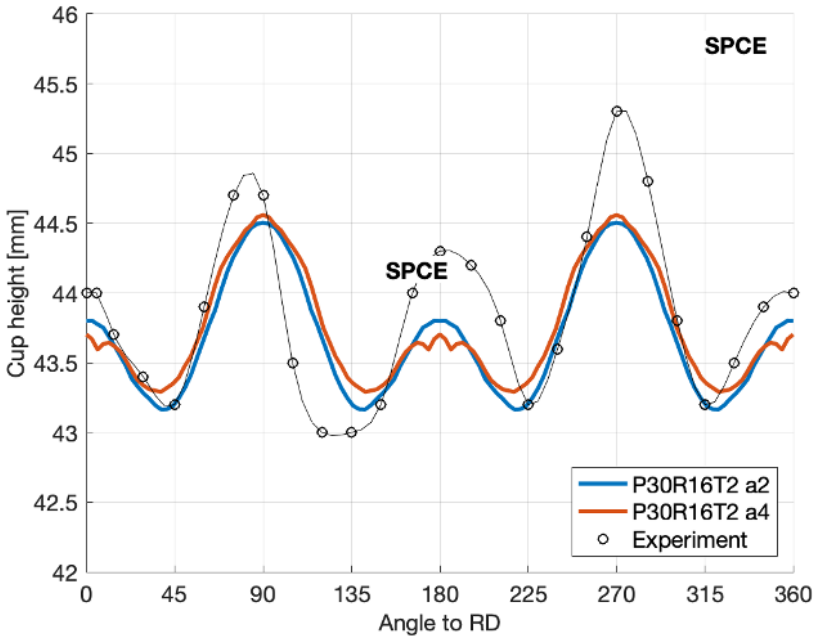
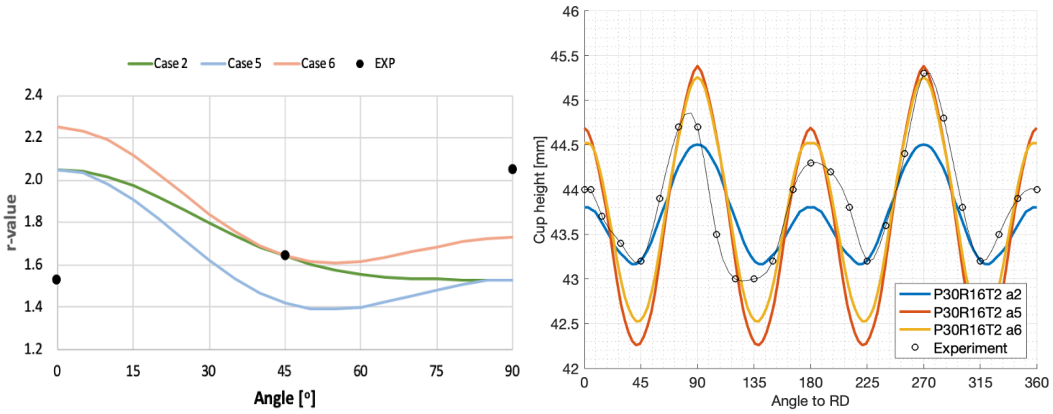


Fig. 4.32: Cup height prediction for different r-value: Case a2 and a4

In figure 4.32 the similar cup height prediction can be seen by increasing the all r-values linearly. It shows the shift/increase in cup height.



(a) a) r-value evolution

(b) b) Case a5 & a6: Cup height

Fig. 4.33: Case a5 and a6: Cup height and earing prediction: SPCE

In figure 4.33 a) the r-value evaluation is shown. It can be seen that the values

don't pass through the experimental data points. Figure 4.33 b) shows the effect of changing r_0 and r_{45} simultaneously. It can be seen that the cup height prediction is higher at 0 and 90 degrees and predicts lower and 45 degrees. Hence, it is very clear that the height prediction is very much sensitive with the r-values of the material.

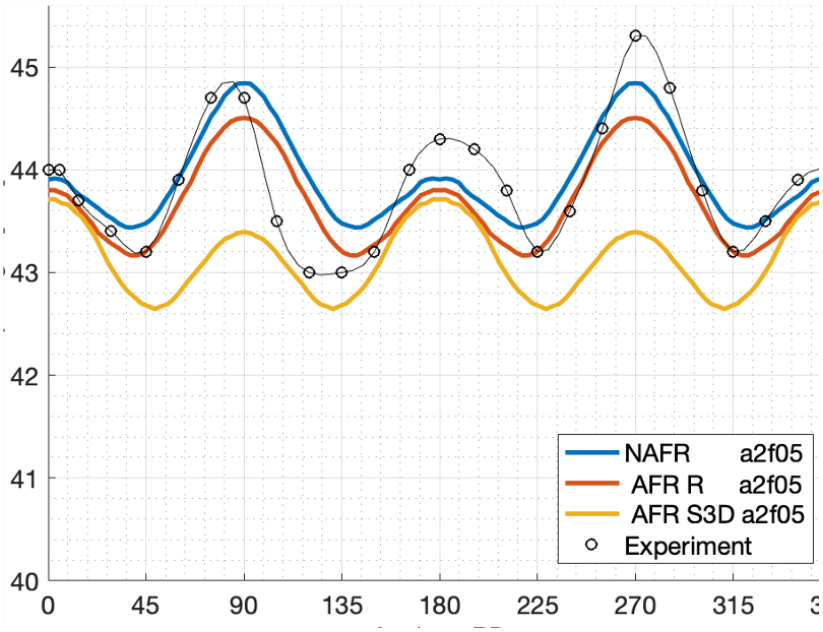


Fig. 4.34: Cup height prediction using proposed r-values

Figure 4.34 shows the cup height prediction using three different models with the case a2 r-values. It can be seen that the cup height and earing prediction using AFR-r is very much close to the experimental values. Also it follows the profile of the earing. In case of 3D AFR-σ the earing profile follows the experimental results but predicts different height.

In case of 3D NAFR case, this is the approach which gives the closest results to the experimental values, in terms of cup height as well as the earing profile. Hence, with the new proposed r-values and NAFR it can be seen that the numerical prediction of such cylindrical cup forming the best results when compared to experiment. The comprehensive responses of SPCE material at different anisotropic parameters and forming variables were presented. Anisotropic yield criterion was able to predict the material response at different r_0, r_{45} and r_{90} values. It is observed that, by using a better constitutive model such as NAFR using Hill'48, the predicted cup height and earing can be more accurate than the AFR models.

5 APPLICATION TO CUP DRAWING AND SPRINGBACK

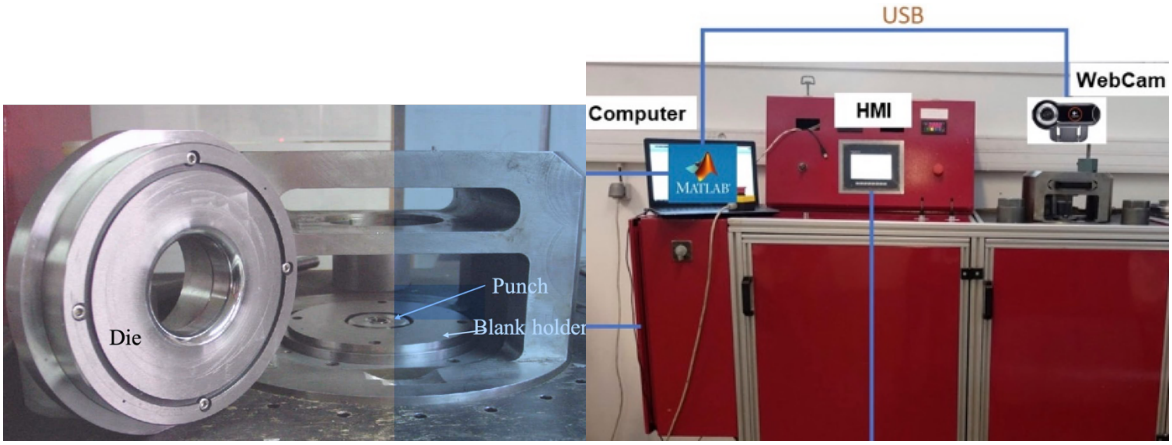
In this chapter an available experimental cylindrical cup test is presented and used to assess and investigate the effect of selected anisotropic constitutive models on the predictive capabilities for cup drawing and corresponding earing evolution, in addition to predicting cup springback, after a cup vertical split. The cup test is experimentally performed for a DP780 steel and the comparative study for finite element simulations includes the three AFR approaches (AFR-R, AFR-SiP, AFR-S3D), as well as the two NAFR models (NAFR-SiP, NAFR-S3D) for Hill48 yield function, as defined in previous chapter.

5.1 Cylindrical cup drawing

5.1.1 Experimental setup

The cylindrical cup test is an available possibility at INEGI, which is performed at an universal sheet metal testing machine, figure 5.1. The machine has been recently retrofitted with updated CNC control as well as improved capabilities for data acquisition [67] and, by changing pairs of tools, permits a series of formability tests such as Nakajima, Fukui, Marciniak, Swift, Erichsen and hole expansion tests. The current cup test uses the tools for Swift test which are shown in figure 5.1b) with setup and corresponding dimensions as shown in figure 5.2.

The blank diameter is 114 mm and the blank thickness is of 0.8 mm.



(a) Universal testing machine (b) Parts of experimental tool

Fig. 5.1: Experimental universal testing machine and tool for cylindrical cup drawing (HMI: Human-Machine Interface)

The figure 5.1 shows the the actual tool setup and schematic used for the cylindrical cup test. To reduce the friction forces between the blank and tools contact surfaces during the experimental tests, a lubricant was applied to both sides of the circular blank.

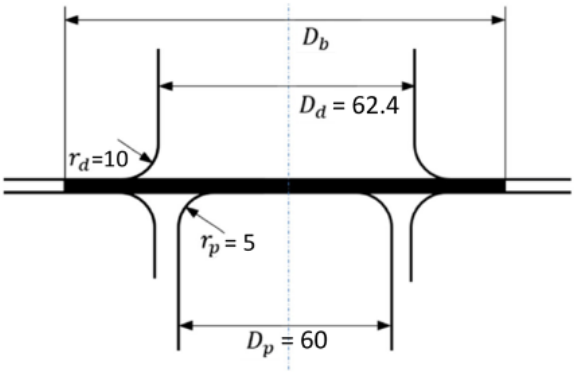


Fig. 5.2: Schematic view for cylindrical cup drawing test, with corresponding tool dimensions; blank diameter is 114 mm

5.1.2 Material properties and numerical model

The sheet material for present study is a DP780 steel, a material of current interest in automobile industry for its good balance on strength and formability, due to their micro-structure, in which a hard martensitic or bainitic phase is dispersed in a ductile ferritic matrix. These steels have additionally the capability of further increase on its yield strength, since they have bake hardening

properties, which can be possible by the paint baking process.
Cylindrical cup modelling has been already performed by [68] and the mechanical characterization of DP780 steel has also been a research topic of Amaral et al. [69] as well as Xue at el. [70] and such fundamental properties are used and presented in Table 5.1. As for the hardening curves of DP780 for tensile and shear tests, they are shown in figure 5.3 [70].
The values of Hill48 anisotropic coefficients are calculated using the expressions shown in table 2.1 to obtain potential surface and yield surface respectively. The two set of such Hills parameters values are shown in table 5.2.

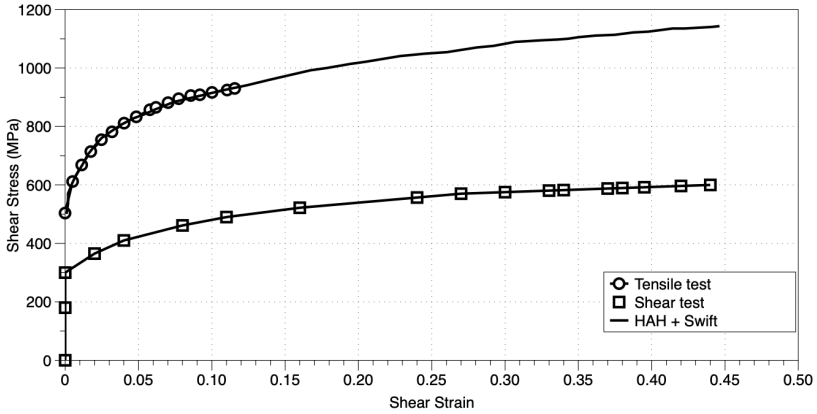


Fig. 5.3: DP780 hardening curves from tensile test and shear test (adapted from [70])

Table 5.1: Mechanical properties for DP780 material

E (MPa)	ν	r_0	r_{45}	r_90	k	ϵ_p	n	σ_0	σ_{45}	σ_{90}	σ_b	τ_{xy}/σ_0
210000	0.3	0.70	1.05	0.88	1319	0.0015	0.149	526.2	537.7	517.8	566.4	0.60

Table 5.2: Values of Hill'48 parameters for DP780

Based on	F	G	H	L	M	N_p	N_{3D}
r-values	0.468	0.588	0.412	1.5	1.5	1.64	-
stress	0.45	0.42	0.58	1.50	1.50	1.48	1.39

The numerical model of cup test to be implemented in Abaqus/Explicit is using rigid tools with analytical surfaces and the blank is discretized with 8-node linear brick elements of reduced integration (C3D8R, available in the Abaqus library) having three elements along thickness. The mesh for blank is presented

in figure 5.4 with half symmetry being used, according to the methodology for the springback modelling, as it will be presented in section 5.2. A constant Coulomb friction coefficient of 0.05 is defined for the interacting surfaces. The sheet blank is defined as an elasto-plastic material with hardening evolution behavior modeled by Swift law and corresponding parameters defined in Table 5.1.

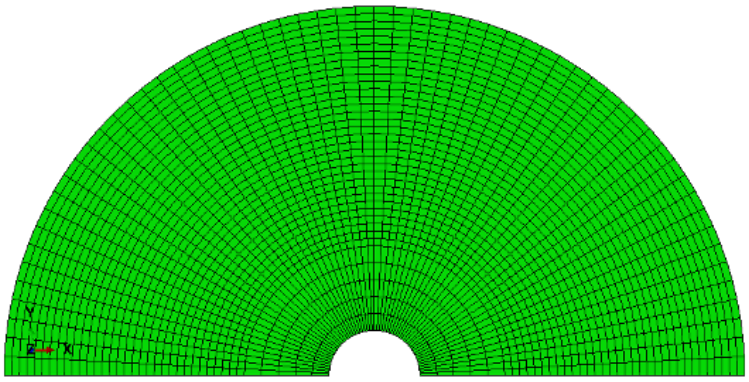


Fig. 5.4: Mesh used for cylindrical cup drawing test: total number of Elements = 6660; 3 elements along thickness; blank thickness: 0.8 mm; blank size: 114 mm; element type: C3D8R (8-node linear brick)

As shown in the figure 5.4, due to symmetry one half model was used for the simulation.

5.1.3 Cup height evolution, stress and strain contours

The cylindrical cup deep drawing test represents a very effective test for evaluation of anisotropic material models by analyzing the predicting behavior of earing evolution and its amplitude.

In this section cup height evolution is being assessed by comparison of different results obtained by several approaches for the anisotropic constitutive modelling.

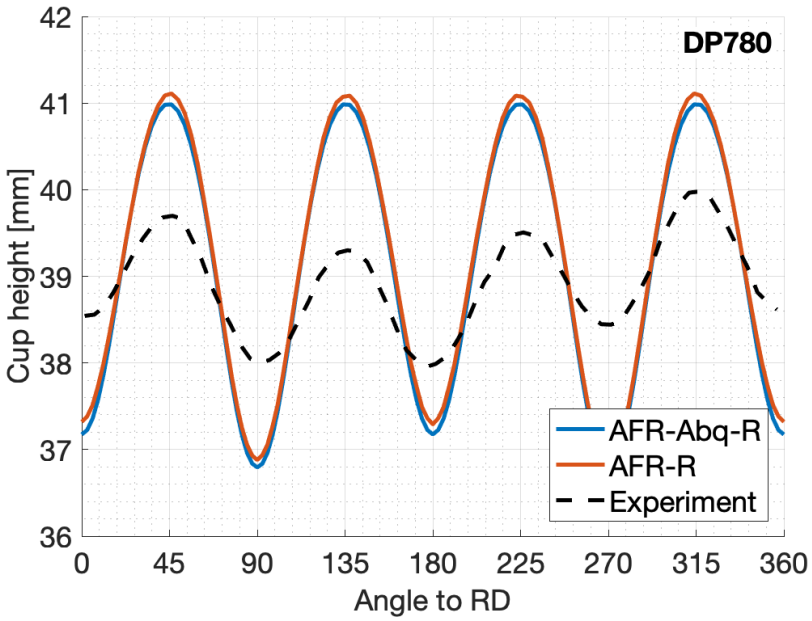
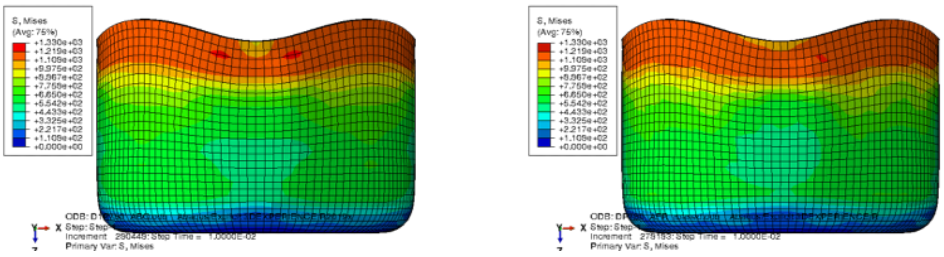


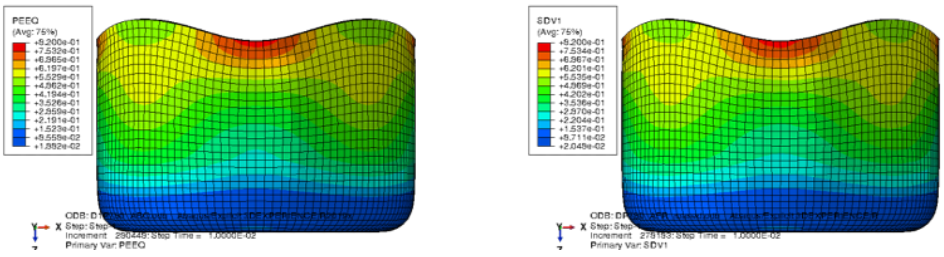
Fig. 5.5: Cup height evolution using Abaqus code (r-based anisotropy) and using User subroutine with AFR r-based approach

Figure 5.5 presents the prediction of earing evolution obtained by Abaqus code without user subroutine and the same kind of results obtained with developed user subroutine, both being AFR (Associated Flow Rule) with r-based anisotropic parameters. As seen, both results agree quite closely between them, which means that implemented user subroutine is validated, since it obtains the same results as those from a well-tested and validated implementation in Abaqus code. On the other hand, it is seen that when comparing to experimental earing profile, the predicted amplitude from simulation is overestimated. The same comparison is performed for results of equivalent stress and strain distribution, as shown in figures 5.6 and 5.7. As seen, the same tendency for very close results is observed, between the two methods, which again reinforces the correct implementation of user subroutine for AFR-r based model.



(a) (b)

Fig. 5.6: a) Equivalent stress contours using Abaqus code and b) using User subroutine with AFR r-based approach



(a) (b)

Fig. 5.7: a) Plastic equivalent strain contours using Abaqus code and b) using User subroutine with AFR r-based approach

AFR results for different approaches:

The results when comparing the three implemented AFR approaches is presented in figure 5.8. The main evidence is seen for the opposite evolution, when compared to experimental data, of highs and lows of earing profile for stress-based parameters, as obtained when using AFR-SiP and S3D approaches. It is also seen that the amplitude of these approaches is closer to the experimental result than the AFR-r based approach. As for stress and strain distribution, figures 5.9 and 5.10 show that different earing evolution is a primary reason for the visible differences seen on the main two kind of observed contours. Additionally, for the same type of predicted earing evolution (AFR-SiP and S3D) the different amplitude by these approaches also cause some difference on contours, specially seen on strain results (figure 5.10).

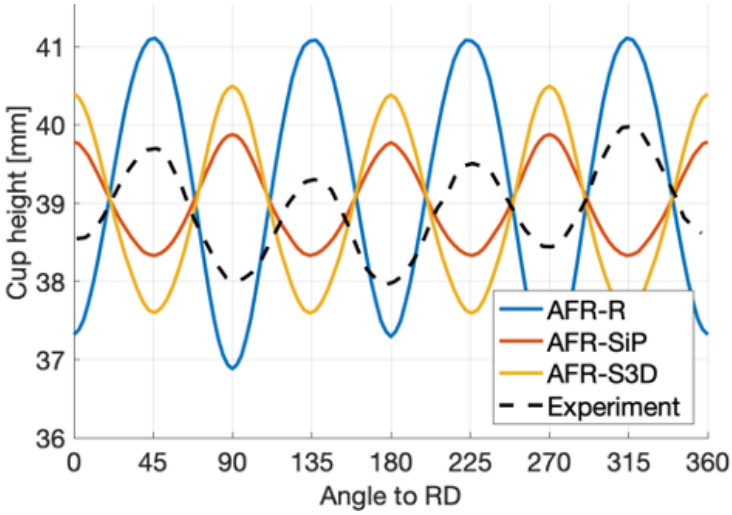


Fig. 5.8: Cup height evolution along different angles to the rolling direction for AFR approaches and comparison with experiment

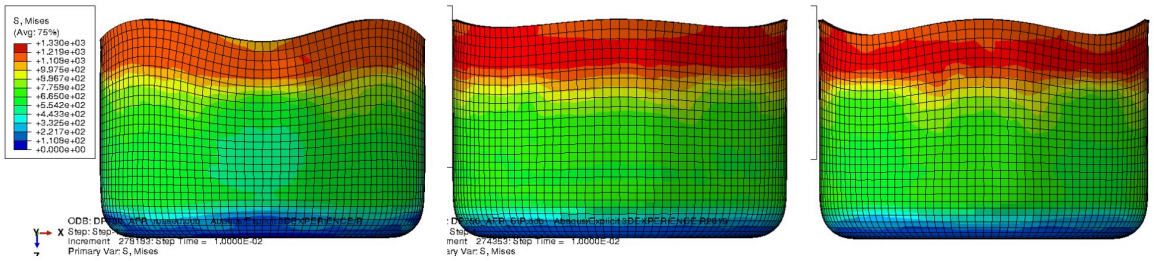


Fig. 5.9: Equivalent stress contours using AFR-R (left), AFR-SiP (center) and AFR-S3D (right)

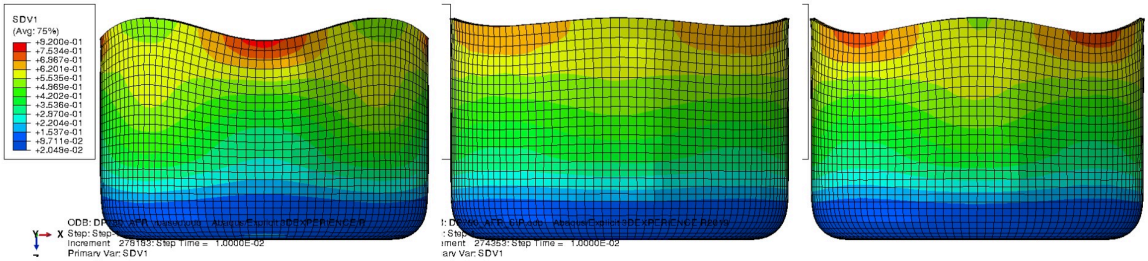


Fig. 5.10: Plastic equivalent strain contours using AFR-R (left), AFR-SiP (center) and AFR-S3D (right)

NAFR results for different approaches:

Amplitude creates between them some visible differences, especially visible on strain distribution.

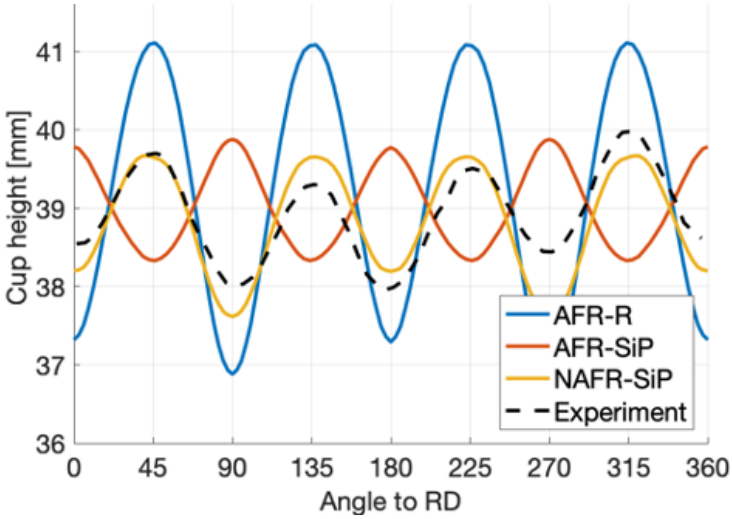


Fig. 5.11: Cup height evolution along different angles to the rolling direction for NAFR-SiP and corresponding AFR approaches with comparison to experiment

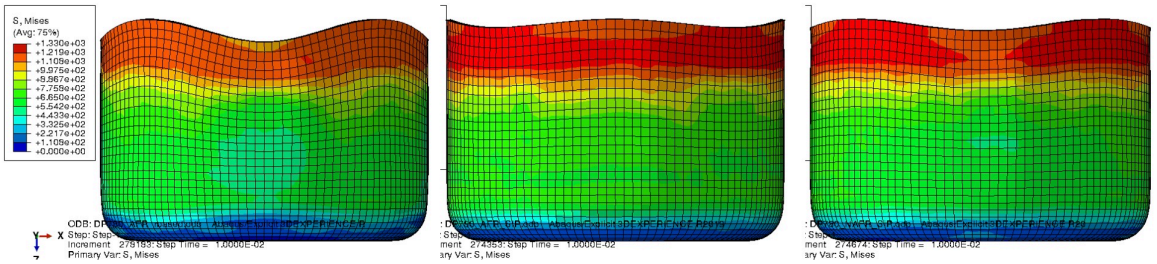


Fig. 5.12: Equivalent stress contours using AFR-R (left), AFR-SiP (center) and NAFR-SiP (right)

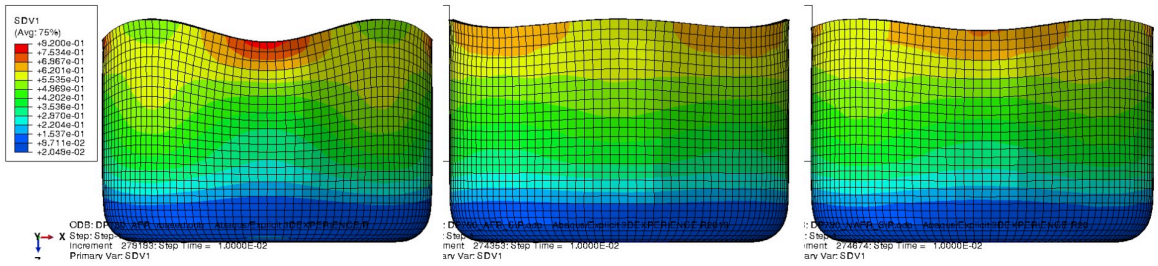


Fig. 5.13: Plastic equivalent strain contours using AFR-R (left), AFR-SiP (center) and NAFR-SiP (right)

A similar comparison to the previous one is performed for NAFR-S3D approach. Their results are shown in figure 5.11 for cup height evolution and figures 5.15 and 5.16 for stress and strain distributions, respectively. Such figures show that previous stated analysis (NAFR-SiP) shall apply: 1) AFR approaches have

non-conform amplitude or earing evolution, but the resulting NAFR approach obtains a correct earing evolution and an approximate earing amplitude to the experimental results; 2) stress and strain distributions show that the same earing profile evolution from AFR-R and NAFR-S3D approximates their results compared to AFR-S3D, but their different predicted amplitude creates between them (AFR-R vs. NAFR-S3D) some visible differences, especially visible on strain distribution.

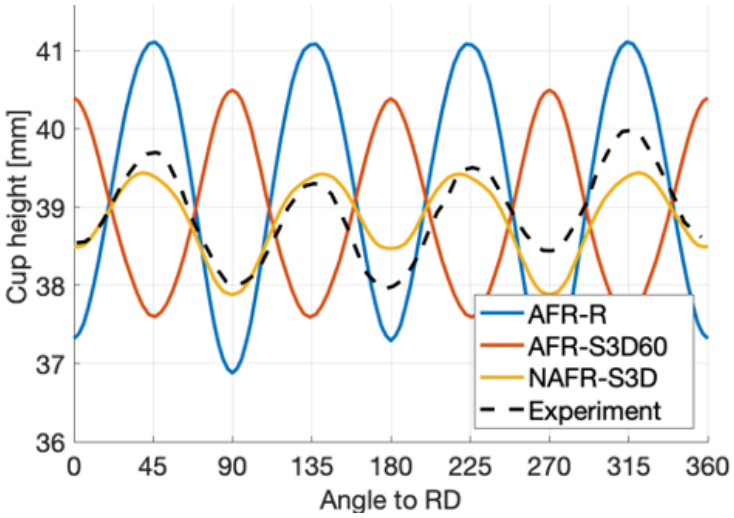


Fig. 5.14: Cup height evolution along different angles to the rolling direction for NAFR-SiP and corresponding AFR approaches with comparison to experiment

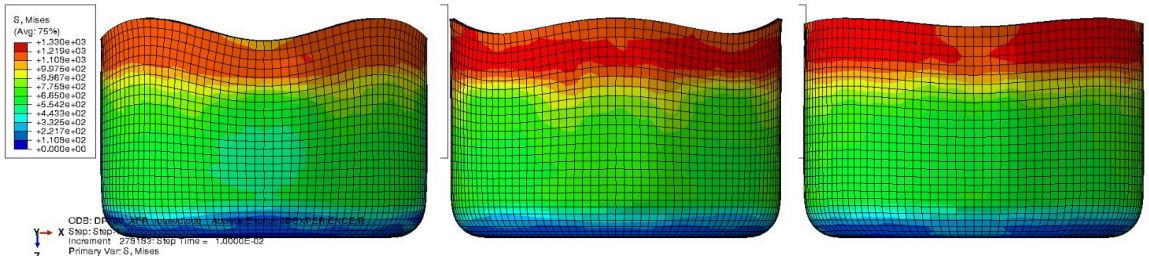


Fig. 5.15: Equivalent stress contours using AFR-R (left), AFR-S3D (center) and NAFR-S3D (right)

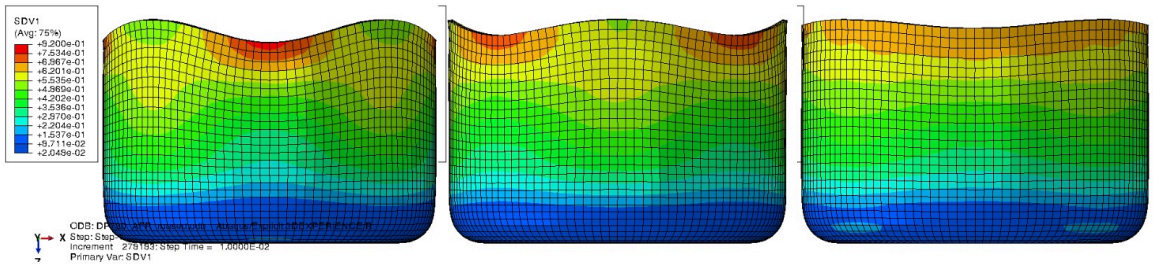


Fig. 5.16: Plastic equivalent strain contours using AFR-R (left), AFR-S3D (center) and NAFR-S3D (right)

The comparison for the two NAFR approaches is presented in figures 5.17, for cup height evolution and figures 5.18 and 5.19 for stress and strain distributions, respectively. Concerning cup height evolution, it is seen that both approaches show a similar performance when compared to experiment.

Now that results of simulation and experiment are found to be in a similar level for theses NAFR approaches, one should also consider about experimental results themselves. Until now, the experimental result has shown to be a good reference for comparison, since some of the numerical results were quite far from experiment. However, as any measurement, experiments shall have associated with them a level of uncertainty for obtained results, which is not presented here and it was not yet possible to be done under this research. If one takes a second view to the experimental cup height evolution (e.g. figure 5.17) it is understood that repeatability of curve evolution does not behave as a mirror for one quarter of the cup or even for half of the cup, due to the anisotropy that is expected for sheets after the rolling process. The experimental cup height evolution besides being a result from sheet anisotropy may have influence from other variables like initial centering of blank, centering during forming, possible ironing between blank-holder and die at the final stage of forming, method for measurement of cup height, etc.

With previous clue on critically evaluating also the experimental results and understanding what level of uncertainty shall exist for them, one may return to figure 5.17 and having this in mind it seems clear that the level of dispersion for numerical simulation seems to be in a similar level to the dispersion or uncertainty of experimental results. Therefore it is not possible to evaluate which of the two NAFR approaches are closer to the best accuracy for prediction

of anisotropy for this cylindrical cup test and they both give representative good results. Also, these results and this analysis show that a step forward would be the improvement of higher accuracy concerning experimental results, which is a fundamental need when benchmarks for numerical validation are defined and performed.

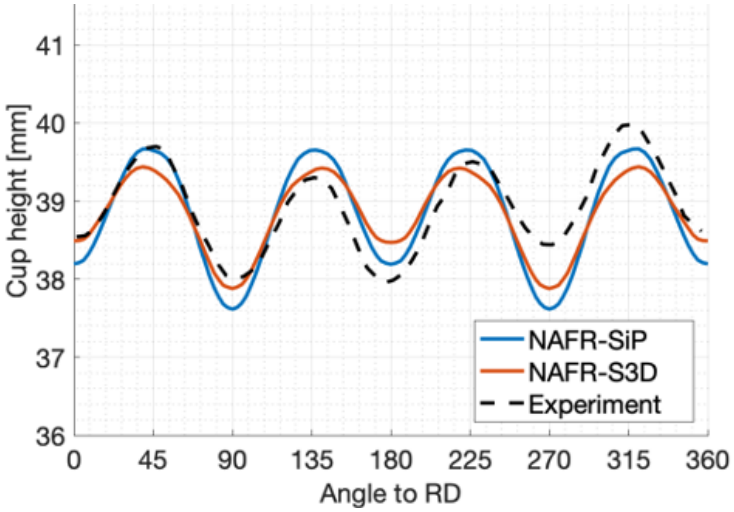


Fig. 5.17: Cup height evolution along different angles to the rolling direction for NAFR-S3D vs. NAFR-S3D with comparison to experiment

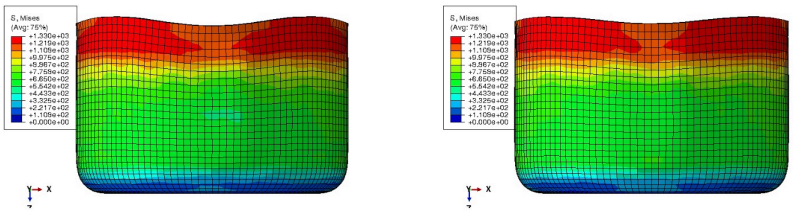


Fig. 5.18: Equivalent stress contours using NAFR-SiP (left) and NAFR-S3D (right)

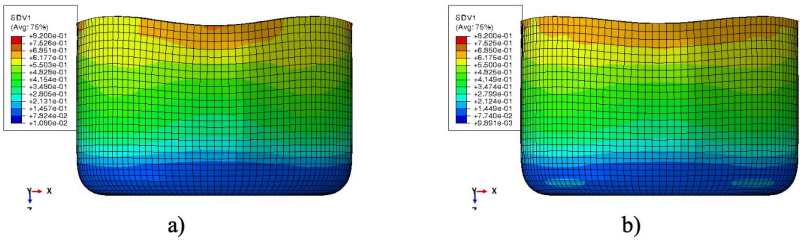
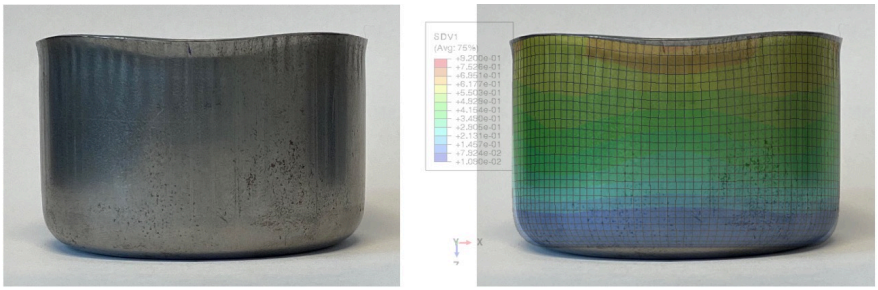


Fig. 5.19: Plastic equivalent strain contours using NAFR-SiP (left) and NAFR-S3D (right)

The additional comparisons for current cup deep drawing results are shown

in figures 5.20 and 5.21, which correspond to lateral views and 3D views of experimental geometry and geometry from numerical simulation using one of the two NAFR approaches (NAFR-SiP). As shown, both comparisons perform quite well as well as the overlapping presented in figure 5.20 a).



a) b)

Fig. 5.20: View of earing cup profile from experimental cup (left) and overlapping with simulation (right, from NAFR-SiP, figure 5.19 a)

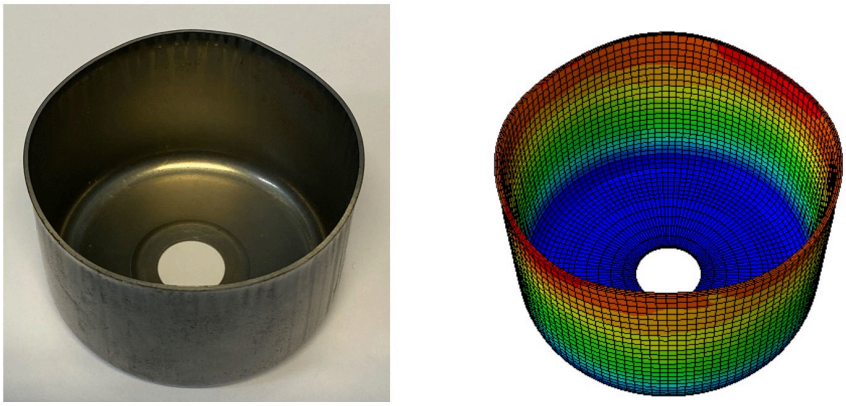


Fig. 5.21: View of cylindrical cup from experiment (left) and from simulation (right)

5.1.4 Thickness strain

For a successful deep drawing process, it is important to take into account the interaction between the blank, the die and the blank-holder. Accordingly, changes in thickness of the sheet metal shall be modelled as accurately as possible in simulation, since they will influence on the contact and friction stresses at the interfaces. Therefore, the analysis of thickness strain has been compared for each of AFR and NAFR approaches, along both rolling and transverse directions.

Thickness strain along rolling direction:

The predicted strain distribution through-thickness for the vertical section of the cup along the rolling direction is shown in figures 5.22 and 5.23. The comparison (figure 5.22 a) between Abaqus code without user subroutine and with developed user subroutine (both with AFR and r-based anisotropic parameters) show that both results agree quite closely, as already seen in previous comparisons, thus supporting the validation of implemented user subroutines. On the other hand, the comparison between all AFR approaches, figure 5.22 b), show that the three approaches are grouped in two types of behavior and the differences are mainly on the vertical wall region (initial xx coordinate greater than 40 mm). AFR-SiP and AFR-S3D have very coincident thickness distribution while AFR-R exhibits higher thickness strain along the vertical wall. Such two groups and the difference on strain distribution is related with the different prediction of earing evolution, which influences the thickness, due to constancy of volume in plastic deformation. Comparing AFR-SiP/AFR-S3D behavior with AFR-R behavior, this last approach is predicting lower cup height along rolling direction and higher thickness, which gives consequently higher thickness strain, as observed in figure 5.22 b). The lower thickness strain for AFR-SiP/AFR-S3D behavior is related with higher cup height and lower thickness. Comparing the NAFR approaches, figure 5.23, they show very similar behavior, close to AFR-R approach, but having lower thickness strain for region greater than 35 mm.

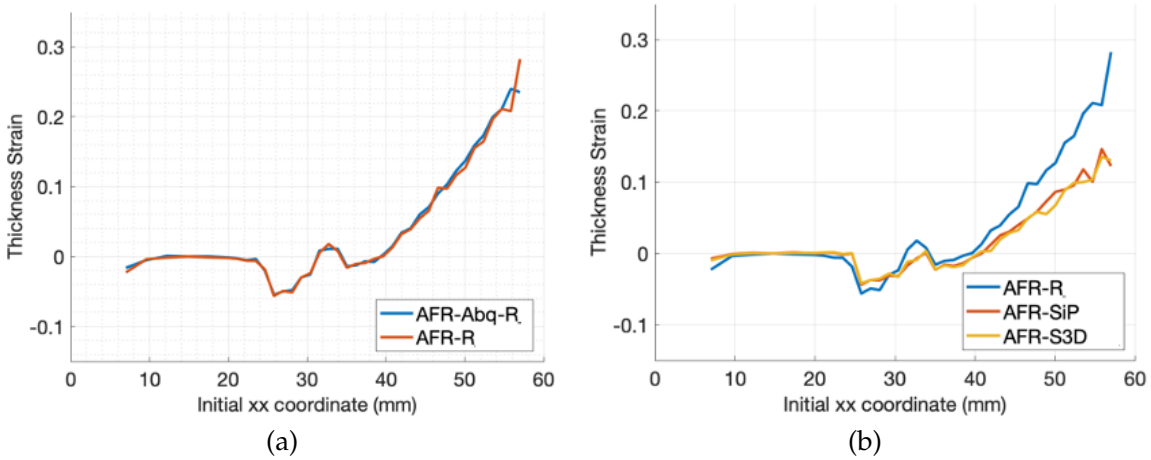


Fig. 5.22: Comparison of predicted thickness strain along Rolling direction for DP780; a) Abaqus code vs. User subroutine; b) User subroutine Associated Flow Rule approaches: AFR-R vs. AFR-SiP vs. AFR-S3D

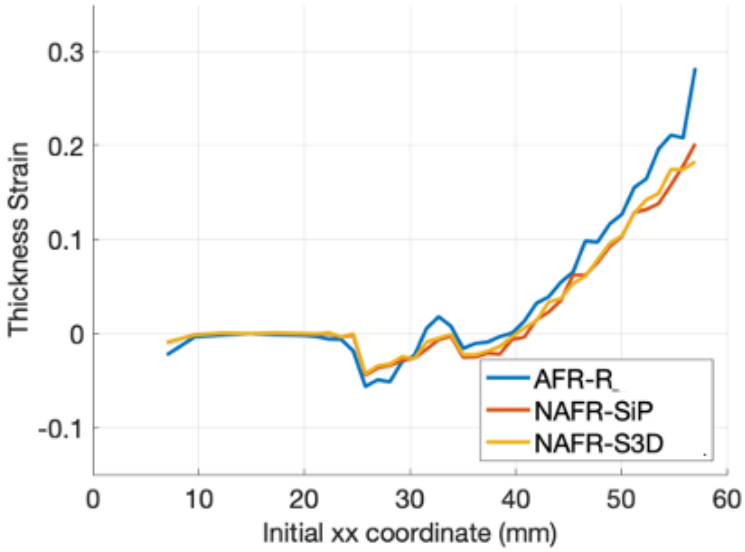


Fig. 5.23: Predicted thickness strain along Rolling direction for DP780

Thickness strain along transverse direction:

The predicted strain distribution for the vertical section of the cup along the transverse direction is shown in figures 5.24 and 5.25. The comparisons show that the tendencies observed for rolling direction are the same as for transverse direction. Although existing different thickness values between rolling and transverse directions for the same approach, the resulting strains show very small differences. On the other hand, when comparing the various approaches their differential at transverse direction is almost the same as for rolling direction, thus resulting on very similar tendencies (as with transverse direction).

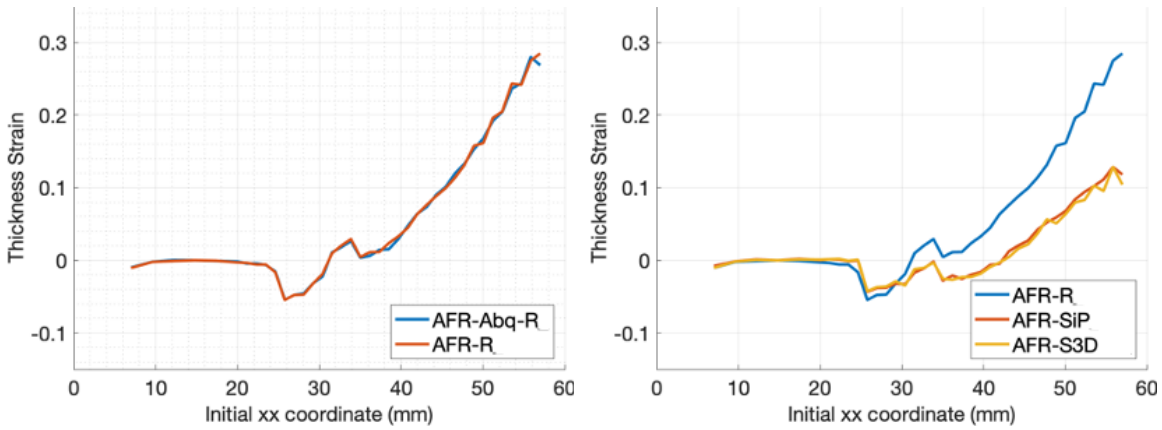


Fig. 5.24: Comparison of predicted thickness strain along Transverse direction for DP780; a) Abaqus code vs. User subroutine; b) User subroutine Associated Flow Rule approaches: AFR-R vs. AFR-SiP vs. AFR-S3D

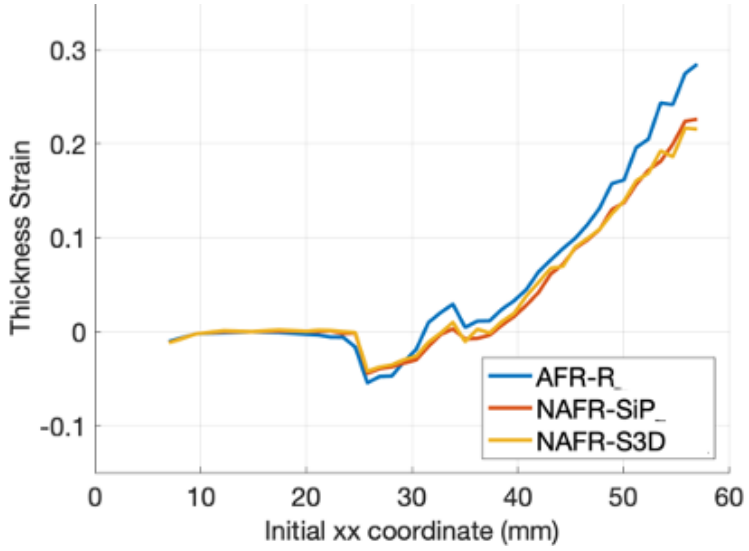


Fig. 5.25: Predicted thickness strain along Rolling direction for DP780 NAFR approaches and comparison with AFR-R

5.1.5 Sensitivity analysis for anisotropic parameter τ_{xy}/σ_0

In section 5.1.3 it was seen that cup earing evolution and therefore anisotropic constitutive modelling is dependent on the choice of flow rule approach, but at the same time each flow rule has its own parameters according to material characterization. It was also in section 5.1.3 that experimental results were questioned and it was stated that uncertainty should be part of information on experimental results. This context is the basis for studying and performing sensitivity analysis on parameter τ_{xy}/σ_0, which is defined for stress-based flow rules and S3D approaches. This parameter represents the ratio between yield stress for tensile loading versus yield stress for shear loading and it can be calculated from data of tensile and shear tests. This study will include a variation on the parameter from 0.40 to 0.70 and comparison of results with experimental earing evolution.

τ_{xy}/σ_0 parameter from 0.40 to 0.70 AFR-S3D:
The earing evolution for S3D parameter under analysis is shown in figure 5.26 for values from 0.40 to 0.70 with a variation step of 0.10. As seen, under these variation limits the earing behavior can include not only large and smaller amplitudes, but also an opposite behavior of highs and lows for earing evolution to the rolling direction. As a complementary analysis, the cup views, stress and strain contours for these results are presented in figures 5.27 and 5.28.

When comparing to experimental behavior the results would suggest that the parameter value would be inside the values of 0.50 and 0.60, due to the observed tendency. Therefore, a new analysis has been performed, now for limits between 0.54 and 0.60 with variation step of 0.02.

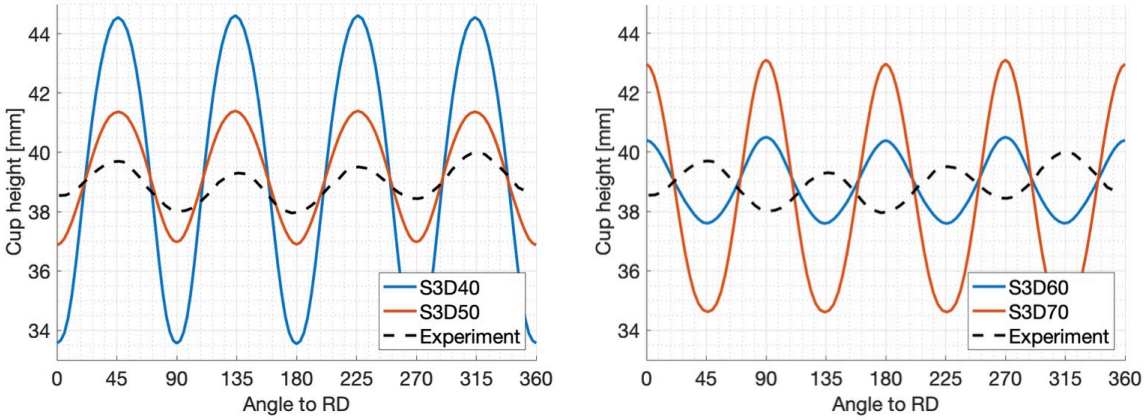


Fig. 5.26: Cup height evolution along different angles to the rolling direction for AFR-S3D and τ_{xy}/σ_0 parameter changing from 0.40 (left) to 0.70 (right), with comparison to experiment

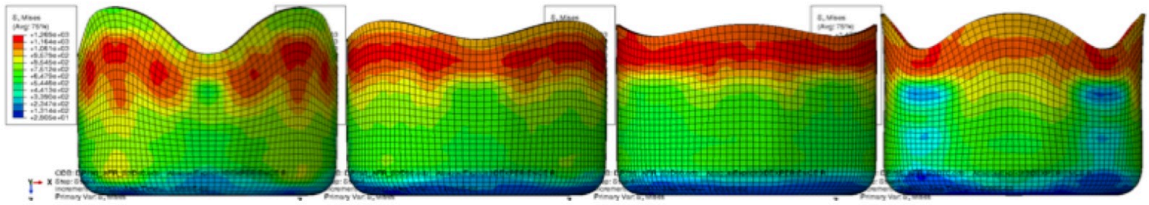


Fig. 5.27: Equivalent stress contours for AFR-S3D and τ_{xy}/σ_0 parameter being 0.40 (left), 0.50, 0.60 and 0.70 (right)

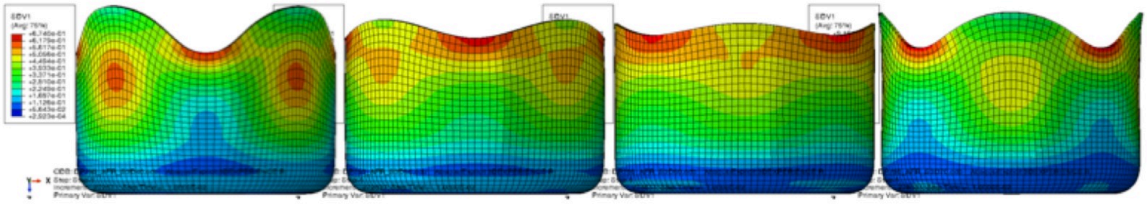


Fig. 5.28: Plastic equivalent strain for AFR-S3D and τ_{xy}/σ_0 parameter being 0.40 (left), 0.50, 0.60 and 0.70 (right)

τ_{xy}/σ_0 parameter from 0.54 to 0.60 AFR-S3D:

Figure 5.29 presents the earing evolution, now for S3D parameter limits between

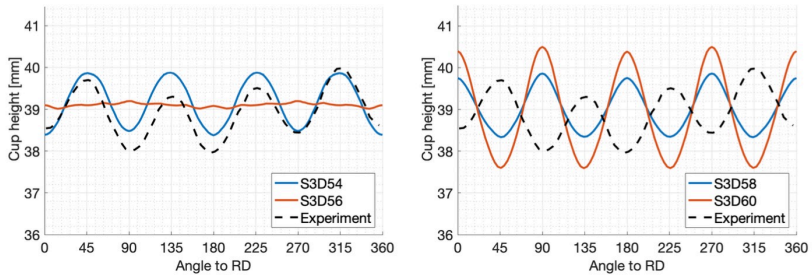


Fig. 5.29: Cup height evolution along different angles to the rolling direction for AFR-S3D and τ_{xy}/σ_0 parameter changing from 0.54 to 0.60, with comparison to experiment

0.54 and 0.60, which shows that such values include a close behavior to experiment (parameter value =0.54), a close behavior to material isotropy (parameter value = 0.56) and earing behavior with opposite evolution to experimental behavior (value of 0.58 and 0.60). Figures 5.30 and 5.31 show the corresponding cup views, as well as their stress and strain contours at final stage of forming.

These results would suggest that 0.54 for parameter would be the intuitive value to be used, if an associated flow rule would be followed. However, since this study includes NAFR approaches it is important to understand additionally what is the parameter sensitivity for this type of approach.

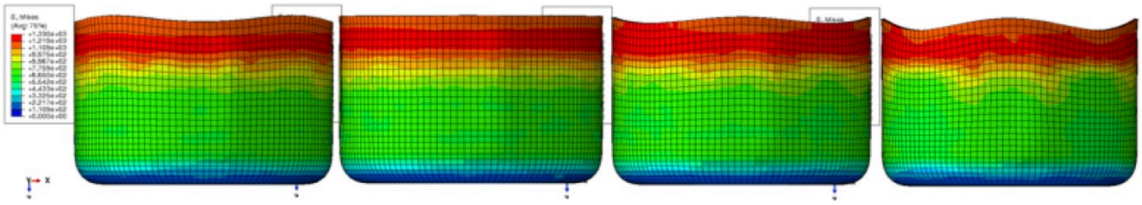


Fig. 5.30: Equivalent stress contours for AFR-S3D and τ_{xy}/σ_0 parameter being 0.54 (left), 0.56, 0.58 and 0.60 (right)

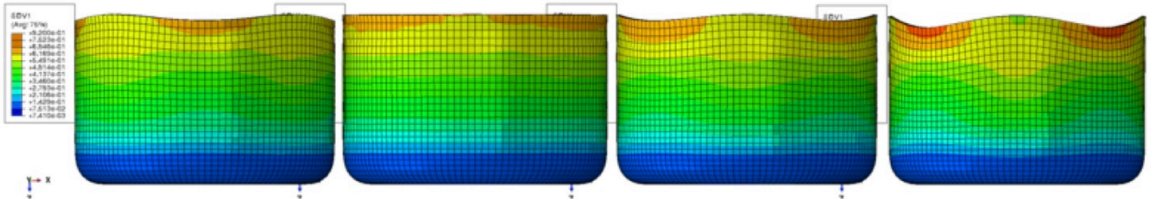


Fig. 5.31: Plastic equivalent strain contours for AFR-S3D and τ_{xy}/σ_0 parameter being 0.54 (left), 0.56, 0.58 and 0.60 (right)

τ_{xy}/σ_0 parameter from 0.54 to 0.60 NAFR-S3D:

The parameter sensitivity for NAFR-S3D approach on earing evolution for values between 0.54 and 0.60 is presented in figure 5.32 and corresponding cup views with stress and strain contours are shown in figures 5.33 and 5.34, respectively. As seen, now the behavior with NAFR-S3D approach is different from AFR-S3D for the same parameter values and the parameter that corresponds to a better performance when compared to experiment is the value of 0.60, which is the calculated parameter according to experimental data.

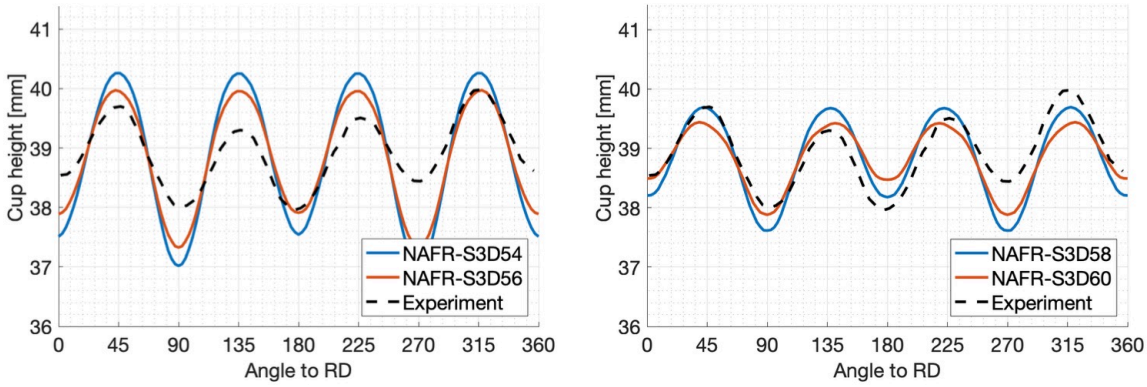


Fig. 5.32: Cup height evolution along different angles to the rolling direction for NAFR-S3D and τ_{xy}/σ_0 parameter changing from 0.54 (left) to 0.60 (right), with comparison to experiment

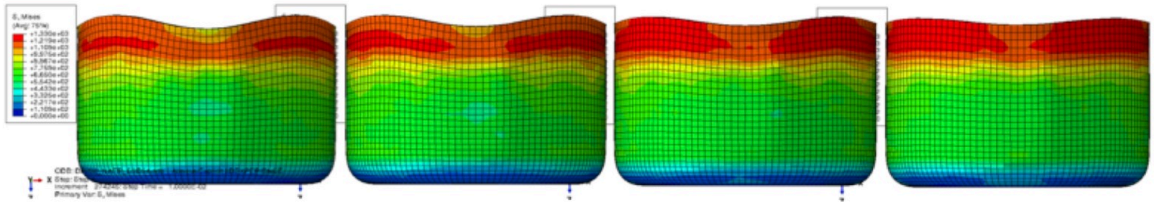


Fig. 5.33: Equivalent stress contours for NAFR-S3D and τ_{xy}/σ_0 parameter being 0.54 (left), 0.56, 0.58 and 0.60 (right)

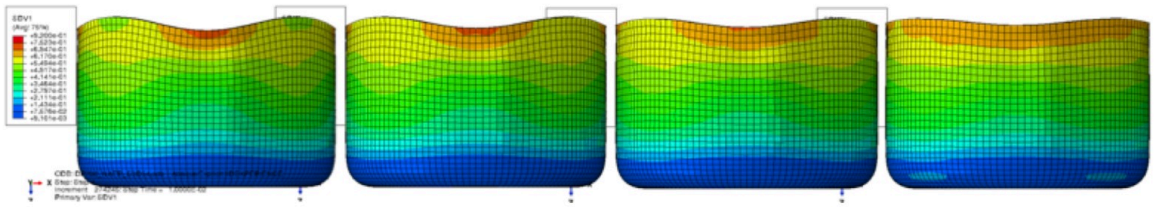


Fig. 5.34: Plastic equivalent strain contours for NAFR-S3D and τ_{xy}/σ_0 parameter being 0.54 (left), 0.56, 0.58 and 0.60 (right)

5.2 Cup split and springback

The predictive numerical capabilities in sheet metal forming processes, besides formability analysis, should always include springback, since this phenomenon changes the geometry of finished part after being released from tools, affecting the dimensional accuracy of a component and tryout loops being needed for tools, to compensate for its behavior. As seen previously, the anisotropic constitutive models play an important role on the prediction of the formed part and this suggests to include the investigation on the influence of anisotropy modelling on springback prediction. Traditionally, the cylindrical cup test is also being used for springback analysis by cutting a ring from the wall of a drawn cylindrical cup and splitting it, thus freeing the circular shape and using the new geometry as a measure of elastic recovery or springback [33,71].

In current investigation it is proposed and used an alternate methodology, which has been implemented due to its higher simplicity and the current available possibilities for experimental work.

5.2.1 Experimental methodology and numerical modelling

As seen in figure 5.35, the cup vertical split, for springback analysis, consists in cutting the cup vertical wall and partially cutting the cup base. This process will release the circular geometry and the opening can be analysed, as well as the corresponding vertical wall section. The cutting has been performed with a circular saw, which removes material with a 2 mm width.



Fig. 5.35: View of experimental cylindrical cup, after being split along Rolling direction (cutting with a circular saw, 2 mm width)

The numerical simulation of springback is performed by using the final geometry and data from cup forming and, as next step, applying the adequate boundary conditions adjusted to the experimental process. Having springback simulation in mind, the cup forming was modelled with half model and applying corresponding symmetry boundary conditions with Abaqus/Explicit. This half model, after deep drawn, has then its analysis imported into Abaqus/Standard, in which a static analysis is performed. The boundary conditions for springback are shown in figure 5.36 and they correspond to symmetry conditions applied to the non-split part of cylindrical cup, in addition to fixed points on the hole of cup base to prevent displacements along xx and zz directions and rotation along yy direction.

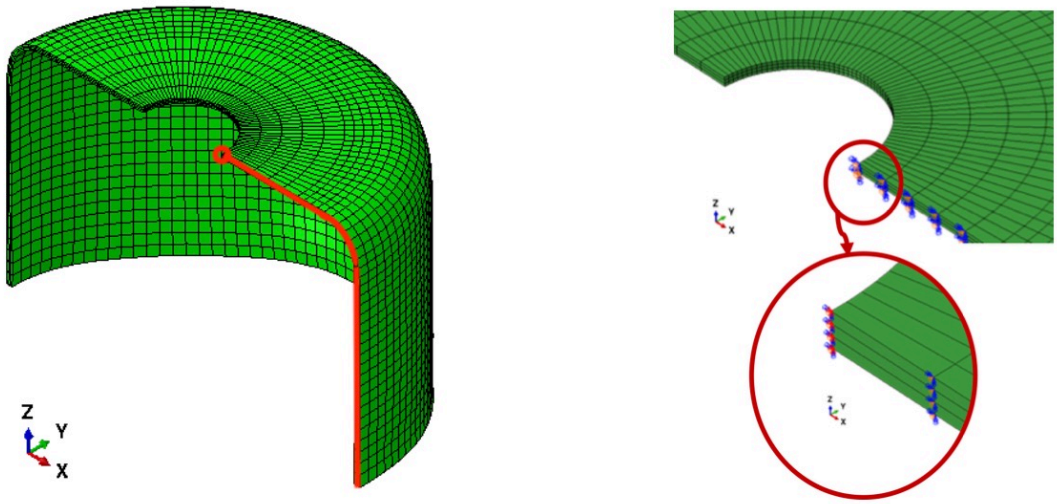


Fig. 5.36: Boundary conditions for springback simulation: symmetry condition for a lateral xz face and fixed points for xx and zz directions

5.2.2 Stress contours and springback

In this section each AFR and NAFR approach has its results of stress and displacement visualized as contours and compared. The stress contours are visualized before and after springback, being possible to understand the residual stress distribution, since the non-uniform distribution of residual stress produced by the deep drawing process is the main factor for elastic relaxation and springback.

Figures 5.37 and 5.38 show the results, respectively, for Abaqus code without user subroutine and Abaqus with developed user subroutine (both with AFR and r-based anisotropic parameters). As in previous comparisons, both results agree quite closely, thus supporting again the validation of implemented user subroutines.

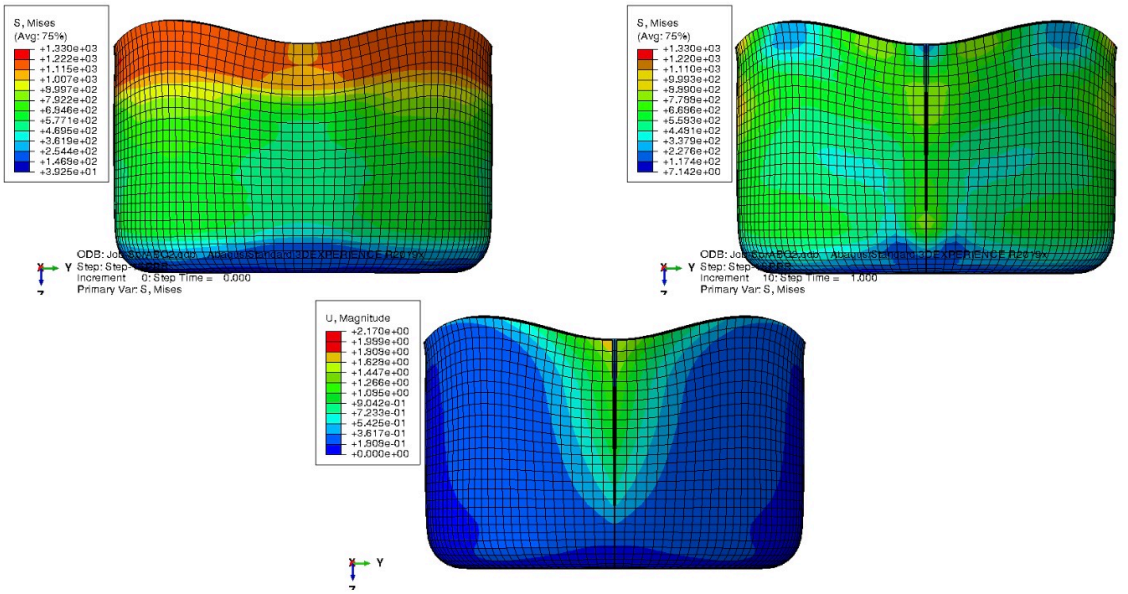


Fig. 5.37: Contours for equivalent stress, before springback (top left), after springback top right) and displacement contour (down), for Abaqus code (AFR r-based)

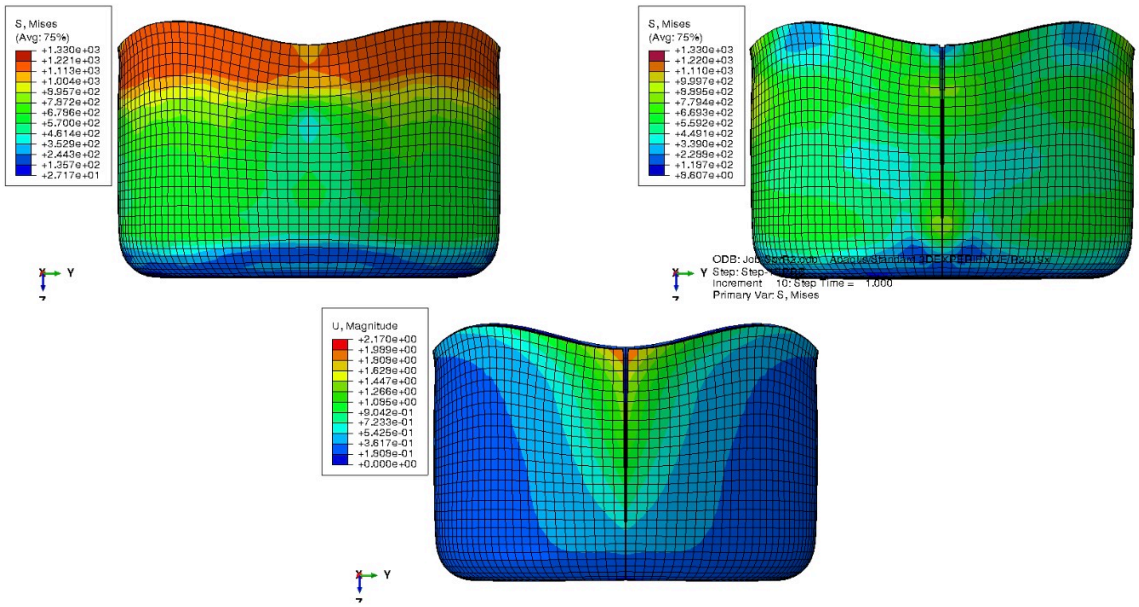


Fig. 5.38: Contours for equivalent stress, before springback (top left), after springback top right) and displacement contour (down), for user subroutine AFR r-based

When comparing every approach and its results, from figures 5.38 to 5.42, it is clear that the predicted cup earing profile, which affects also cup geometry shall have an evident influence on springback behavior, since different geometries will

create different restrictions for elastic recovery. This also shows that anisotropic constitutive modelling by playing a role on final geometry after forming will have a great influence on springback, besides the accurate modeling of residual stresses (both also being connected).

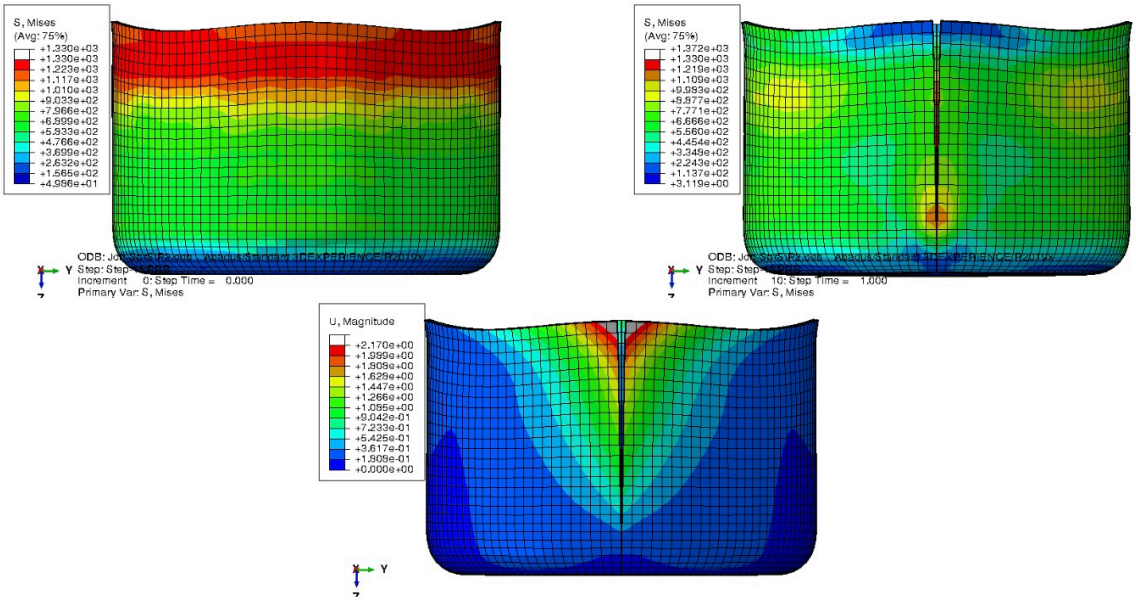


Fig. 5.39: Contours for equivalent stress, before springback (top left), after springback top right) and displacement contour (down), for user subroutine AFR S in Plane

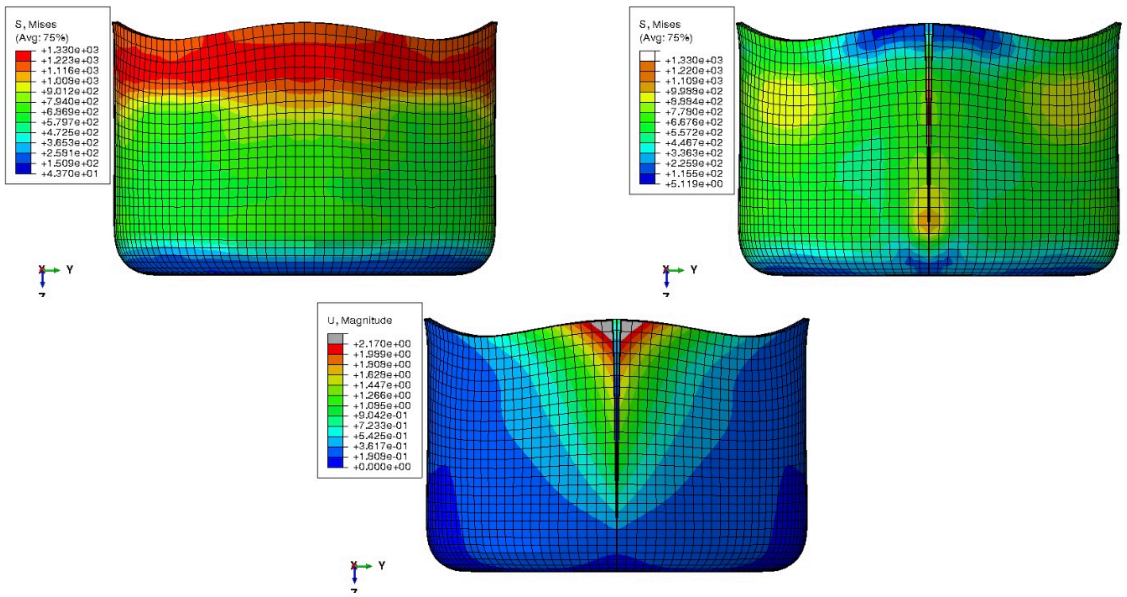


Fig. 5.40: Contours for equivalent stress, before springback (top left), after springback top right) and displacement contour (down), for user subroutine AFR S3D

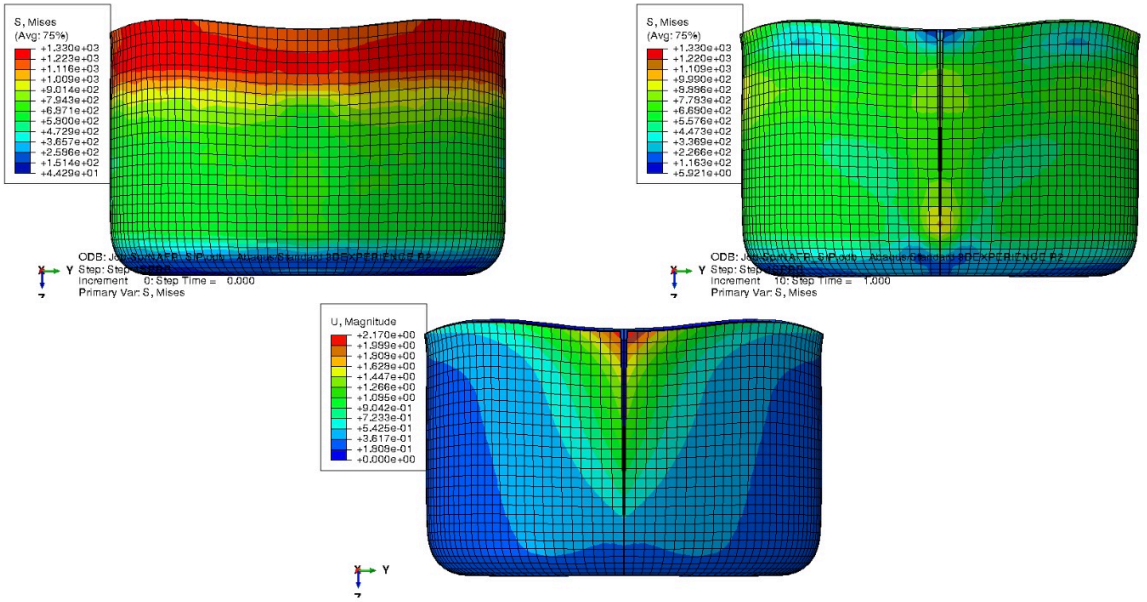


Fig. 5.41: Contours for equivalent stress, before springback (top left), after springback top right) and displacement contour (down), for user subroutine NAFR S in Plane

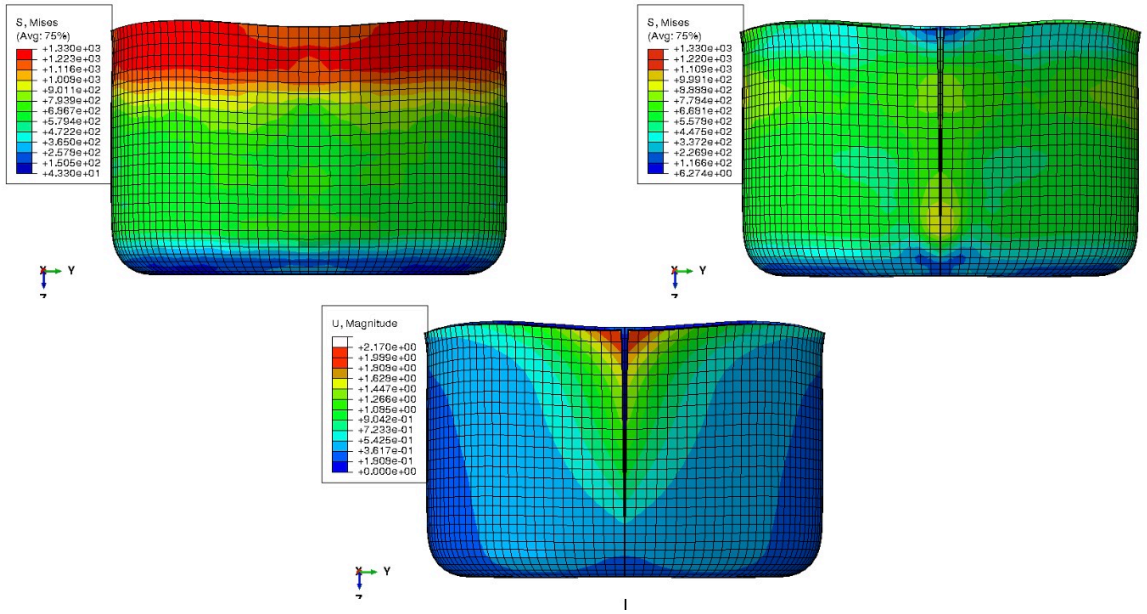


Fig. 5.42: Contours for equivalent stress, before springback (top left), after springback top right) and displacement contour (down), for user subroutine NAFR S3D

Figure 5.43 compares the cup lateral profile after springback (split side of cup) for the AFR approaches. As seen, two types of behavior are observed: AFR-R and AFR-SiP/AFR-S3D, which when observing corresponding geometries

(figure 5.43 b) suggests that corresponding different cup height profile is the leading factor for existing these two groups of behavior.

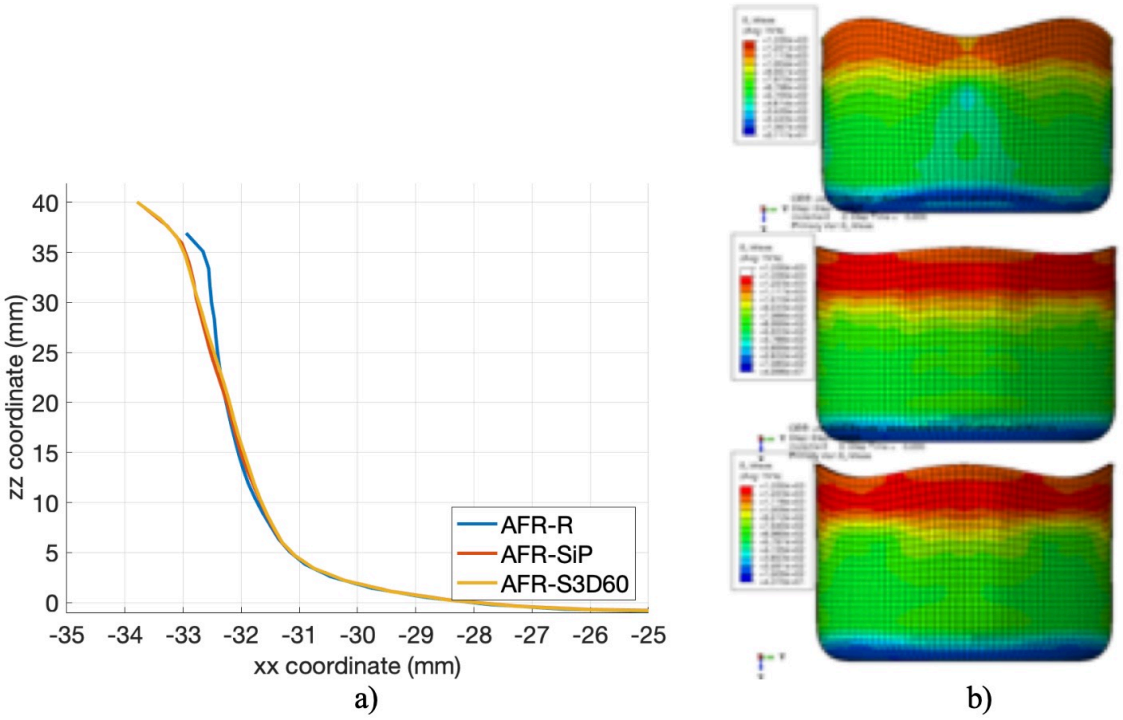


Fig. 5.43: Contours for equivalent stress, before springback (top left), after springback top right) and displacement contour (down), for user subroutine NAFR S3D

As with AFR approaches, now the comparison is done for NAFR approaches, seen in figure 5.43, which also includes AFR-R as a reference. As observed and suggested for AFR approaches, now the same conclusions can be withdrawn, since the same similar earing prediction is giving very close results. As additional data, it is presented in figure 5.45 the lateral cup sections, before springback, for every flow rule approach and it may be observed that globally the cylindrical surface of cup is very similarly represented by every approach, except on the height of profile, which is different dependent on corresponding approach. Also, the geometric views, with displacement contours, in xz and xy coordinate planes are presented in figures 5.46 and 5.47, for every approach in this study. They show a good correspondence to what was already observed for cup lateral profiles, seen in figures 5.43 and 5.44.

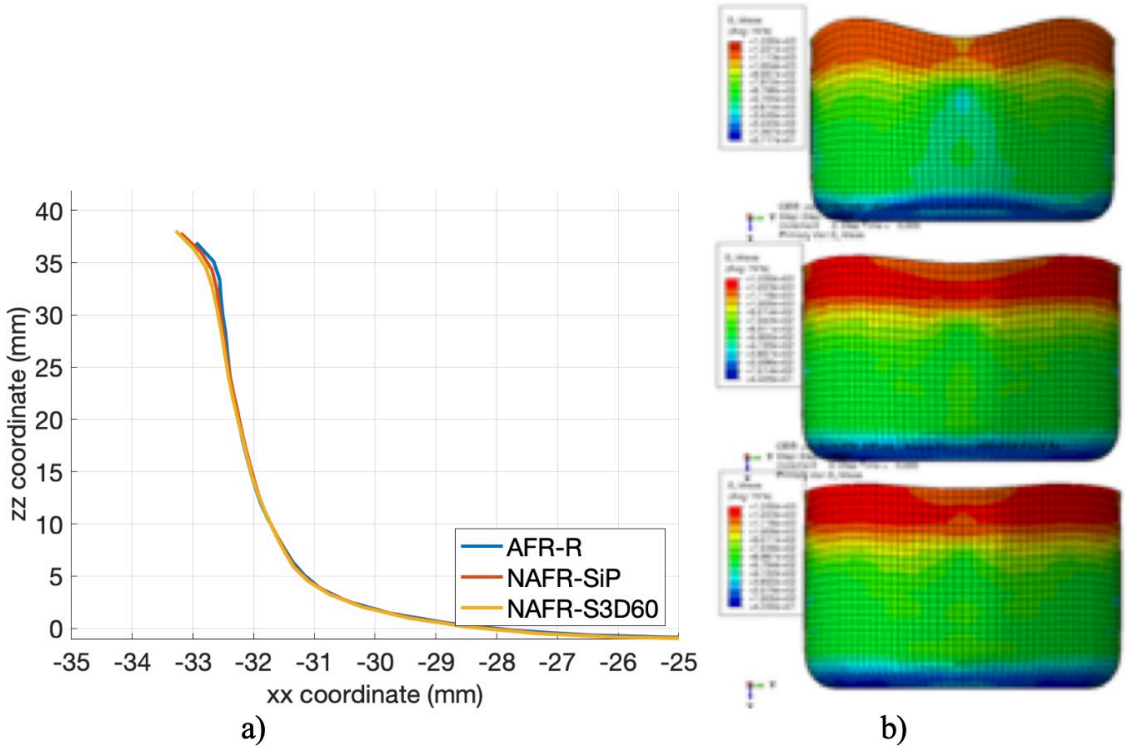


Fig. 5.44: Lateral profile section (cutting side) After Springback, predicted by NAFR-SiP vs. NAFR-S3D approaches and comparison with AFR-R

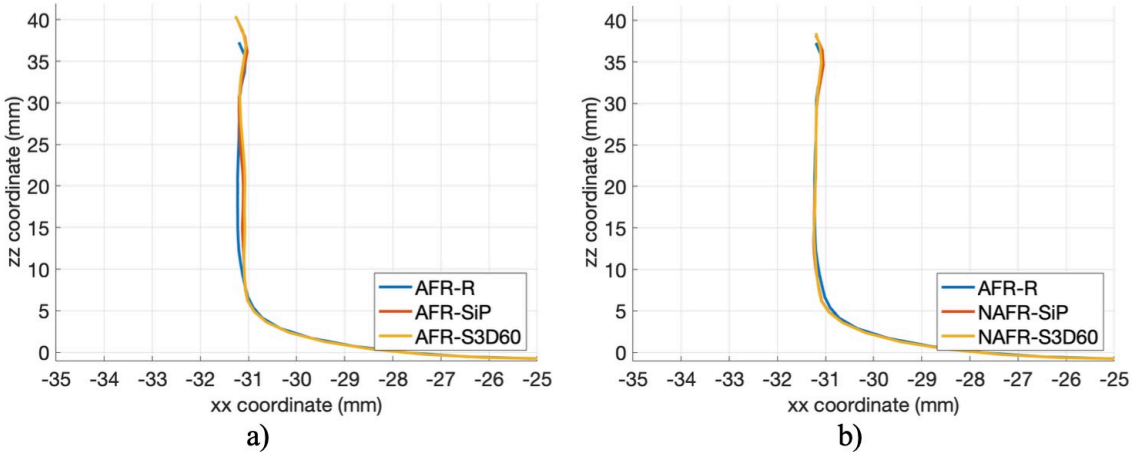


Fig. 5.45: Lateral profile section (cutting side) Before Springback, predicted by different AFR and NAFR approaches

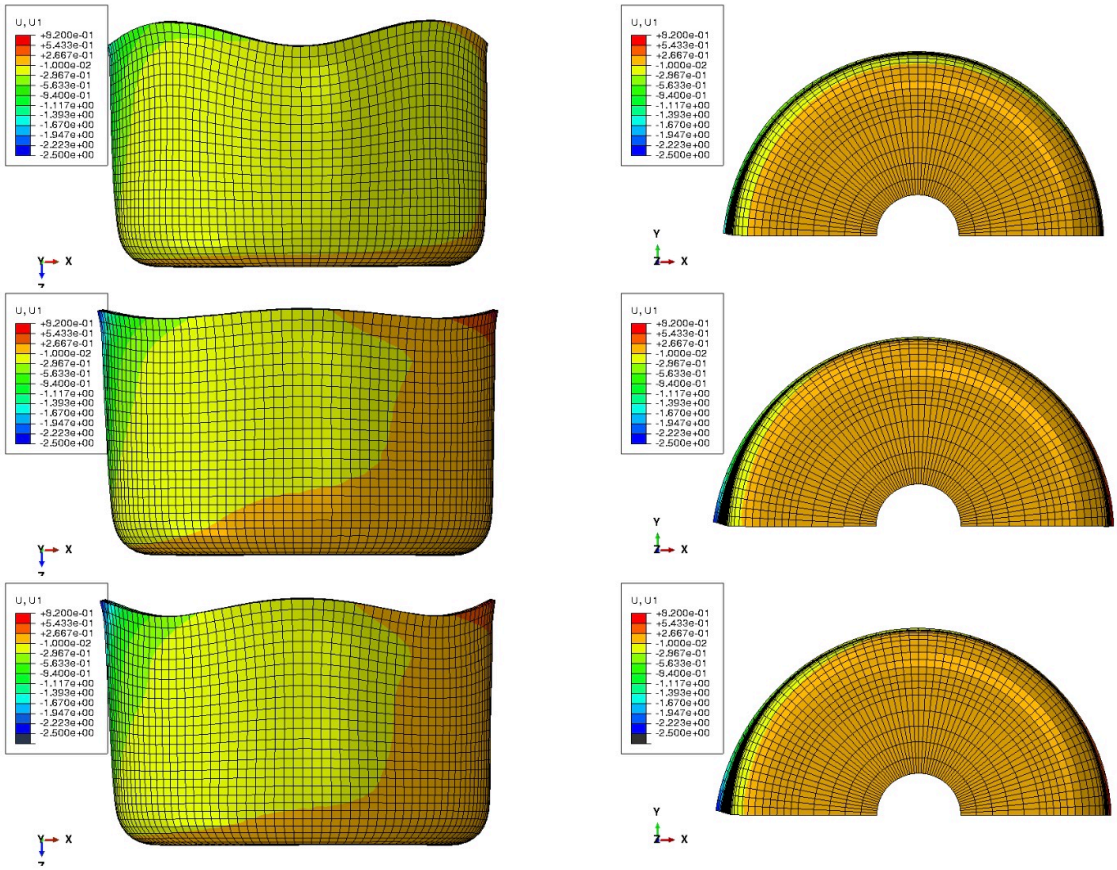


Fig. 5.46: Displacement contours, After Springback, lateral and top views (xx axis, along Rolling and cutting direction) for AFR-R (top), AFR-SiP and AFR-S3D (bottom) approaches

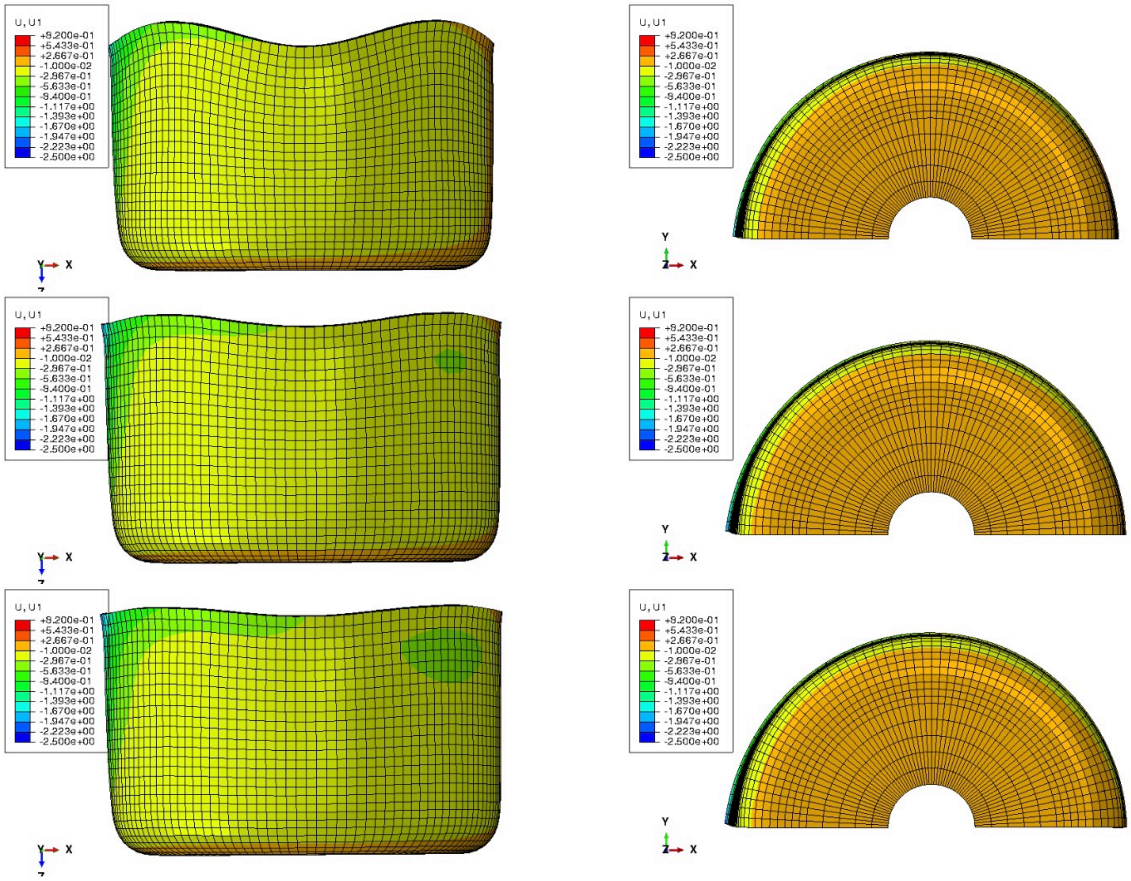


Fig. 5.47: Displacement contours, After Springback, lateral and top views (xx axis, along Rolling and cutting direction) for AFR-R (top), NAFR-SiP and NAFR-S3D (bottom) approaches

5.2.3 Earing evolution and experimental validation

Since earing evolution has been a main topic of analysis for presented anisotropic models it would be important also to understand any possible correspondence between springback and this cup earing profile. Such results of earing profile, before and after springback are shown in figures 5.48 and 5.49, respectively, for AFR and NAFR approaches. As seen, it is observed that under the defined springback boundary conditions, the split side of cup (180ž to RD), due to being partially released, gets a lower height for such side of the cup, which is related with deformation by elastic relaxation on lateral wall and including the cup base.

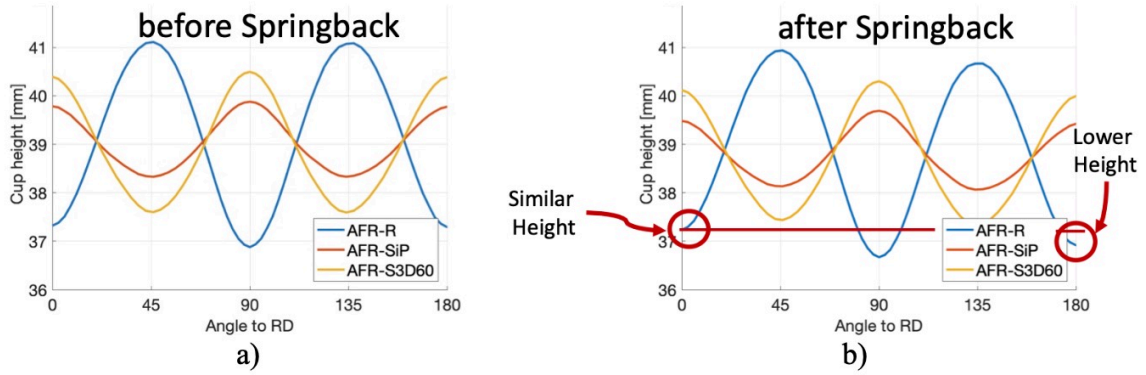


Fig. 5.48: Cup height evolution along different angles to the rolling direction, Before and After Springback for AFR-R vs. AFR-SiP vs AFR-S3D; a cup height change is observed after springback

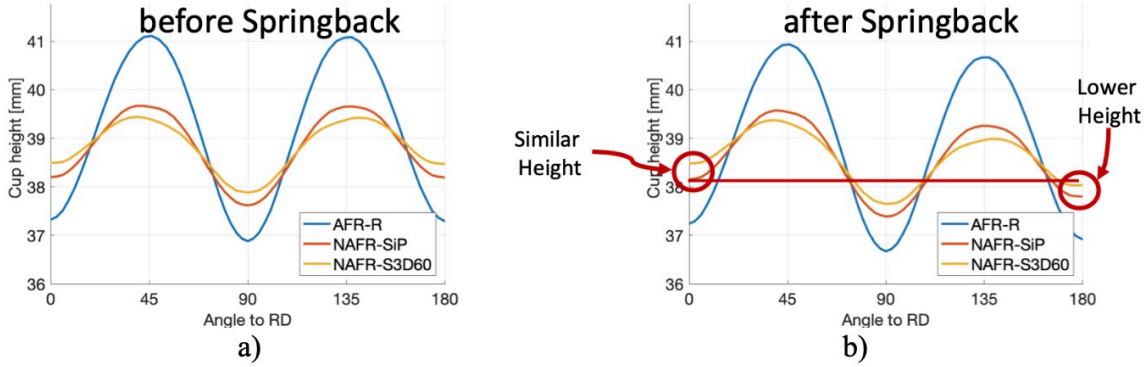


Fig. 5.49: Cup height evolution along different angles to the rolling direction, Before and After Springback for AFR-R vs. NAFR-SiP vs NAFR-S3D; a cup height change is observed after springback

The validation of current numerical results was performed by considering an experimental cup and a high resolution, optical digitizer (ATOS Triple Scan), which delivered the three-dimensional measuring data for cylindrical cup after split, in STL format. Such data was imported to Abaqus post-processer and experimental cup images could be compared with simulation images, in addition to using external developed tools in MatLab, for visualization and analysis. Figure 5.50 shows such imported experimental cup geometry, as well as the methodology to obtain a section profile for comparison with numerical profile. As shown, from the complete cup geometry it was selected an array of points defining a band for which a cup section profile is retrieved containing the cutting part of splitting. As highlighted in figure by zooming a part of the band, the digitized data contains the outer part of cup surface, but in the cutting split

contains also points at the sheet thickness, although not perfectly uniform. This highlight shall be observed, since it must be taken into account when seeing the comparison of profiles, figure 5.52.

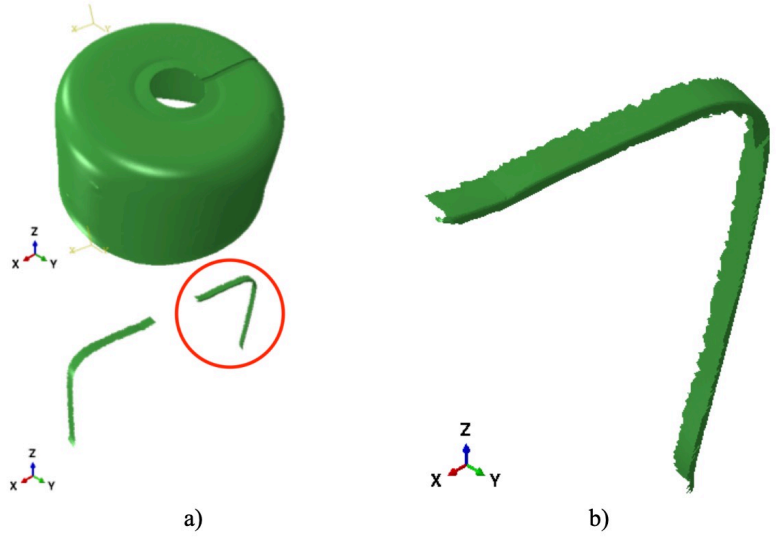


Fig. 5.50: View of experimental cup after vertical split (STL data); a band of points has been selected for comparison with experiment; a) view of total cup and selected band, along cup split cutting; b) detail view of band from a), in which surface data is seen for sheet thickness (to take into account on comparison with experimental profile)

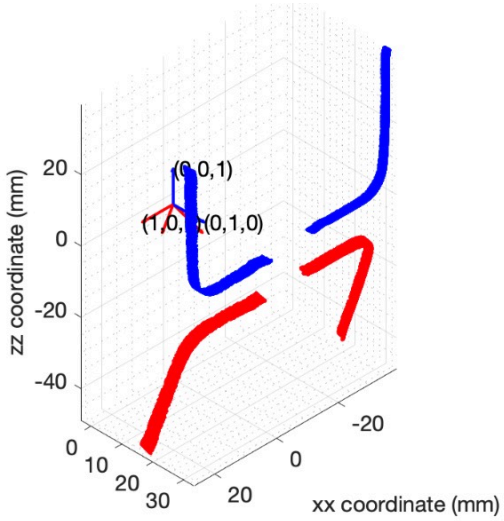


Fig. 5.51: Experimental STL raw data with corresponding coordinate system before transformation (in red) and same data after rotation to the coordinate system used in simulation (blue)

In order to follow the steps for comparison of experimental versus numerical

results, the next step after selecting the band defined in figure 5.50 it was to transform the digitized data coordinate system into the coordinate system from numerical results. For such purpose, a MatLab script was developed to read and visualize the selected points of the cup band (figure 5.51), then the coordinate system from raw data was defined by using several representative points from bottom of cup and the following step was to rotate the digitized defined coordinate system into a new coordinate system, the one used in simulation.

Supposing that we want to (linearly) change the basis vectors v_1, v_2, v_3 to u_1, u_2, u_3 from $x^{'}$, $y^{'}$, $z^{'}$ coordinate system to x, y, z coordinate system, respectively, the two representations of a vector $\boldsymbol{v}$ are given by

$$\boldsymbol{v} = \mathbf{a}^T \begin{bmatrix} v_1 \\ b_2 \\ v_3 \end{bmatrix}, \ and \ \boldsymbol{v} = \boldsymbol{b}^T \begin{bmatrix} u_1 \\ u_2 \\ u_3 \end{bmatrix}, \tag{5.2.1}$$

where $\mathbf{a} = (a_1 \ a_2 \ a_3)^T$ and $\mathbf{b} = (b_1 \ b_2 \ b_3)^T$, are the coordinates of the vector in each of the two coordinate systems; then

$$\boldsymbol{v} = \mathbf{a}^T \begin{bmatrix} v_1 \\ v_2 \\ v_3 \end{bmatrix} = \boldsymbol{b}^T \begin{bmatrix} u_1 \\ u_2 \\ u_3 \end{bmatrix} = \boldsymbol{b}^T \boldsymbol{R} \begin{bmatrix} v_1 \\ v_2 \\ v_3 \end{bmatrix}, \tag{5.2.2}$$

which implies that

$$\boldsymbol{a} = \boldsymbol{R}^T \boldsymbol{b} \ and \ \boldsymbol{b} = (\boldsymbol{R}^T)^{-1} \boldsymbol{a} \tag{5.2.3}$$

where the 'change of basis' or Rotation matrix $\boldsymbol{R}$ is defined by:

$$\boldsymbol{R} = \boldsymbol{R}_z(\gamma)\boldsymbol{R}_y(\beta)\boldsymbol{R}_x(\alpha) \begin{bmatrix} cos\gamma & -sin\gamma & 0 \\ sin\gamma & cos\gamma & 0 \\ 0 & 0 & 1 \end{bmatrix} \begin{bmatrix} cos\beta & 0 & sin\beta \\ 0 & 1 & 0 \\ sin\beta & 0 & cos\beta \end{bmatrix} \begin{bmatrix} 1 & 0 & 0 \\ 0 & cos\alpha & -sin\alpha \\ 0 & sin\alpha & cos\alpha \end{bmatrix} \tag{5.2.4}$$

and α, β, γ are the Euler angles about axes x, y, z.

Having the experimental and numerical data sections in the same reference coordinate system it was possible to compare them and figure 5.52 presents such results. The comparison shows numerical points before and after springback,

while experimental data corresponds to final geometry after springback. As seen there is a very close agreement between experiment and simulation. It should be highlighted again that experimental data in split section includes some points from the thickness, as stated in figure 5.50, which gives a thicker line when compared to the other side of the section.

Final comparisons include figures 5.53 and 5.54, which show the lateral views on experimental versus numerical geometry for xz and yz planes.

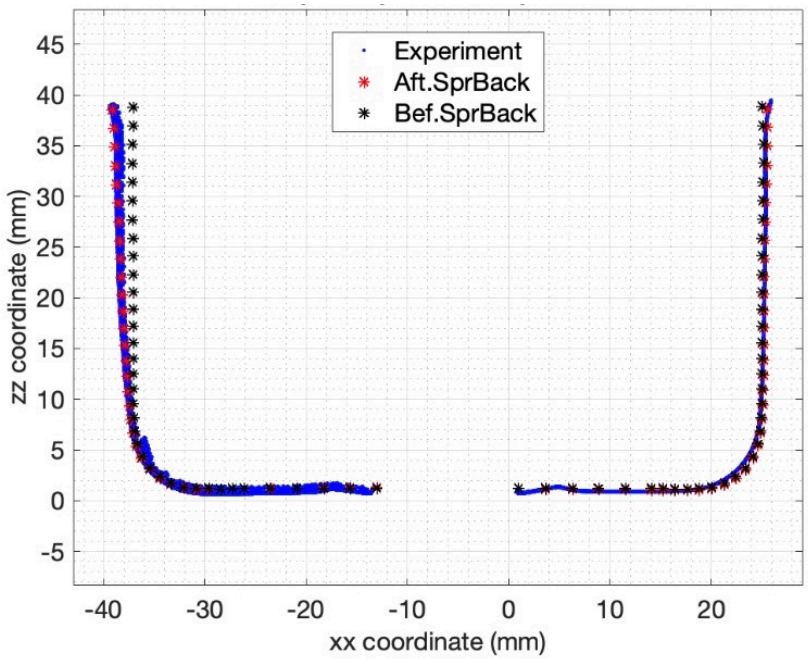


Fig. 5.52: Comparison of experimental cup profile (blue continuous line) versus the simulation profile (red points) after springback; simulation profile points before springback are also shown as blue points

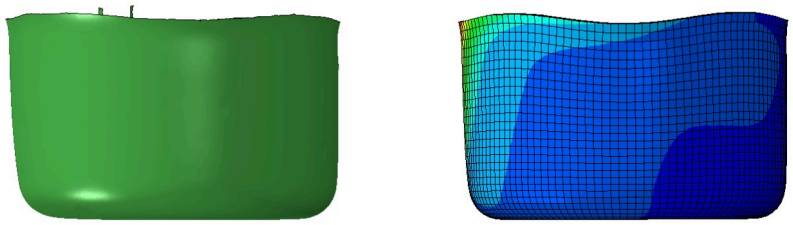


Fig. 5.53: Comparison of experimental geometry (left) with predicted geometry in simulation (NAFR-SiP) for xz plane (same view as section profile in figure 5.52)

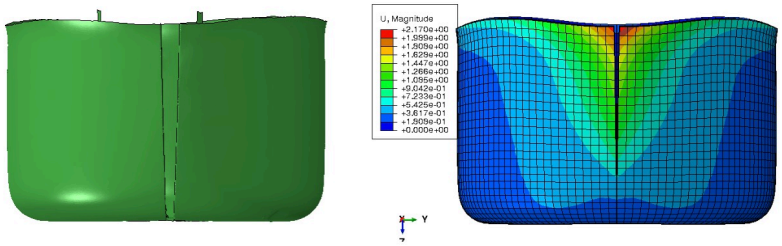


Fig. 5.54: Comparison of experimental geometry (left) with predicted geometry in simulation (NAFR-SiP) for yz plane, showing the opening of cup vertical split after springback (experimental cutting by circular saw with 2 mm width)

Although quantification is not performed between experiment and simulation results, the presented comparisons in previous figures show a very close agreement for simulation results with developed methodologies under current research, namely the Non-Associated Flow Rules with S-inPlane or S3D approaches. It is also observed in this cylindrical cup forming application test and DP780 steel that for approaches based in Associated Flow Rule, none of them can represent and can predict the anisotropic behavior observed in experiments, AFR-R approach having a correct earing evolution but not the right amplitude, AFR-stress based approaches having both incorrect earing evolution and earing amplitude. A final conclusion states that both developed Non-Associated Flow Rule approaches have, for this steel material, a similar performance with their predicted results. However, this conclusion cannot be generalized and in previous chapter it was observed that using other materials the non-associated approach S3D reaches better predictions than NAFR-S-inPlane approach.

6 CONCLUSIONS AND FUTURE WORK

6.1 Concluding remarks

The mechanical behavior of metallic materials is a topic of great importance and its study has been a topic of great interest with the development and formulation of mathematical models capable of describing such behavior as close to experimental evidence as possible. Often, the industry can take competitive advantages from these scientific developments by better understanding the behavior of materials and their applications, in addition to developments and optimization of manufacturing processes. Automobile and aerospace industries are among those industries, which represent driving forces for such scientific developments.

This work, applied to sheet metal forming, had its focus on the development and implementation of an anisotropic constitutive model based on the associated flow rule (AFR) and the non-associated flow rule (NAFR), evaluating their advantages and corresponding results. The research topics included the analysis of a benchmark with an industrial component, proposed by Numisheet conference series, and the application of developed models to a cylindrical cup test by analyzing the anisotropic behavior and springback.

The work was divided into several chapters, as defined in first chapter, from which some main conclusions can be summarized.

Chapter three was concerned with springback analysis for an industrial automotive panel in aluminum, which was the topic of a benchmark test. It was possible to perform simulation at the level of current challenges for numerical modelling

of sheet metal forming processes and predicting the stamping of an industrial component by using practical stages of binder closure, forming, trimming and springback, The investigation gave the possibility to understand some of the reasons why Numisheet BM2 results didnt give the complete intended numerical validation answers that were expected. The performed analysis gave the possibility to redirect the use of some guidelines, which may support some directions to follow, when comparison of complex geometries needs to be performed.

Chapter four deals with the validation and testing of implemented anisotropic material models based on AFR and NAFR using a user material VUMAT subroutine for the commercial finite element code Abaqus. The tests comprised a single element case study and a cylindrical cup deep drawing test and the selected materials included AA2090-T3, A6061P-T6 and a SPCE steel. Hill48, the most well-known quadratic model, was selected for the definition of the yield function and plastic potential function, due to its simple functional forms. The results of the cup drawing test showed that the proposed non-AFR model could improve the accuracy of results, as well as providing an effective and efficient approach to anisotropic sheet metal simulation and prediction, which by using the proposed quadratic model could also offer accurate simulation results with minimal material testing.
Chapter five corresponds to the application of implemented anisotropic constitutive models to an available experimental cylindrical cup test, in order to assess and investigate the predictive capabilities for cup drawing and corresponding earing evolution, in addition to predicting cup springback, after a cup vertical split. The cup test was experimentally performed for a DP780 steel. It is observed in this cup forming application test and this steel material that for approaches based in Associated Flow Rule, none of them can represent and can predict the anisotropic behavior observed in experiments, AFR-R approach having a correct earing evolution but not the right amplitude, AFR-stress based approaches having both incorrect earing evolution and earing amplitude. This comparative study also showed that NAFR models can best reproduce the experimental anisotropic behavior of cylindrical cups and it was observed a very close agreement for predicted simulation results.

6.2 Future work

From current work it was understood that further research could be undertaken and some directions could be pursued.

The study on Benchmark 2 from Numisheet 2016 gave an insight to the required level of accuracy currently needed for experimental results, so that appropriate assessment and validation of developments in the numerical field can be adequately accomplished. Benchmarks or Round Robin Tests, by promoting different institutions and research groups to participate, is an important direction to a better knowledge on how to provide experimental reference data for such objective, in which the possible scatter and dispersion of results can be analyzed and experimental data can be defined with the corresponding uncertainty. In this work the AFR and NAFR approaches have been used with Hill48 anisotropic yield criterion. It would be interesting to evaluate the advantages and disadvantages of a selected flow rule, AFR and NAFR, with additional advanced yield criteria such as Yld89, Yld2000, BBC2008 and evaluating the stability of the NAFR formulation, when combined with different yield functions.

Additional tests should be pursued to complement the validation of application of anisotropic models to springback. It would be envisaged the use of the so-called Split ring test, which presents a high springback response and the possibility to better testing the implemented numerical models. In addition to testing the AFR vs. NAFR approaches the numerical model should include, kinematic hardening, Bauschinger effect and evolution of elastic properties. State-of-art research, when using this test, also takes into consideration evolutionary anisotropic parameters for yield stress or r-values, instead of being constant.

References

[1] M. Wali, R. Autay, J. Mars, and F. Dammak, "A simple integration algorithm for a non-associated anisotropic plasticity model for sheet metal forming," *International Journal for Numerical Methods in Engineering*, vol. 107, pp. 183–204, jul 2016.

[2] K. Katchasuwanmanee, R. Bateman, and K. Cheng, "An Integrated approach to energy efficiency in automotive manufacturing systems: quantitative analysis and optimisation," *Production & Manufacturing Research*, vol. 5, pp. 90–98, jan 2017.

[3] H. S. Park, T. T. Nguyen, and X. P. Dang, "Energy-Efficient optimization of forging process considering the manufacturing history," *International Journal of Precision Engineering and Manufacturing - Green Technology*, vol. 3, pp. 147–154, apr 2016.

[4] J. Jeswiet, M. Geiger, U. Engel, M. Kleiner, M. Schikorra, J. Duflou, R. Neugebauer, P. Bariani, and S. Bruschi, "Metal forming progress since 2000," *CIRP Journal of Manufacturing Science and Technology*, vol. 1, no. 1, pp. 2–17, 2008.

[5] Hill R., "A theory of the yielding and plastic flow of anisotropic metals," *Proceedings of the Royal Society of London. Series A. Mathematical and Physical Sciences*, vol. 193, no. 1033, pp. 281–297, 1948.

[6] J. Woodthorpe and R. Pearce, "The anomalous behaviour of aluminium sheet under balanced biaxial tension," *International Journal of Mechanical Sciences*, vol. 12, pp. 341–347, apr 1970.

[7] M. Dunand, A. P. A. Maertens, M. Luo, and D. Mohr, "Experiments and modeling of anisotropic aluminum extrusions under multi-axial loading - Part I: Plasticity," *International Journal of Plasticity*, vol. 36, pp. 34–49, sep

2012.

[8] F. Barlat, R. C. Becker, Y. Hayashida, Y. Maeda, M. Yanagawa, K. Chung, J. C. Brem, D. J. Lege, K. Matsui, S. J. Murtha, and S. Hattori, "Yielding description for solution strengthened aluminum alloys," *International Journal of Plasticity*, vol. 13, no. 4, pp. 385–401, 1997.

[9] J. Yoon, F. Barlat, R. Dick, and M. Karabin, "Prediction of six or eight ears in a drawn cup based on a new anisotropic yield function," *International Journal of Plasticity*, vol. 22, pp. 174–193, jan 2006.

[10] L. Ming and O. Pantalé, "An efficient and robust VUMAT implementation of elastoplastic constitutive laws in Abaqus/Explicit finite element code," *Mechanics and Industry*, vol. 19, no. 3, p. 308, 2018.

[11] T. B. Stoughton, "A non-associated flow rule for sheet metal forming," *International Journal of Plasticity*, vol. 18, no. 5-6, pp. 687–714, 2002.

[12] V. Cvitanić, F. Vlak, and Ž. Lozina, "A finite element formulation based on non-associated plasticity for sheet metal forming," *International Journal of Plasticity*, vol. 24, pp. 646–687, apr 2008.

[13] A. Taherizadeh, D. E. Green, A. Ghaei, and J.-W. Yoon, "A non-associated constitutive model with mixed iso-kinematic hardening for finite element simulation of sheet metal forming," *International Journal of Plasticity*, vol. 26, pp. 288–309, 2009.

[14] G. Wang, X. Qian, X. Li, H. Hou, Y. Liu, and Y. Lou, "A study on compressive anisotropy and nonassociated flow plasticity of the AZ31 magnesium alloy in hot rolling," *Mathematical Problems in Engineering*, vol. 2014, pp. 1–9, 2014.

[15] J. Lian, F. Shen, X. Jia, D. C. Ahn, D. C. Chae, S. Münstermann, and W. Bleck, "An evolving non-associated Hill48 plasticity model accounting for anisotropic hardening and r-value evolution and its application to forming limit prediction," *International Journal of Solids and Structures*, vol. 151, no. April, pp. 20–44, 2018.

[16] B. Tang, F. Wu, Z. Wang, and S. Zhang, "Study on non-associated plasticity

with various forward Euler stress integration algorithms and its prediction of earing in cylindrical cup drawing," *International Journal of Mechanical Sciences*, vol. 157-158, pp. 384–402, jul 2019.

[17] B. Wu, H. Wang, T. Taylor, and J. Yanagimoto, "A non-associated constitutive model considering anisotropic hardening for orthotropic anisotropic materials in sheet metal forming," *International Journal of Mechanical Sciences*, vol. 169, mar 2020.

[18] K. Runesson and Z. Mroz, "A note on non-associated plastic flow rules," *International Journal of Plasticity*, vol. 5, pp. 639–655, jan 1989.

[19] M. Safaei, W. De Waele, and S.-L. Zang, "A rate-independent non-associated constitutive model for finite element simulation of sheet metal forming," in *Plasticity and its Current Applications 18th International symposium Proceedings*, pp. 61–63, 2012.

[20] J. Mendiguren, L. Galdos, and E. Saenz de Argandoña, "On the plastic flow rule formulation in anisotropic yielding aluminium alloys," *The International Journal of Advanced Manufacturing Technology*, vol. 99, pp. 255–274, oct 2018.

[21] F. Yoshida, T. Uemori, and K. Fujiwara, "Elastic-plastic behavior of steel sheets under in-plane cyclic tension-compression at large strain," *International Journal of Plasticity*, vol. 18, no. 5-6, pp. 633–659, 2002.

[22] J. W. Yoon, F. Barlat, R. E. Dick, K. Chung, and T. J. Kang, "Plane stress yield function for aluminum alloy sheets - Part II: FE formulation and its implementation," *International Journal of Plasticity*, vol. 20, no. 3, pp. 495–522, 2004.

[23] S. Kim, J. Lee, F. Barlat, and M. G. Lee, "Formability prediction of advanced high strength steels using constitutive models characterized by uniaxial and biaxial experiments," *Journal of Materials Processing Technology*, vol. 213, no. 11, pp. 1929–1942, 2013.

[24] T. Ogawa and F. Yoshida, "Springback analysis of U-bending with bottoming," in *AIP Conference Proceedings*, vol. 1383-1129, pp. 1129–1136, American Institute of Physics, aug 2011.

[25] F. Yoshida, H. Hamasaki, and T. Uemori, "A user-friendly 3D yield function to describe anisotropy of steel sheets," in *International Journal of Plasticity*, vol. 45, pp. 119–139, Elsevier Ltd, 2013.

[26] J. Zhu, Y. Xia, H. Luo, G. Gu, and Q. Zhou, "Influence of flow rule and calibration approach on plasticity characterization of DP780 steel sheets using Hill48 model," *International Journal of Mechanical Sciences*, vol. 89, pp. 148–157, dec 2014.

[27] V. Cvitanić, M. Kovačić, and A. Vladislavić, "Numerical analysis of accuracy for evolutionary anisotropic plasticity models," *Engineering Review*, vol. 36, no. 3, pp. 255–267, 2016.

[28] B. Wu, K. Ito, N. Mori, T. Oya, T. Taylor, and J. Yanagimoto, "Constitutive Equations Based on Non-associated Flow Rule for the Analysis of Forming of Anisotropic Sheet Metals," *International Journal of Precision Engineering and Manufacturing-Green Technology*, pp. 1–16, feb 2019.

[29] M. Pfestorf, "Manufacturing of High Strength Steel and Aluminum for a Mixed Material Body in White," *Advanced Materials Research*, vol. 6-8, pp. 109–126, 2005.

[30] K. Mattiasson, "On finite element simulation of sheet metal forming processes in industry," *European Congress on Computational Methods in Applied Sciences and Engineering*, vol. 55, no. September, pp. 11–14, 2000.

[31] H. S. Kim, M. Koç, and M. Ko, "Numerical investigations on springback characteristics of aluminum sheet metal alloys in warm forming conditions," *Journal of Materials Processing Technology*, vol. 204, pp. 370–383, aug 2008.

[32] O. Ghorbel, S. Koubaa, J. Mars, M. Wali, and F. Dammak, "Non associated-anisotropic plasticity model fully coupled with isotropic ductile damage for sheet metal forming applications," *International Journal of Solids and Structures*, feb 2019.

[33] K. J. Lee, Y. Choi, H. J. Choi, J. Y. Lee, and M. G. Lee, "Split-Ring Springback Simulations with the Non-associated Flow Rule and Evolutionary Elastic-Plasticity Models," *JOM*, vol. 70, pp. 906–911, jun 2018.

[34] "NUMISHEET 2016: 10th International Conference and Workshop on Numerical Simulation of 3D Sheet Metal Forming Processes," in *Journal of Physics: Conference Series* (O. A. Rui P.R. Cardoso, Jeong Whan Yoon, Robert E. Dick, Eduardo Souza Neto, J.M.A. Cesar de Sa, ed.), vol. 734, p. 011001, 2016.

[35] J. T. Gau and G. L. Kinzel, "A new model for springback prediction in which the Bauschinger effect is considered," *International Journal of Mechanical Sciences*, vol. 43, no. 8, pp. 1813–1832, 2001.

[36] A. Taherizadeh, A. Ghaei, D. E. Green, and W. J. Altenhof, "Finite element simulation of springback for a channel draw process with drawbead using different hardening models," *International Journal of Mechanical Sciences*, vol. 51, no. 4, pp. 314–325, 2009.

[37] B. Levy, "Empirically Derived Equations for Predicting Springback in Bending," *Journal of Applied Metalworking*, vol. 3, no. 2, pp. 135–141, 1984.

[38] J. Y. Lee, M. G. Lee, F. Barlat, K. H. Chung, and D. J. Kim, "Effect of nonlinear multi-axial elasticity and anisotropic plasticity on quasi-static dent properties of automotive steel sheets," *International Journal of Solids and Structures*, vol. 87, pp. 254–266, jun 2016.

[39] H. J. Choi, K. J. Lee, Y. Choi, G. Bae, D. C. Ahn, and M. G. Lee, "Effect of Evolutionary Anisotropy on Earing Prediction in Cylindrical Cup Drawing," *JOM*, vol. 69, pp. 915–921, may 2017.

[40] T. Oya, J. Yanagimoto, K. Ito, G. Uemura, and N. Mori, "Material Model based on Non-associated Flow Rule with Higher-order Yield Function for Anisotropic Metals," *Procedia Engineering*, vol. 81, no. October, pp. 1210–1215, 2014.

[41] M. Safaei and W. De Waele, "Study on the definition of equivalent plastic strain under non-associated flow rule for finite element formulation," *International Journal of Plasticity*, vol. 58, pp. 219–238, jul 2014.

[42] R. Autay, S. Koubaa, M. Wali, and F. Dammak, "Numerical implementation of coupled anisotropic plasticity-ductile damage in sheet metal forming process," *Journal of Mechanics*, vol. 34, no. 4, 2018.

[43] J.-W. Lee, M.-G. Lee, and F. Barlat, "Finite element modeling using homogeneous anisotropic hardening and application to spring-back prediction," *International Journal of Plasticity*, vol. 29, pp. 13–41, 2012.

[44] M. Ortiz and J. C. Simo, "An analysis of a new class of integration algorithms for elastoplastic constitutive relations," *International Journal for Numerical Methods in Engineering*, vol. 23, pp. 353–366, mar 1986.

[45] U. Augsburg and W. Germany, "A Cutting Plane Algorithm for a Clustering Problem," *Mathematical Programming*, vol. 45, pp. 59–96, 1989.

[46] M. Safaei, W. De Waele, and S. L. Zang, "Evaluation of Associated and Non-Associated Flow Metal Plasticity; Application for DC06 Deep Drawing Steel," *Key Engineering Materials*, vol. 504-506, pp. 661–666, feb 2012.

[47] A. Bouhamed, H. Jrad, L. B. Said, M. Wali, and F. Dammak, "A non-associated anisotropic plasticity model with mixed isotropickinematic hardening for finite element simulation of incremental sheet metal forming process," *International Journal of Advanced Manufacturing Technology*, vol. 100, pp. 929–940, jan 2019.

[48] Z. Damian-Noriega, R. Perez-Moreno, S. A. Villanueva-Pruneda, V. M. Dominguez-Hernandez, J. P. A. Puerta-Huerta, and C. Huerta-Munoz, "A New Equation to Determine the Springback in the Bending Process of Metallic Sheet," *Icces*, vol. 8, no. 1, pp. 25–30, 2008.

[49] M. Allen, M. C. Oliveira, S. Hazra, O. Adetoro, A. Das, and R. Cardoso, "Benchmark 2 - Springback of a Jaguar Land Rover Aluminium," *Journal of Physics: Conference Series*, vol. 734, no. 022002, pp. 1–54, 2016.

[50] D. Neto, M. Oliveira, J. Alves, A. Santos, and L. Menezes, "Prediction of wrinkling and springback in sheet metal forming," in *MATEC Web of Conferences*, vol. 80, 2016.

[51] L. Menezes and C. Teodosiu, "Three-dimensional numerical simulation of the deep-drawing process using solid finite elements," *Journal of Materials Processing Technology*, vol. 97, pp. 100–106, jan 2000.

[52] M. C. Oliveira, J. L. Alves, and L. F. Menezes, "Algorithms and strategies for

treatment of large deformation frictional contact in the numerical simulation of deep drawing process," *Archives of Computational Methods in Engineering*, vol. 15, pp. 113–162, jun 2008.

[53] D. M. Neto, M. C. Oliveira, L. F. Menezes, and J. L. Alves, "Applying Nagata patches to smooth discretized surfaces used in 3D frictional contact problems," *Computer Methods in Applied Mechanics and Engineering*, vol. 271, pp. 296–320, apr 2014.

[54] A. D. Santos and P. Teixeira, "A study on experimental benchmarks and simulation results in sheet metal forming," *Journal of Materials Processing Technology*, vol. 199, pp. 327–336, apr 2008.

[55] A. D. Santos, J. Ferreira Duarte, A. Reis, A. Barata da Rocha, L. Menezes, M. Oliveira, A. Col, and T. Ono, "Towards standard benchmarks and reference data for validation and improvement of numerical simulation in sheet metal forming," in *Journal of Materials Processing Technology*, vol. 125-126, pp. 798–805, Elsevier, sep 2002.

[56] Col A, "Presentation of the3ds research project," in *The Fifth International Conference and Workshop on Numerical Simulation of 3D Sheet Forming Processes* (K. Y. In Huh H., Yang D.-Y., Oh S.I., ed.), (Jeju Island, Korea), pp. 643 – 647, 2002.

[57] A. Col and A. D. Santos, "Influence of stamping rate upon springback," in *AIP Conference Proceedings*, vol. 778 A, pp. 228–233, American Institute of Physics Inc., aug 2005.

[58] N. E. Inc, www. m-research. co. Jp, and U. 2004, "M&M Research."

[59] M. Ablat and A. Qattawi, "Numerical simulation of sheet metal forming: a review," *International Journal of Advanced Manufacturing Technology*, vol. 89, no. 1-4, 2017.

[60] F. Barlat, J. W. Yoon, and O. Cazacu, "On linear transformations of stress tensors for the description of plastic anisotropy," *International Journal of Plasticity*, vol. 23, pp. 876–896, may 2007.

[61] R. Hill, "Constitutive modelling of orthotropic plasticity in sheet metals,"

Journal of the Mechanics and Physics of Solids, vol. 38, no. 3, pp. 405–417, 1990.

[62] D. Banabic, H. Aretz, D. S. Comsa, and L. Paraianu, "An improved analytical description of orthotropy in metallic sheets," *International Journal of Plasticity*, vol. 21, pp. 493–512, 2005.

[63] F. Barlat, D. J. Lege, and J. C. Brem, "A six-component yield function for anisotropic materials," *International Journal of Plasticity*, vol. 7, pp. 693–712, jan 1991.

[64] M. Safaei, S.-L. Zang, M.-G. Lee, and W. De Waele, "Evaluation of anisotropic constitutive models: Mixed anisotropic hardening and non-associated flow rule approach," *International Journal of Mechanical Sciences*, vol. 73, pp. 53–68, 2013.

[65] J. W. Yoon, F. Barlat, K. Chung, F. Pourboghrat, and D. Y. Yang, "Earing predictions based on asymmetric nonquadratic yield function," *International journal of plasticity*, vol. 16, pp. 1075–1104, aug 2000.

[66] T. Park and K. Chung, "Non-associated flow rule with symmetric stiffness modulus for isotropic-kinematic hardening and its application for earing in circular cup drawing," *International Journal of Solids and Structures*, vol. 49, pp. 3582–3593, dec 2012.

[67] P. Meireles, J. G. Magalh, M. Coorientador, A. Dias, S. M. Integrado, and E. Mec, *Desenvolvimento de um Sistema de Controlo e Aquisição de Dados para Máquina Universal de Ensaios de Chapas Metálicas*. PhD thesis, 2019.

[68] R. L. Amaral, A. D. Santos, and S. S. Miranda, "Limiting drawing ratio and formability behaviour of dual phase steelsexperimental analysis and finite element modelling," in *Advanced Structured Materials*, vol. 98, pp. 469–486, Springer Verlag, 2019.

[69] R. Amaral, A. D. Santos, C. d. S. José, and S. Miranda, "Formability prediction for AHSS materials using damage models," *Journal of Physics: Conference Series*, vol. 843, p. 012018, may 2017.

[70] X. Xue, *Modelling and control of twist springback in lightweight automotive structures with complex cross-sectional shape*. PhD thesis, Universidade de

Aveiro, 2016.

[71] V. Simões, M. Oliveira, D. Neto, P. Cunha, H. Laurent, J. Alves, and L. Menezes, "Numerical study of springback using the split-ring test: influence of the clearance between the die and the punch," *International Journal of Material Forming*, 2017.